Triaxiality in neutron-rich Ruthenium isotopes

New lifetimes measured in ^{109,110,111}Ru

Johannes Sørby Heines

Thesis submitted for the degree of
Master in Nuclear and Particle Physics
(Nuclear Physics)
60 credits

Department of Physics
Faculty of mathematics and natural sciences

UNIVERSITY OF OSLO

Spring 2022

Triaxiality in neutron-rich Ruthenium isotopes

New lifetimes measured in $^{109,110,111}Ru$

Johannes Sørby Heines

Triaxiality in neutron-rich Ruthenium isotopes

http://www.duo.uio.no/

Abstract

This thesis explores the asymmetrical deformation of Ruthenium isotopes, aiming to provide reliable experimental data useful for testing theoretical nuclear structure models.

We have obtained reduced transition probabilities $B(E2)$ for a number of transitions in ^{109,110,111}Ru. A fit of the generalised triaxial rotor model indicates ^{110}Ru is well deformed, with a slightly oblate triaxial shape. The results are compared to various global nuclear structure models. First approximation reveals no evidence of shape changes between ^{109}Ru and ^{111}Ru, more accurate results will be achieved through triaxial particle rotor calculations.

The dataset at the heart of the analysis, obtained with AGATA and VAMOS++ at GANIL in 2017, features much higher statistics for a much larger number of nuclei than have previously been available. This has allowed us to get reliable lifetime measurements for the neutron odd ^{109,111}Ru, and for both the ground-state band and one phonon γ-band in ^{110}Ru. Additionally, it is expected to significantly reduce systematic errors when comparing results from different nuclei.

We have developed and applied a new method for extracting lifetimes from the decay curves obtained in recoil distance Doppler shift measurements. By imposing constraints of physicality, it is expected to produce more reliable results than previous methods. A code for simultaneously fitting multiple gamma-spectra with shared parameters has also been developed.

Acknowledgements

As I reach this milestone that is the completion of my Master's thesis, looking back I see so many people who have helped and supported me along the way, and without whom this thesis would not have been possible.

Thank you, Andreas and Victor, for guiding me through this work with open doors, always being available to help me and answer my questions. I feel very fortunate to have had you as my supervisors.

Thank you, everyone in the nuclear physics group, for sharing ideas, snacks and anecdotes. This great work environment we have is not something I take for granted. You are wonderful colleagues, and I look forward to continue working alongside you.

Thank you, Sylvain Mérendet, for believing in me, pushing me to improve and encouraging me to pursue a career in physics.

Thank you Mamma, Pappa and Aurora for supporting me emotionally through everything, for listening to me ramble about kiwi-shaped nuclei and buggy code, and for reminding me to take breaks and relax. I would not have gotten through this without you.

Johannes

This thesis uses scientific colour maps by Crameri (2021) to prevent visual distortion of the data and exclusion of readers with colour-vision deficiencies (Crameri, Shephard, and Heron 2020).

Contents

List of Figures

List of Tables

Chapter 1

Introduction

For millennia, humans have looked at the world and wondered "What is it all made of?". The concept of the atom dates back to the philosopher Democritus (fourth century BC). The word comes from Greek "atomos" meaning indivisible. The discovery of radioactivity by Henri Becquerel in 1896 – and the subsequent research by Pierre and Marie Skłodowska Curie and by Rutherford et al. – provided the first indication that atoms are not, in fact, immutable nor indivisible. The discovery of the electron by J.J. Thomson in 1897 led him to suggest, in 1903, the so-called "plum pudding" model of the atom, where electrons move freely in an otherwise uniform region of positive charge. The famous experiments suggested by Rutherford and performed by Geiger and Marsden starting in 1909 led to the first nuclear model of the atom in 1911, where the electrons orbit around a positively charged nucleus. The nature of the nucleus itself, as composed of positive protons and neutral neutrons, followed the discovery of the neutron by Chadwick in 1932.

Today, research into nuclear structure is aimed towards understanding how the protons and neutrons interact to give rise to the various observed nuclear properties. Following this, it aims to predict those properties for nuclei which cannot be observed.

The best description of the internal structure of nuclei to date is the shell model. Proposed by Maria Goeppert Mayer in 1949, it models protons and neutrons as arranged in shells with discrete energies.

The question of the nature of matter is accompanied by another age-old question: "Where does it come from?". The universe is mostly made out of Hydrogen, in fact, approximately 73% of the mass of the visible universe is Hydrogen. What remains is principally Helium: the rest of the periodic table makes up only 2%. The creation of elements is called nucleosynthesis, and is one of the major fields of study in nuclear astrophysics.

The rapid neutron capture process, or r-process, creates extremely neutron rich nuclei close to the limit of what is possible, which then decay into the slightly neutron rich elements we observe. Calculations seeking to describe the r-process require information about the properties of these very exotic nuclei, and since we cannot create and study them directly, we require models which can be extrapolated far beyond the experimentally available data. A multitude of such models exist, which diverge significantly as they are extrapolated. To select and improve them, then, one needs to compare them against experimental data, and as such acquiring more data contributes to gaining more precise insight into the formation of heavy elements. Regions where the models differ significantly are of particular interest, and the neutron rich Ruthenium isotopes studied in this work are part of one such region.

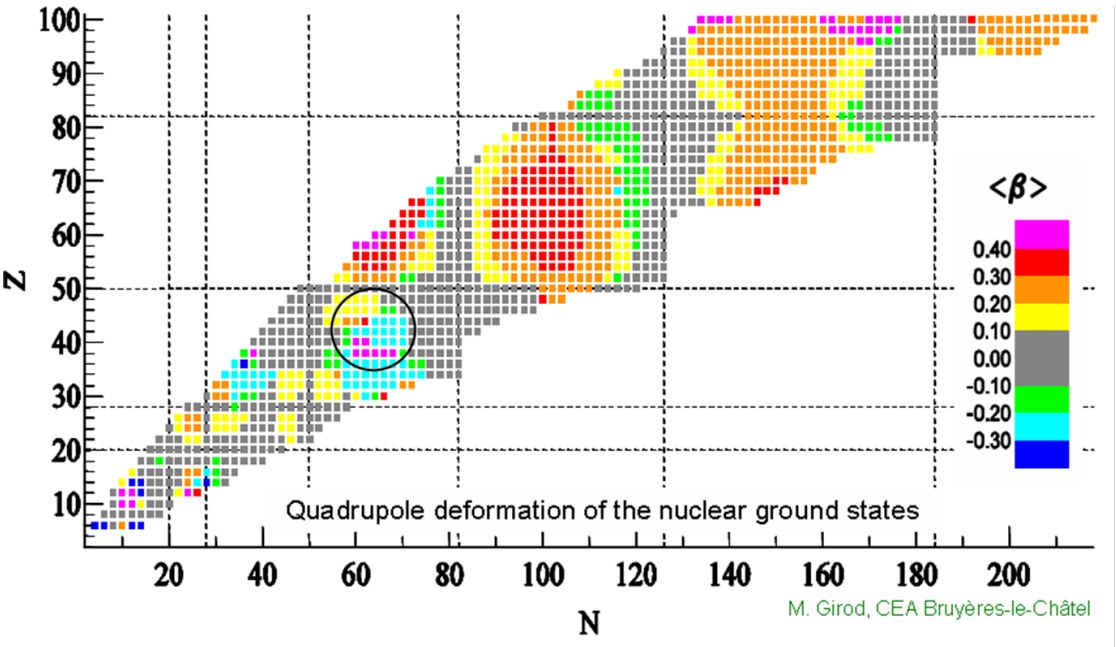

Figure 1.1: The nuclear chart, with the $A \sim 100$ region highlighted. The colours indicate the degree of deformation of the nuclei. Figure by Girod (2007) showing calculations by Hilaire and Girod (2007).

The easiest nuclei to experiment on are those close to the valley of stability, but these also tend to be where the models agree. In order to usefully test different models of nuclear structure, we need do conduct our experiments for a situation where the models give different predictions. The more the predictions differ, the better the test. The highlighted region of the nuclear chart in figure 1.1 is just what we are looking for. Indeed, it features several nuclei with rare properties and widely varying theoretical predictions, making it an ideal testing ground for nuclear structure models. The Strontium and Zirconium chains, for instance, exhibit shape coexistence, where different states in a nucleus correspond to different shapes. As for the Ruthenium chain, it is one of the few to contain isotopes without axial symmetry.

In 2017, an experiment was performed at the Grand accélérateur national d'ions lourds (GANIL) facility in Caen, France, with the aim of measuring the lifetimes of excited states of a previously unattained number on nuclei in the $A \sim 100$ region. This was achieved by a unique experimental setup. By employing a fusion-fission reaction, the experiment produced a very high number of nuclei, which could be identified individually in a magnetic spectrometer. The utilisation of a γ-ray tracking detector allowed it to reliably extract lifetimes from a substantial number of these nuclei, many more than the previous, and first, experiment to employ this setup.

Obtaining data from this many nuclei from the same experiment poses a significant advantage when it comes to comparing the properties of different nuclei. Indeed, we can expect systematic errors to be similar for all the measured nuclei, and thus have little effect on their relative properties.

This thesis is structured as follows: Chapter 2 introduces the shell model, explains the concept of nuclear deformation, and presents an overview of the previous work done on the studied nuclei. Chapter 3 describes the experimental setup, including the general principles of the recoil distance Doppler shift method, and the particle identification. Chapter 4 explains the data analysis procedure in detail, and presents new methods developed in this work. The results are presented in chapter 5 and discussed in chapter 6.

Chapter 2

Theoretical background

This chapter lays the ground work for the thesis by going over relevant definitions and theoretical models. Further details on this material can be found in most nuclear structure textbooks, such as Nilsson and Ragnarsson (1995). The second section of this chapter introduces the specifics of Ruthenium isotopes and the previous work done on the topic.

1 Nuclear deformation

1.1 Nuclear shell structure

As mentioned in the introduction, the protons and neutrons in the nucleus are arranged in shells. This structure originates from the Pauli exclusion principle: two fermions cannot occupy the same quantum state simultaneously. The orbital angular momentum $\boldsymbol{l}$ of the nucleons couples to their spin $\boldsymbol{s}$, generating the orbitals shown in figure 2.1. In a spherical nucleus, all orientations of the total angular momentum $\boldsymbol{j}$ result in the same energy level.

Figure 2.1 shows the magic numbers 2, 8, 20, 28 and 50. When the proton or neutron number is close to these magic numbers – or to the higher ones not seen in the figure – it is energetically favourable for the nucleus to be spherical. As one moves away from the magic numbers, however, nuclei can gain energy by deforming; deformations create new states with different energies and different magic numbers.

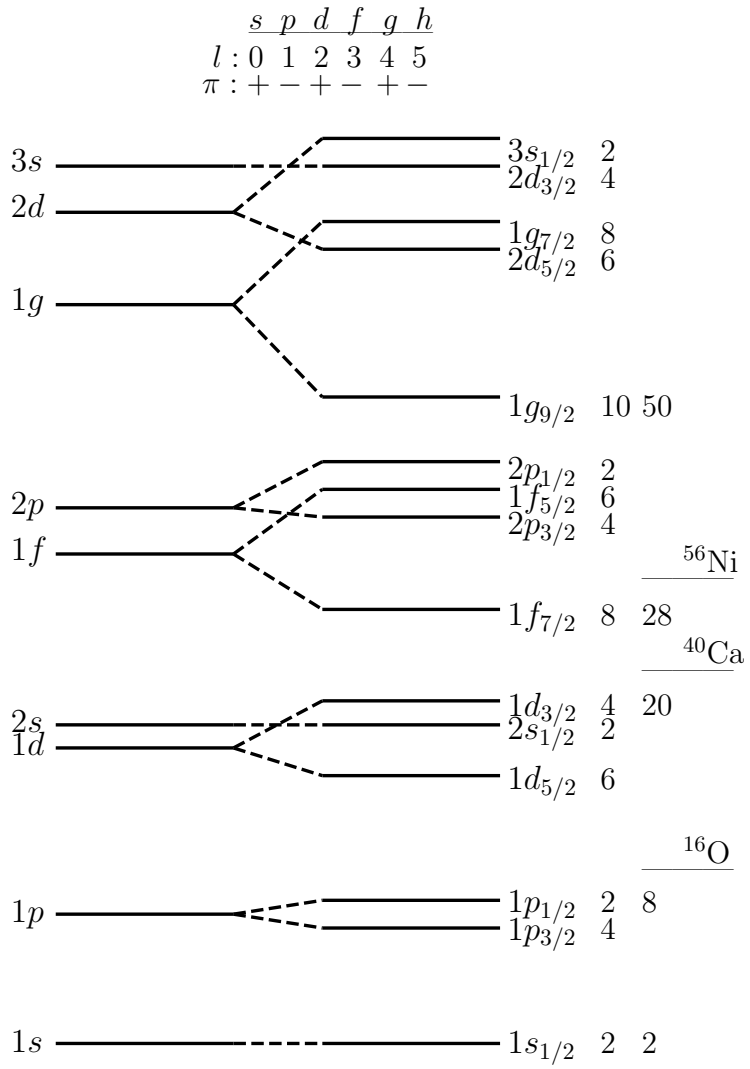

Figure 2.1: Illustration of the first orbitals in the spherical shell model, showing the energy levels obtained with a Woods-Saxon potential on the left and spin-orbit coupling on the right. The levels are named as nl_j, where l uses the spectroscopic notation shown at the top. Figure courtesy of Jon K. Dahl.

Excitation of the nucleus is, in the simplest case, a result of a single particle changing its energy level. When the gap between energy levels is large, such excitations require more energy. This in turn makes magic nuclei more stable.

1.2 Spherical harmonics and deformation parameters

Any shape in space can be described by expanding the radius vector $\mathbf{R}(t)$ in spherical harmonics $Y_{\lambda\mu}$ as follows:

$$\mathbf{R}(t) = R_0 \left[1 + \sum_{\lambda} \sum_{\mu=-\lambda}^{+\lambda} a_{\lambda\mu}(t) Y_{\lambda\mu}(\theta, \varphi) \right] \quad \text{for} \quad \lambda \in \mathbb{N}, \tag{1.1}$$

where, in the case of a nucleus, R_0 is the radius for a spherical shape. At $\lambda = 0$, there is only one harmonic Y_{00}, and the coefficient a_{00} describes the volume. At $\lambda = 1$, there are three harmonics, $\mu = -1, 0, 1$, which describe the position of the system in space. The remaining terms, that is $\lambda \geq 2$, describe deformation from a spherical shape.

Most nuclei have a quadrupole shape, which is described by the five harmonics corresponding to $\lambda = 2$. Only the coefficients a_{20} and a_{22} are necessary to define the shape; the others give the orientation of that shape in space.

We will consider the shape first. It is useful to define parameters which are easier to visualise than equation (1.1). For instance, the parameters β and γ describe the magnitude and asymmetry of the deformation, respectively, and relate to a_{20} and a_{22} by

$$a_{20} = \beta \cos\gamma, \quad \text{and} \tag{1.2}$$

$$a_{22} = \frac{1}{\sqrt{2}} \beta \sin\gamma. \tag{1.3}$$

The shape of a nucleus is not a fixed value. Rather it follows a potential indicating the probability of finding the nucleus with a given (β, γ) combination. Such potentials are usually plotted in polar coordinates as in figure 2.2, with β as the radial coordinate and γ denoted by the angle. For most nuclei, the minima lie along the edges of the plot: they are deformed along a single axis, around which they are axially symmetric. For $\gamma = 0°$, the symmetry axis is the z-axis and the nucleus is prolate, whereas for $\gamma = 60°$, the nucleus is oblate and symmetric around the x-axis. In the intrinsic frame of the nucleus, then, the oblate deformation along $\gamma = 60°$ can be described equally well by keeping $\gamma = 0°$ and letting β take negative values. Some nuclei are deformed such that they have no axial symmetry. These are called triaxial deformations and correspond to the interior of the plot in figure 2.2.

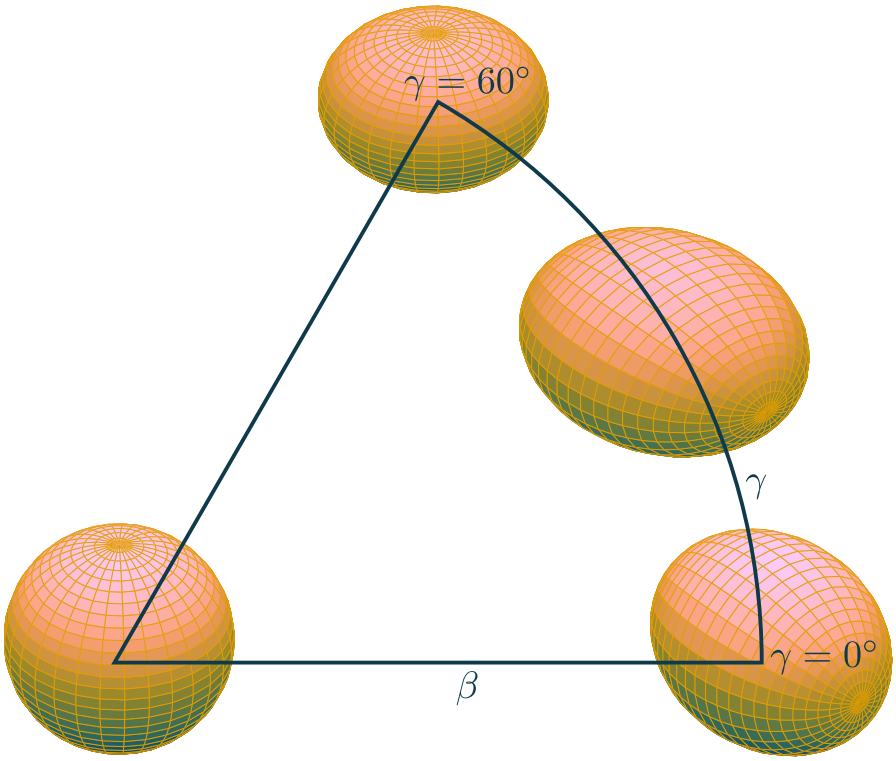

Figure 2.2: Quadrupole deformations can be described by two parameters. β indicates the deviation from a spherical shape, and γ indicates the asymmetry of the deformation.

As the shape of a nucleus becomes asymmetrical, so does the charge distribution. This gives rise to electric moments,most notably in our case the intrinsic quadrupole moment Q_0, defined classically as

$$Q_0 = \int \rho(\mathbf{r})(3z^2 - r^2)\,\mathrm{d}^3r, \tag{1.4}$$

where $\rho(\mathbf{r})$ is the charge distribution and z is the deformation axis. By convention, Q_0 is negative for an oblate nucleus and positive for a prolate one.

1.3 The Nilsson model

As mentioned, deformation of the nucleus displaces the energy levels in the shell model. The theoretical framework describing this was developed by Nilsson (1955). Originally restricted to axially symmetric nuclei, it has since been adapted to

the triaxial case. In the interest of clarity, the axially symmetric Nilsson model will be outlined first. The changes brought about by braking this symmetry will then be made apparent. In the following, we will employ the intrinsic coordinate system, where the z-axis is collinear with the symmetry axis of the nucleus. The quantum numbers in this system are illustrated in figure 2.3.

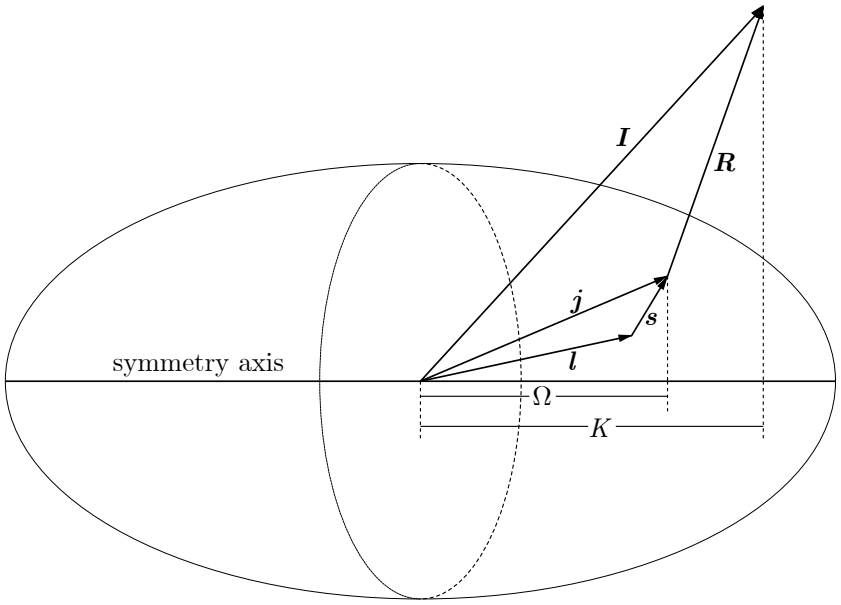

Figure 2.3: Quantum numbers in an axially symmetric nucleus. Each nucleon has orbital angular momentum l and spin s, these combine with the angular momentum R of the other nucleons to yield the total angular momentum I of the nucleus.

The Nilsson model modifies the effective potential of the shell model to describe deformed nuclear shapes. It does this through the frequencies $\omega_\perp$ and ω_z associated with the deformed potential in the intrinsic reference frame. The degree of deformation is specified by the elongation parameter ε^* , such that

$$\omega_z = \omega_0(\varepsilon)\left(1 - \frac{2}{3}\varepsilon\right) \quad \text{and} \quad \omega_\perp = \omega_0(\varepsilon)\left(1 + \frac{1}{3}\varepsilon\right), \tag{1.5}$$

where ω_0 has a weak dependence on ε to conserve the nuclear volume.

The deformed potential causes additional splitting of the energy levels from the spherical shell model in figure 2.1. The possible angular momentum components Ω of a nucleon along the symmetry axis are no longer degenerate, and each or-

*The parameters ε and β are equivalent descriptions of the deformation magnitude, and relate one-to-one on $[0, \infty)$ by $\beta = \sqrt{5/\pi}\sum_n 4\varepsilon^n/3^n$.

bital is filled by only two particle with time-reversal symmetry. Figure 2.4 shows calculated Nilsson orbitals around the Z and N of Ruthenium isotopes. The splitting of each level according to Ω is apparent.

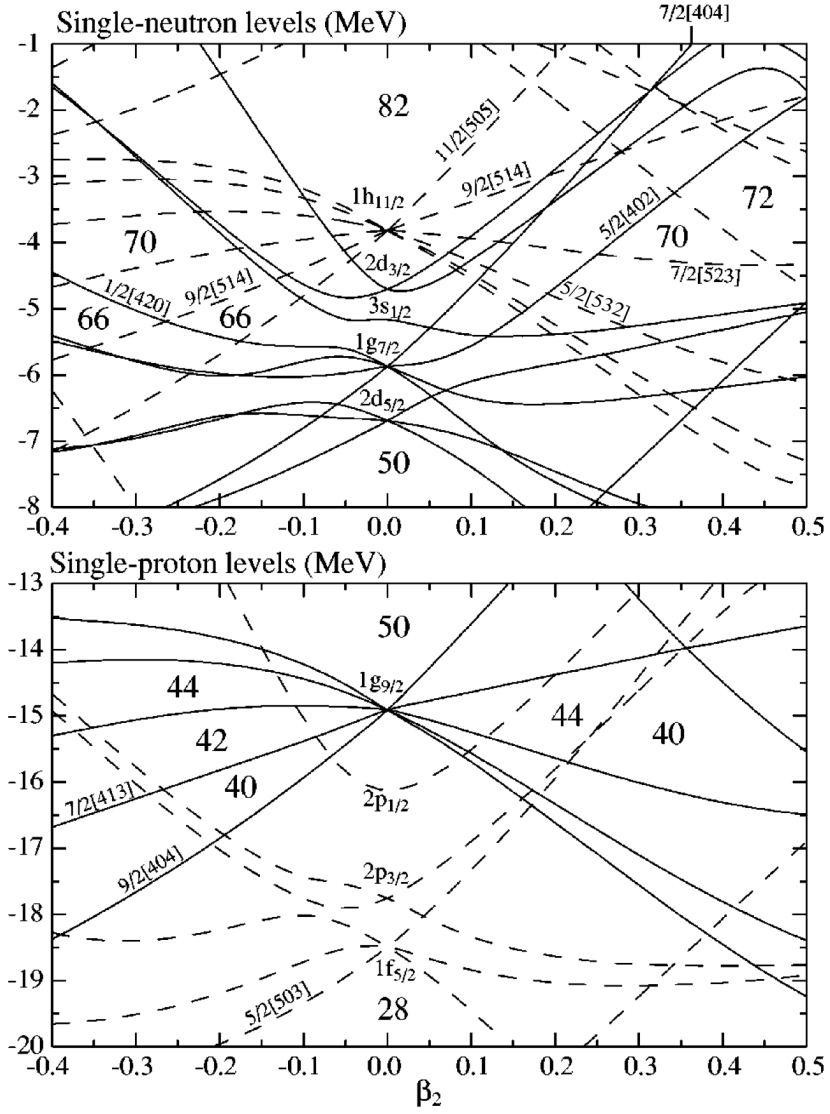

Figure 2.4: Calculated single-neutron (top) and single-proton (bottom) levels in the Nilsson model, assuming axial symmetry. Positive and negative parity is indicated by solid and dashed lines, respectively, and the orbitals are labeled as $\Omega[Nn_z\Lambda]^\dagger$. The figure is adapted from Xu, Walker, and Wyss (2002), who performed the calculations.

$^\dagger[Nn_z\Lambda]$ are called asymptotic quantum numbers. We will not treat these here, and refer the reader to any textbook description of the Nilsson model.

Only Ω and the parity Π remain good quantum numbers for orbitals in a deformed nucleus. Orbitals originating from different j shells with the same Ω^{Π} interact with each other through mixing. This results in such orbitals repelling each other as can be seen in figure 2.4.

In the triaxial case, the model requires a separate frequency for each axis of deformation, namely

$$\omega_x = \omega_0(\varepsilon, \gamma)\left[1 - \frac{2}{3}\varepsilon\cos\left(\gamma + \frac{2\pi}{3}\right)\right], \tag{1.6}$$

$$\omega_y = \omega_0(\varepsilon, \gamma)\left[1 - \frac{2}{3}\varepsilon\cos\left(\gamma - \frac{2\pi}{3}\right)\right] \quad \text{and} \tag{1.7}$$

$$\omega_z = \omega_0(\varepsilon, \gamma)\left[1 - \frac{2}{3}\varepsilon\cos\gamma\right]. \tag{1.8}$$

As there is no longer a symmetry axis, there is no longer a defined Ω. The wave function of a single nucleon is thus a superposition of several Nilsson orbitals with different Ω. The parity is left the only remaining good quantum number. All states with the same parity can mix, but odd and even parity states stay uncoupled.

1.4 Collective excitations: vibrations and rotations

In some cases, the potential-energy surface has a deep, narrow minimum, meaning the nucleus has a well-defined shape. In other cases, the potential-energy surface has a larger, shallow minimum, allowing the shape of the nucleus to oscillate, or vibrate. Such vibrations are decomposed in β and γ vibrations, which are quantised independently by β and γ phonons. The nuclei in question are called β-soft and γ-soft, according to the oscillating parameter.

Once a nucleus deviates from a spherical shape, be it by vibrating or because of a constant deformation, it becomes possible for it to rotate. Prolate and oblate nuclei rotate around an axis perpendicular to the symmetry axis. Since triaxial nuclei have no axial symmetry, they can rotate about any axis.

The various ways in which a nucleus vibrates and rotates are made apparent by the band structure in its level scheme, as described by the collective model introduced by Bohr and Mottelson (1969-1975). For even-even nuclei, the possible

excitation energies are described by the formula

$$E_{n_\beta,n_\gamma}(I) = \hbar\omega_\beta\left(n_\beta + \frac{1}{2}\right) + \hbar\omega_\gamma\left(2n_\gamma + 1 + \frac{|K|}{2}\right) + \frac{\hbar^2}{2\mathfrak{I}}(I(I+1) - K^2), \quad (1.9)$$

where n_β and n_γ are the number of β and γ phonons, respectively, and $\mathfrak{I}$ is the moment of inertia of the nucleus. The first term in the sum describes β-vibrations of frequency ω_β. The second term describes γ-vibrations of frequency ω_γ, including the apparent γ vibrations caused by rotations about the intrinsic z-axis. The last term describes rotations with angular momentum I. For $K = 0$, the symmetry of the nucleus only allows even I for positive parity.

Upon each vibrational state created by the first two terms, the last term builds a rotational band, recognisable by the characteristic $I(I+1)$ spacing of the energy levels.

The picture is more complex for nuclei with odd proton or neutron number. Only the even-odd case is relevant to this work and will be discussed here.

Nuclei with a single odd nucleon are commonly described by the particle-rotor model, which views the system as a single particle coupled to an even-even core. The total angular momentum $\boldsymbol{I}$ is the sum of the angular momentum $\boldsymbol{j}$ of the odd particle, and the collective angular momentum $\boldsymbol{R}$ of the core.

There are two competing mechanisms which determine how the odd particle couples to the core. Each orbital in the Nilsson model corresponds to a single value of Ω, making it energetically favourable to rotate with a constant Ω. Such rotation is called deformation aligned. Pulling the other way is the Coriolis effect: the system gains energy by aligning the angular momentum of the odd nucleon with that of the core. This is called rotation alignment.

The balance between these two opposing forces determines the coupling of the odd nucleon to the even-even core. The coupling manifests in the rotational bands of the nucleus, and we can recognise it by comparing with the two limits shown in figures 2.5 and 2.6.

In the deformation aligned limit, $K = \Omega$ is a constant of motion, and the Coriolis effect is approximated in first order perturbation theory. The energy levels of the rotational band are thus given by:

$$E(I) = |e_\Omega - \lambda| + \frac{\hbar^2}{2\mathfrak{I}}\big[I(I+1) + j(j+1) - 2\Omega K + \delta_{K,1/2}a(-1)^{I+1/2}(I+1/2)\big], \quad (1.10)$$

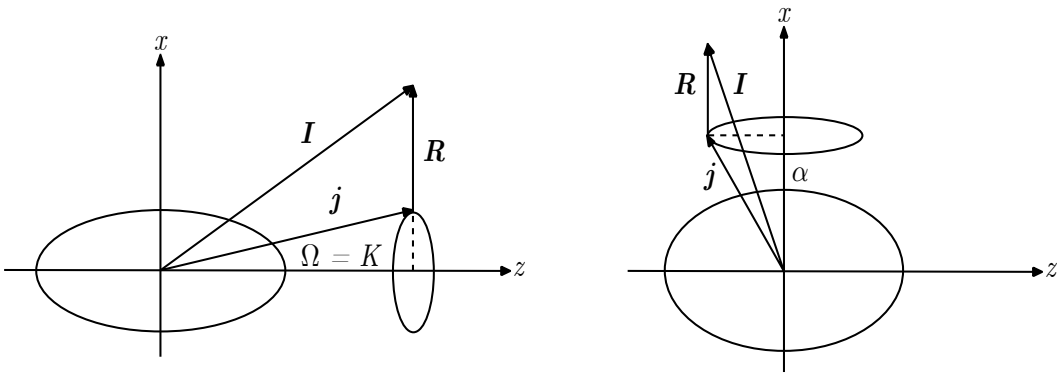

Figure 2.5: Schematic illustration of the two particle-rotor coupling limits: deformation alignment (left) and rotation alignment (right).

where the first term is the excitation of the odd nucleon relative to the Fermi level. The resulting bands are strongly coupled, as exemplified in figure 2.6.

For $K = 1/2$, the Coriolis effect results in the decoupling parameter a, causing alternating parity levels to increase and decrease in energy, decoupling the bands. $K = 1/2$ -bands are not studied in this work and will not be discussed further.

In the rotation aligned limit, the constant of motion is α (see figure 2.5), and the energy levels of the rotational bands are given by:

$$E(I) = \sum_{\Omega} 2\Big[D^{j}_{\alpha\Omega}\Big(0, \frac{\pi}{2}, 0\Big)\Big]^2 \big(e_\Omega - e_{1/2}\big) + \frac{\hbar^2}{2\mathfrak{J}}[I(I+1) + j(j+1) - 2I\alpha]. \quad (1.11)$$

Once again, the first term is the contribution of the odd nucleon, whose wave function is now spread over multiple orbitals. The energetically favoured band is made by $\alpha = j$, and the resulting spin states are $I = R + j$, where R is even. Full alignment is rare, and a second, unfavoured band created from $\alpha = j - 1$ is usually observed at higher energies. Due to this large difference in energy, these two bands are weakly coupled, as exemplified in figure 2.6.

1.5 Transitions

The transitions between energy levels are characterised by their reduced transition probabilities $B(\sigma\lambda)$, where σ is the type of transition – electric (E) or magnetic (M) – and 2^λ is the multipole order of the emitted radiation. These are

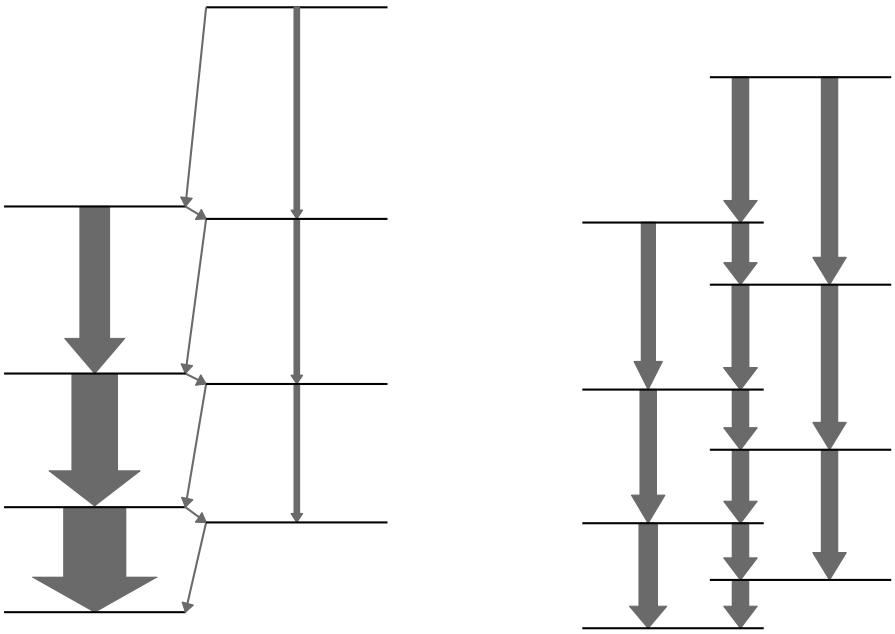

Figure 2.6: Schematic illustration of the general structure of weakly coupled rotation aligned bands (left) and strongly coupled deformation aligned bands (right).

independent of the transition energy and contain information about the wave functions of the initial and final states. $B(\sigma\lambda)$ is related to the decay probability $T(\sigma\lambda)$ by the formula

$$T(\sigma\lambda) = \frac{8\pi(\lambda+1)}{\lambda\hbar[(2\lambda+1)!!]^2}\left(\frac{E_\gamma}{\hbar c}\right)^{2\lambda+1} B(\sigma\lambda), \tag{1.12}$$

where E_γ is the energy difference between the initial and final states, and c is the speed of light in vacuum. For a single transition from level L_i to level L_j, the decay probability is $T(\sigma\lambda; L_i \rightarrow L_j) = b_{ij}T(\sigma\lambda)$, where b_{ij} is the branching ratio from L_i to L_j. The lifetime τ_i of a state being the inverse of the total decay probability of that state, equation (1.12), can be written for a specific transition as

$$\frac{b_{ij}}{\tau_i} = \frac{8\pi(\lambda+1)}{\lambda\hbar[(2\lambda+1)!!]^2}\left(\frac{E_\gamma}{\hbar c}\right)^{2\lambda+1} B(\sigma\lambda; I_i \rightarrow I_j). \tag{1.13}$$

This work considers electric quadrupole ($\sigma\lambda = E2$) transitions, for which the total transition probability is

$$T(E2) = 1.225 \times 10^9 E_\gamma^5 B(E2)\ \mathrm{s}^{-1}. \tag{1.14}$$

The quantity $B(E2)$ characterises the $E2$ transition and follows from the structure of the specific nucleus. As such, it is common to use the $B(E2)$ values to relate experimental observations to theoretical models. $B(E2)$ is given in units of $\mathrm{e^2fm^4}$ (some publications use $\mathrm{e^2b^2}$, where 1 b = 100 $\mathrm{fm^2}$) or in Weisskopf units, where 1 w.u. = $5.94 \times 10^{-2} A^{4/3}$ $\mathrm{e^2fm^4}$ is an estimate of the single particle transition between shell model states.

In many cases, it can be assumed that the nuclear shape is fully described by the quadrupole moment, with no significant higher order deformation. For a rotating, axially symmetric nucleus, the intrinsic quadrupole moment Q_0 can then be related to the $B(E2)$ value by the Clebsch-Gordan coefficients, as

$$B(E2; I_i \to I_j) = \frac{5}{16\pi}(Q_0)^2 \left\langle I_i K 20 | I_j K \right\rangle^2 . \tag{1.15}$$

The quadrupole moment calculated from the $B(E2)$ values is called the transitional quadrupole moment Q_t to differentiate the it from the physical Q_0, though it is generally considered a good approximation.

1.6 The generalised triaxial rotor model

The triaxial rotor model was first introduced by Davydov and Filippov (1958) to describe the energy states and transitions in nuclei without axial symmetry. This original model assumed nuclear rotations to be described by irrotational flow. The generalised triaxial rotor model (GTRM) applied in this work was introduced by Wood et al. (2004) and developed by Allmond (2007). It describes rotation by three unique moments of inertia, and avoids any assumptions as to its nature.

The GTRM features two parameters which describe the $E2$ properties, namely the transitional quadrupole moment Q_t and the asymmetry angle γ. The former is related to the deformation magnitude by

$$\beta = Q_t \frac{\sqrt{5\pi}}{3ZeR_0^2}, \tag{1.16}$$

where Z is the proton number, e is the elementary charge, and $R_0 = 1.2\ \mathrm{fm} \cdot A^{1/3}$ is the nuclear radius.

The other parameters are the mixing angles Γ_I between the even spin energy states in the ground state and γ bands. These are described theoretically by the relation

$$\tan(2\Gamma_I) = \sqrt{\frac{(I-1)I(I+1)(I+2)}{24}}\tan(2\Gamma_2). \tag{1.17}$$

Analytical expressions can be found (Allmond 2007) for all $B(E2)$ values in the ground state band and one phonon γ-band in terms of the parameters Q_t, γ and Γ_I, and the Clebsch-Gordan coefficients. By using equation 1.17, the number of parameters is reduced to three: Q_t, γ and Γ_2. Measurements of the transitions $2_1 \rightarrow 0_1$, $2_2 \rightarrow 0_2$ and $2_2 \rightarrow 2_1$ then produce a system of three equations with three unknowns, enough to fully solve the model. If a nucleus is well described by this model, it can be used to gain information about its deformation, and in particular its degree of triaxiality.

2 Ruthenium: a rare case of triaxiality in the ground state

The level schemes of ^{109}Ru and ^{111}Ru both show weakly coupled negative parity bands based on the $1h_{11/2}$ intruder seen in figure 2.4. Because of the mixing in triaxial nuclei, the band cannot be assigned to a single Nilsson orbital. Nevertheless, the orbital contributing most strongly can be determined. In the former nucleus, this is the 5/2[532] orbital (Kumar, Chen, and Kondev 2016). In the latter, experimental and theoretical studies by Urban et al. (2004) and Droste et al. (2004) indicate the main contribution to be the 7/2[523] orbital, with an admixture of the 5/2[532].

In both cases, the high spin of the $1h_{11/2}$ intruder generates a very strong Coriolis interaction, hence the rotation alignment.

The evolution of Ruthenium isotopes from prolate to oblate deformation passing through triaxiality has been predicted by multiple different theoretical calculations.

Macroscopic-microscopic calculations performed by Möller et al. (2008) for even-even nuclei find the "largest effect of triaxial deformations on the energy of the ground state for ^{108}Ru". Their calculations predict rigid triaxiality in ^{108}Ru, with increasing γ-softness on either side leading to a prolate ^{98}Ru and oblate ^{120}Ru.

Delaroche et al. (2010) performed fully microscopic global beyond mean field calculations in constrained Hartree-Fock-Bogoliubov (CHFB) theory with the Gogny D1S effective interaction, using a five dimensional collective Hamiltonian (5DCH). Their results indicate maximal triaxial deformation in ^{110}Ru, but with still a high degree of γ-softness. The very neutron-rich isotopes are predicted to be approximately spherical, rather than oblate.

Calculations using a cranked Skyrme HFB model by Zhang et al. (2015) predict strong triaxial deformations in ^{108,110,112}Ru. Triaxial projected shell model calculations performed by Zhang et al. (2015) predict similar well-deformed triaxial ground state minima.

Beyond-mean-field calculation by Shi and Li (2018) using a relativistic mean field (RMF) and 5DCH show an earlier onset of triaxiality, with ^{104}Ru already being well deformed, maximal triaxiality in ^{108}Ru, and subsequent isotopes leaning towards γ-soft oblate deformations.

Sugawara (2019) has applied the GTRM with variable moments of inertia to reproduce the energy levels and branching ratios in the γ-bands of ^{108,110,112}Ru. The calculations obtain stable asymmetry angles around $\gamma = 20^\circ$ for the spin states below 6^+.

These calculations all predict some degree of triaxial deformation in neutron-rich Ruthenium isotopes. However, as we can see, the magnitude and location of the deformation varies significantly; we need experimental evidence to compare with the models.

The level schemes of ^{109,110,111,112}Ru have been extended by Wu et al. (2006), showing band crossings consistent with a triaxial shape transition in ^{111}Ru.

The transition probabilities in the ground state and one phonon γ-bands of ^{110}Ru have been measured up to the 6_1^+ and 3_1^+ energy levels by Doherty et al. (2017) using multi-step Coulomb excitation. Comparison with GTRM and Gogny CHFB + 5DCH calculations indicate a high degree of triaxiality ($\gamma \sim 30^\circ$) with some γ-softness.

Higher spin transition up to $16_1^+ \rightarrow 14_1^+$ have been measured for ^{108,110,112}Ru by Snyder et al. (2013) using the Doppler shift attenuation method.

In this thesis, we expand the work done on ^{110}Ru by providing data for transitions between those measured by Doherty et al. (2017) and those measured by Snyder et al. (2013). In addition, we provide data on the hitherto little studied transition probabilities of the odd-A isotopes ^{109}Ru and ^{111}Ru.

Chapter 3

The experiment

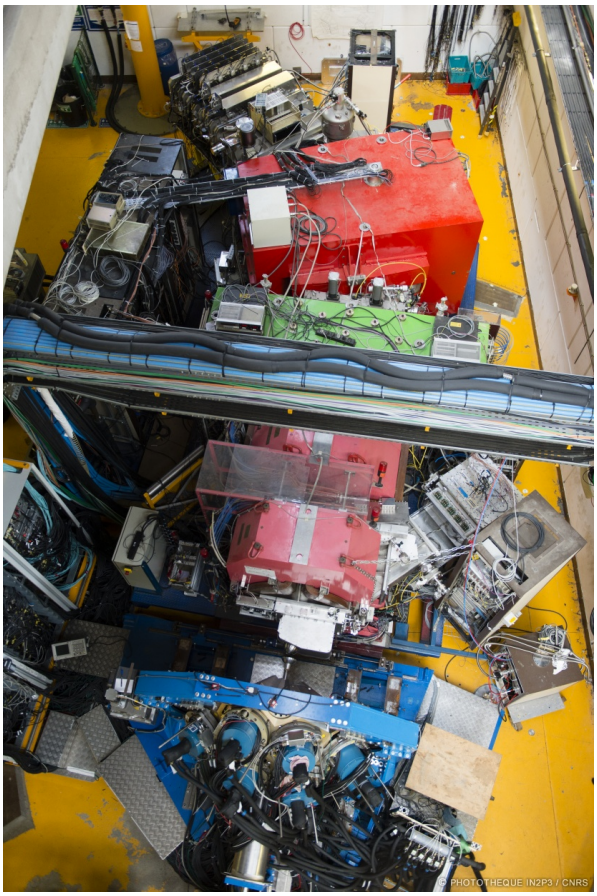

(a) Photography of the experimental setup. Image credit: CNRS/CEA/P.Stroppa.

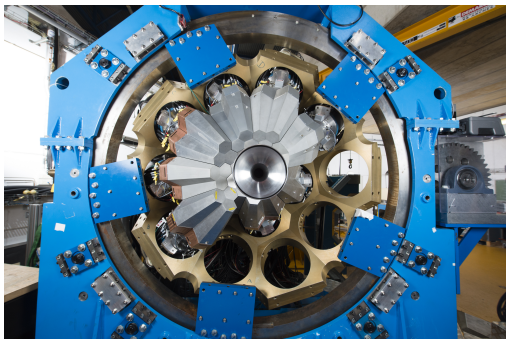

(b) Photography of AGATA. Image credit: Emmanuel Clément, GANIL.

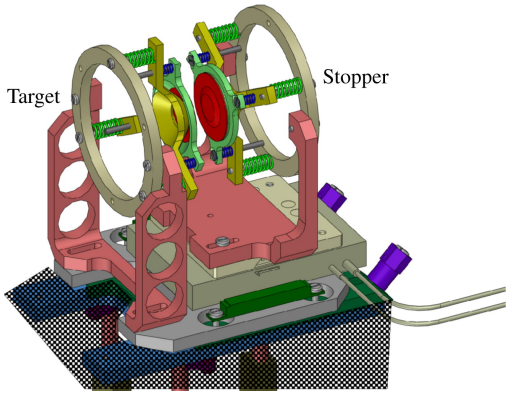

(c) Three dimensional view of the Orsay Plunger. Figure taken from Ljungvall et al. (2012).

1 Overview

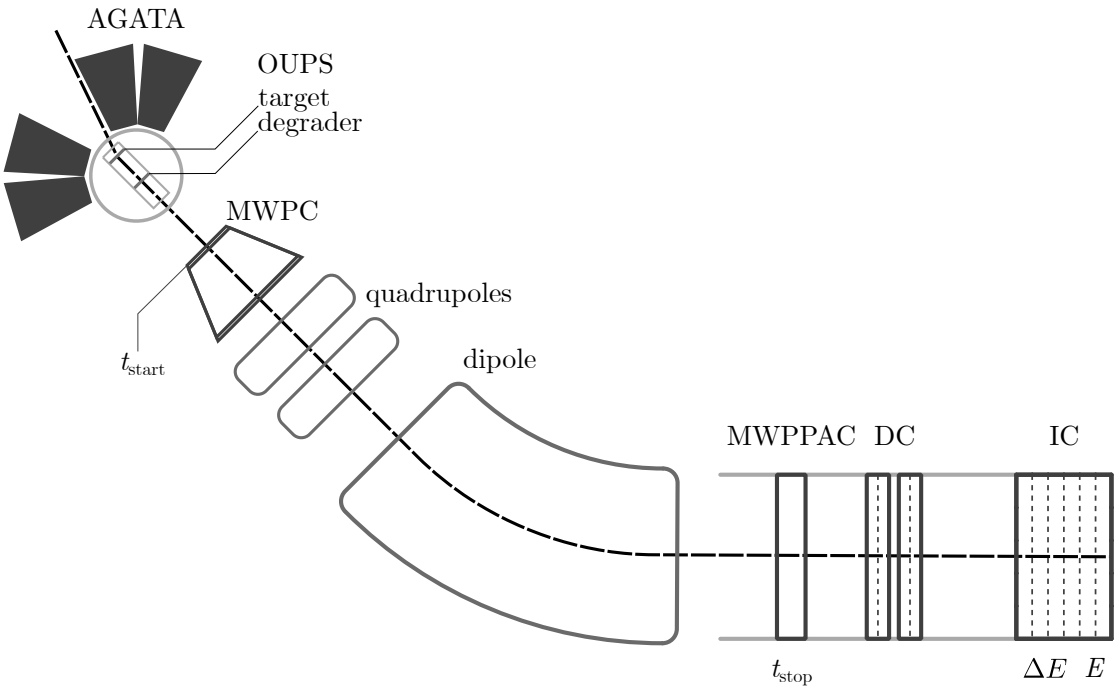

Figure 3.2: Schematic of the experimental setup. The beam is generated by the CSS1 cyclotron not shown in the figure.

The experimental setup, illustrated in figure 3.2, can be divided into three sections. First, the CSS1 cyclotron accelerates a beam of ^{238}U and sends it to collide with a ^{9}Be target at 6.2 MeV/u. This energy is just above the Coulomb barrier for the $^{238}\text{U} + {}^{9}\text{Be}$ system, inducing the fusion fission reaction $^{238}\text{U}(^{9}\text{Be}, \text{f})$ as the dominating process. Due to conservation of momentum, the fission fragments exit the target with velocities around 0.12 c. Because the mass is primarily carried by the projectile instead of in the target, this is called an inverse kinematics reaction. As they travel, the fission fragments γ-decay. This is a much slower process than fission, taking place outside the target. The energy of the emitted γ-rays is measured in the *Advanced gamma tracking array* (AGATA) (Akkoyun et al. 2012). Finally, the *Variable mode high acceptance spectrometer* (VAMOS++) (Rejmund et al. 2011) identifies the fission fragments and measures their velocity. The optical axis is rotated 19° with respect to the incoming beam to align with the maximum number of fission fragments. The magnetic rigidity of VAMOS++ was selected to maximise the transmission of nuclei around ^{104}Mo.

Not all photons will deposit all their energy at once in a detector. Compton scattering within the detector is a major contributor to background and reduced efficiency. AGATA uses pulse shape analysis and γ-ray tracking to reconstruct Compton scattering events, thereby achieving much higher efficiency than a conventional Germanium detector. This also eliminates the need for Compton shielding, allowing the detectors to cover the whole range of solid angles. A full description of the these techniques is beyond the scope of this thesis. The pulse shape analysis and γ-ray tracking was performed on-line, providing the γ-ray energies, times and angles used for further analysis.

2 The recoil distance Doppler shift method

The idea behind the recoil distance Doppler shift method (RDDS) is that γ-rays emitted by nuclei with different velocities can be separated in an energy spectrum thanks to their distinct Doppler shifts. If the velocity is then made to change abruptly at given points, the closeness of these points, rather than the time resolution of the detector, will determine the range of lifetimes which can be measured. By achieving micrometer separations, it becomes possible to measure lifetimes down to the picosecond range.

In this experiment, excited fission products are sent through a 4.5 $\mathrm{mg\,cm^{-2}}$ Magnesium degrader foil which abruptly slows them down. The beam has lost enough energy in the target that fission in the degrader is negligible.

The position of the degrader is controlled by the *Orsay universal plunger system* (OUPS) developed by Ljungvall et al. (2012). Data were taken for ten positions of the degrader, given in table 3.1. During an experiment, heating from the beam can cause variations in the target-degrader distance. To correct for this, OUPS uses a feedback system which keeps the distance constant based on the capacitance between the target and the degrader. The measurements for the three longest distances were taken without the feedback system, and the RMS was estimated from the magnitude of the feedback for the shorter distances.

At the time of the experiment, AGATA comprised 41 coaxial high-purity Germanium detector crystals, covering a solid angle of approximately 0.9π. The crystals were placed at backwards angles ranging from approximately 135° to 175°, symmetrically around the optical axis of VAMOS++. This configuration was determined to yield optimal measurements for the RDDS method (Clément et al. 2017).

Table 3.1: The distance between the target and the degrader, measured from the capacitance between them.

Distance µm	**Distance RMS** µm	**Distance RMS** %
29.8	0.5	1.67
51.6	0.3	0.58
89.9	0.6	0.66
155	2	1.29
264	5	1.89
449	4	0.89
776	40†	5.15
1170	5	0.43
1776	5	0.28
2651	5	0.19

†For the 776 µm distance, the feedback was turned off and on during the run resulting in the larger variation.

When a nucleus decays, the emitted γ-ray is detected with a red-shift given by the Doppler formula

$$E_\gamma = E_0 \frac{\sqrt{1-\beta^2}}{1-\beta\cos\theta}, \tag{2.1}$$

where E_0 is the gamma energy in the intrinsic frame of reference, $v = \beta c$ is the velocity of the fission fragment and θ is the angle of detection. A γ-ray emitted before the degrader will be more red shifted than one emitted after. If the life time is comparable to the flight time between the foils, this produces one "before" and one "after" peak in the γ-spectra, like those shown in figure 3.3. From their intensities I^{b} and I^{a} we can construct the decay curve of the decaying state. This process will be discussed in detail in the following chapter.

The superior efficiency of AGATA, combined with the larger angular coverage at sensitive backward angles, gives this data set an order of magnitude higher statistics than the previous RDDS experiment by Grente (2014) using the EXOGAM detector (Azaiez 1999). This difference is illustrated in figure 3.4. Furthermore, the position resolution provided by the pulse shape analysis allows for more precise Doppler correction and results in better energy resolution.

When the RDDS method was developed, the reaction products would typically stop completely in a thick stopper foil. Their velocity distribution was narrow and was typically determined from the separation between the two peaks. In

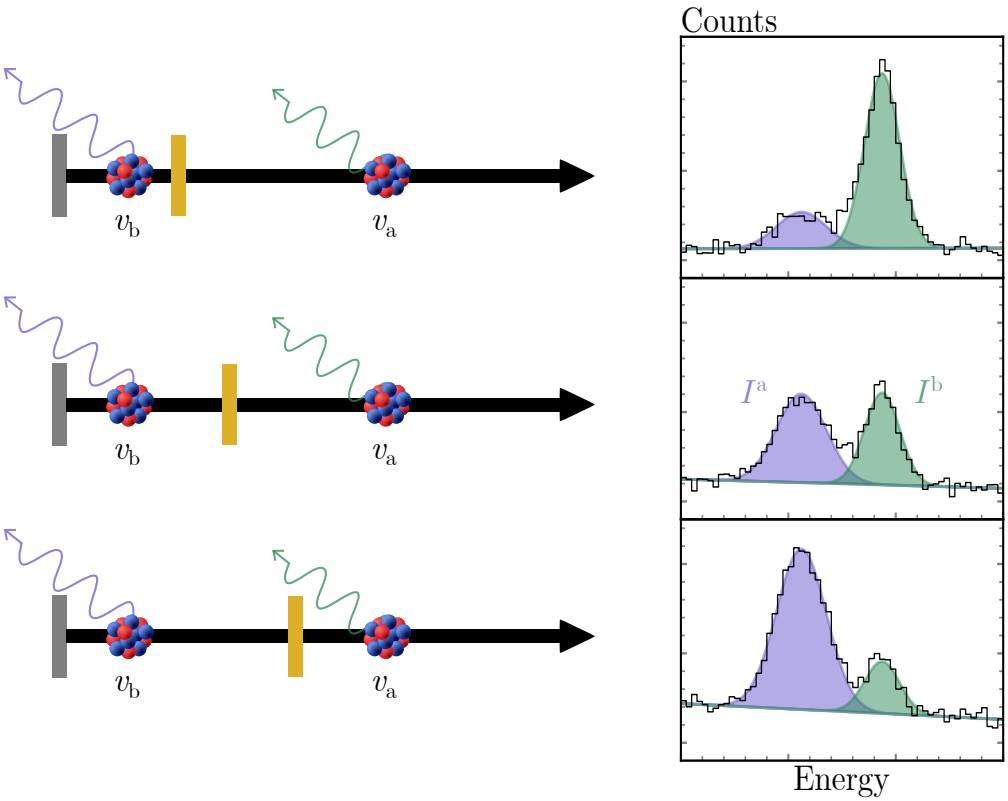

Figure 3.3: Illustration of the principle of the RDDS method.

our case, the fission fragments must be slowed down enough to measure the Doppler shift while keeping the velocity high enough to enable identification in VAMOS++. This is made possible by the inverse kinematics reaction. The resulting velocity distribution is wider and is measured in the VAMOS++ spectrometer.

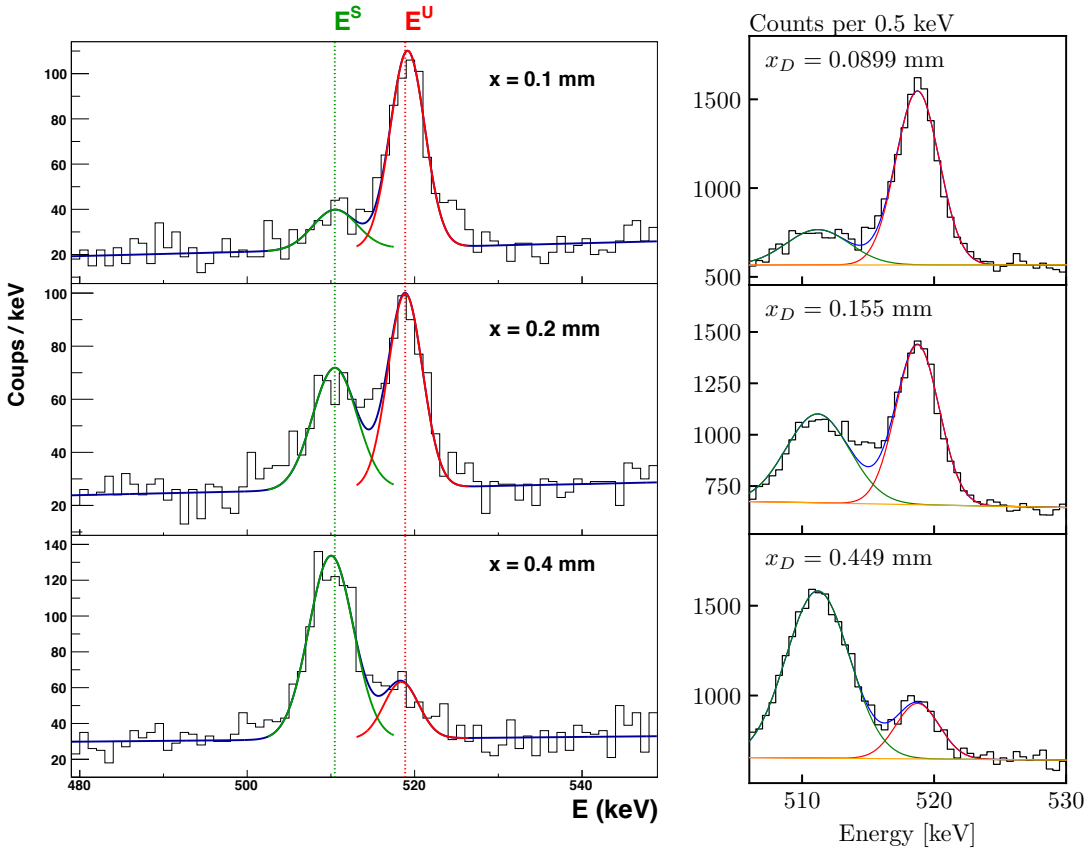

Figure 3.4: Comparison of EXOGAM (left, figure taken from Grente (2014)) and AGATA (right) peaks for the $6_1^+ \rightarrow 4_1^+$ transition in ^{104}Mo. Note the binning of 0.5 keV for AGATA against 1 keV for EXOGAM.

3 Particle identification

VAMOS++ was used to identify and measure the velocity of each fission fragment. The schematic in figure 3.2 shows the detectors and electromagnets constituting VAMOS++.

A fission fragment first passes through a dual multi-wire proportional counter (MWPC) which measures its position and sends a first timing signal. Following two quadrupole magnets which focus it horizontally and vertically, a magnetic dipole then bends it according to its magnetic rigidity

$$\mathbf{B}\rho = \frac{M}{Q}v. \tag{3.1}$$

Once the fission fragment exits the dipole a multi-wire parallel plate avalanche counter (MWPPAC) sends a second timing signal, which along with the first gives the time of flight. The position in the focal plane – which now depends on the magnetic rigidity – and the angle of the trajectory relative to the optical axis are measured in two 2 × 160-pad drift chambers (DC). Finally, the fission fragment enters a 6 × 5-pad ionisation chamber (IC) at the end of which it has deposited all its energy.

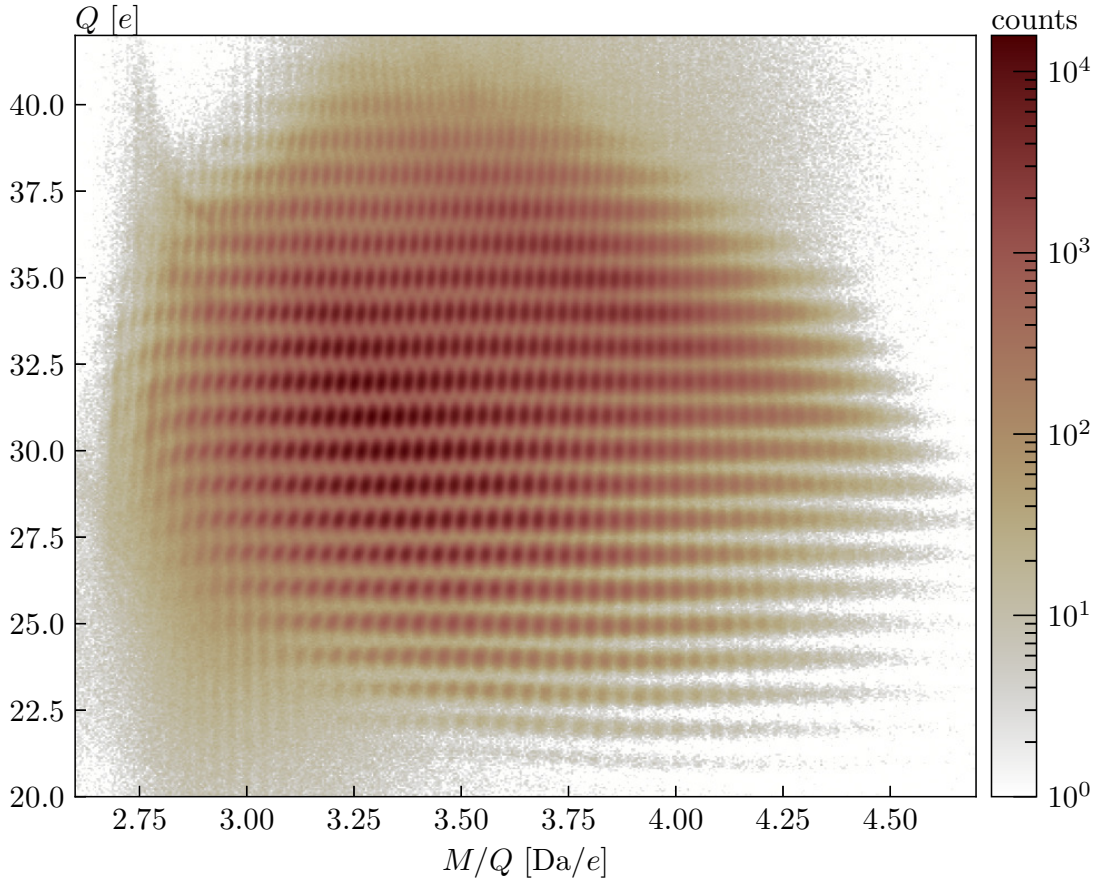

Figure 3.5: Calibrated Q vs M/Q matrix for the longest target-degrader distance $x_d = 2651 \pm 5$ µm. The bin dimensions are 0.5 e × 0.005 Da/e.

The trajectory of the fission fragment is determined from the positions and angles recorded by the MWPC and the DC. The bending through the dipole gives the magnetic rigidity $B\rho$ of the fission fragment, and the length of the trajectory combined with the time of flight gives its velocity v. The mass of the fission

fragment is then determined by relating the velocity v to the total energy E deposited in the IC, and its charge Q is obtained by inserting M, v and $B\rho$ into equation 3.1. After calibration, the events can be sorted as in figure 3.5 *

Finally the fission fragment's proton number Z is determined using the ΔE-E method, which measures the energy change as a particle passes through a detector material as a function of the total particle energy. Since the total energy depends on A and the rate of energy loss for a given A depends on charge, the fission fragment is uniquely identified in this way. A ΔE:E matrix for this experiment is shown in figure 3.6.

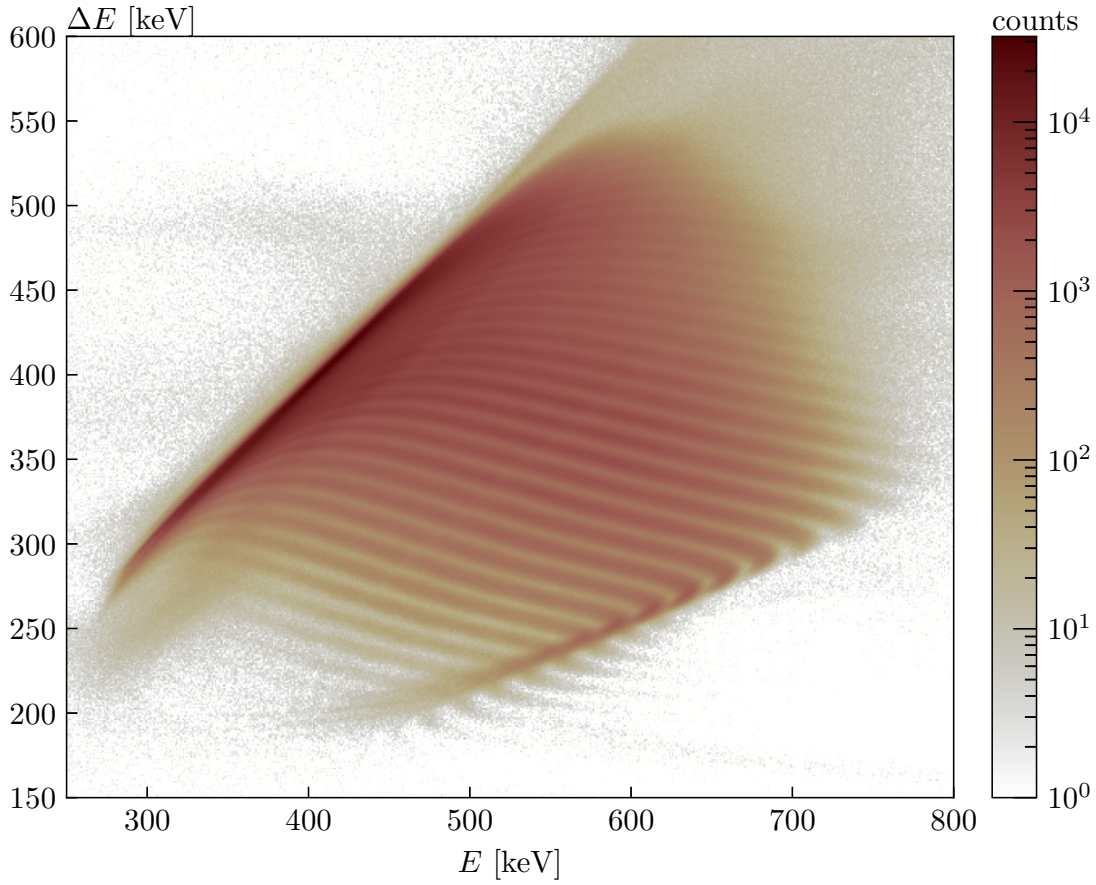

Figure 3.6: ΔE:E matrix of the events recorded for the longest target-degrader distance $x_d = 2651 \pm 5$ µm. The bin dimensions are 1 keV × 1 keV.

*Mass is given in units of dalton (Da), which is the recommended name and symbol equivalent to the atomic mass unit (u). 1 Da = 1.660 539 066 60(50) × 10^{-27} kg.

The velocity v_b before the degrader (see figure 3.3) was reconstructed event by event, based the Doppler shift measured in AGATA for each separate Z. This value is crucial for the lifetime extraction, the topic of the next chapter.

The calibration of VAMOS++ and event-by-event particle trajectory reconstruction was performed by other members of the collaboration. The resulting Z vs M identification plot is shown in figure 3.7.

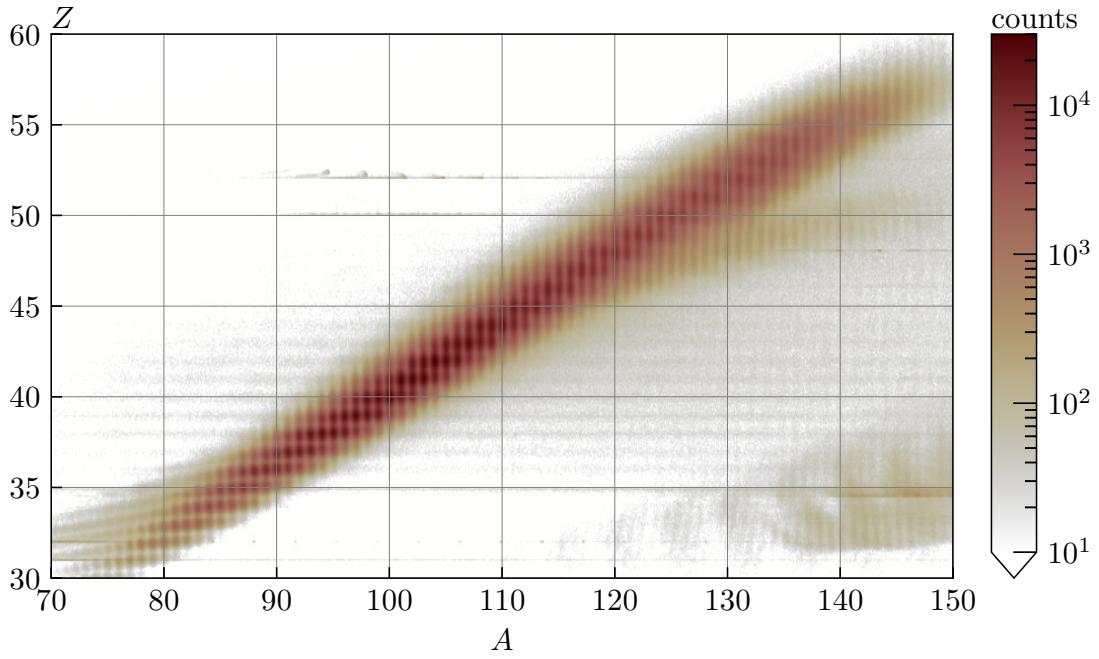

Figure 3.7: Identification plot showing the multitude of nuclei populated in the experiment. Here with the events recorded for the longest target-degrader distance $x_d = 2651 \pm 5$ µm. The bin dimensions are 0.1×0.1.

Chapter 4

The data analysis

1 Event selection

Following the calibration of VAMOS++ and the sorting of the data as described in the previous section, the data were organised in a ROOT tree, where each event had an energy and an angle detected in AGATA and corresponding Z, A and β values from VAMOS++. This was the starting point for our analysis.

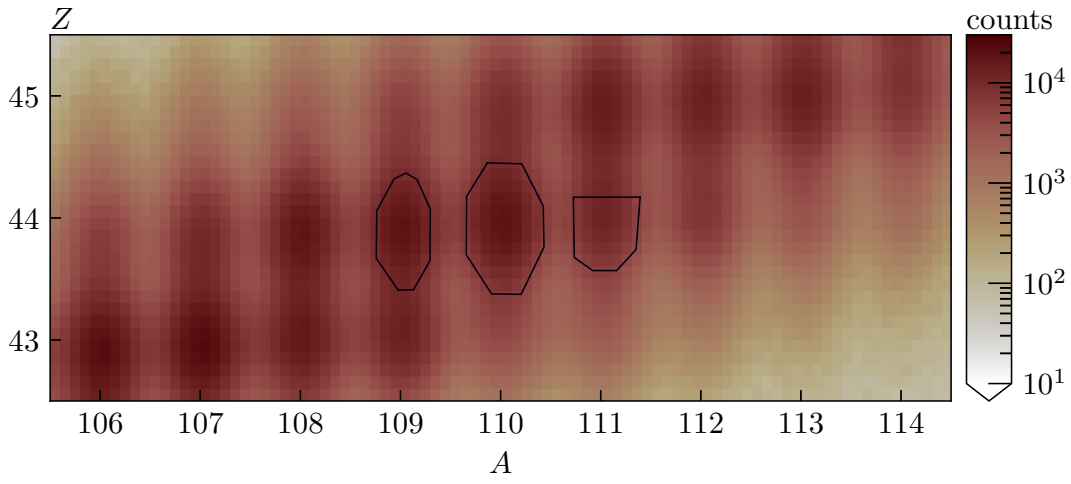

Figure 4.1: Zoom on events corresponding to Ruthenium ($Z = 44$) isotopes in the identification plot. The two-dimensional gates are drawn for the three isotopes analysed in this work.

Figure 4.1 shows a zoom on the events corresponding to the decay of Ruthenium ($Z = 44$) isotopes. To extract these events, we applied the two-dimensional gates on (Z, A) indicated on the figure. We discovered that the precise location of the distribution for each nuclide varied slightly between the distances. As the offset appeared to be approximately equal for all nuclides, we determined the gates for the 776 µm distance, and applied a correction to each of the others. This correction is shown for ^{110}Ru in figure 4.2.

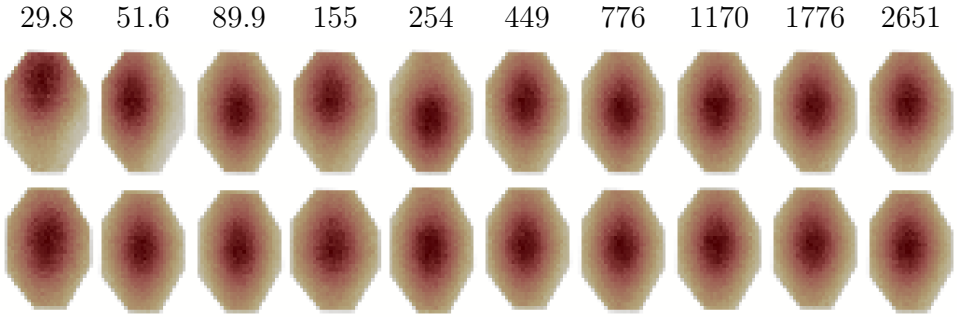

ΔM	−0.03	−0.09	0.00	−0.02	+0.01	+0.01	0.00	0.00	0.00	0.00
ΔZ	+0.22	+0.09	−0.01	+0.10	−0.07	+0.07	0.00	+0.01	+0.02	+0.04

Figure 4.2: Gate on ^{110}Ru defined for the 776 µm distance without correction (top) and with correction (bottom). The maximum of the colour map is different in each case to best show the distribution. The applied correction is noted for each distance.

The two-dimensional gates on (Z, A) allow us to project γ-rays originating from a given nuclide, but inevitably also selects those from the complementary fission fragments produced in the reaction. Because these all travel at different velocities and angles, they do not appear as peaks in the γ-spectra, but contribute to a smooth background.

The ΔE-E method relies on being able to distinguish the ΔE "bananas" shown in figure 3.6. As the figure shows, this becomes impossible when E is close to ΔE, as they all merge together. For this reason, we extracted only events for which $E - \Delta E > 20$.

As can be seen in figure 4.1, the event distribution corresponding to ^{111}Ru overlaps with that of $^{111}_{45}$Rh. Clean spectra necessitated further gating than for the stronger ^{109,110}Ru. We increased the $E - \Delta E$ threshold from 20 to 40, and defined a more restrictive gate on the (Z, A) matrix, removing the ^{111}Rh contamination.

2 The differential decay curve method

The differential decay curve method (DDCM) for analysing RDDS data was first developed by Dewald, Harissopulos, and Brentano (1989), and later reviewed by Dewald, Möller, and Petkov (2012). It allows the determination of lifetimes from relative quantities which can be obtained directly from measured γ-spectra, and makes systematic errors related to feeding transitions evident.

In the interest of clarity, in particular with regards to notation, we will go through the derivation of the DDCM here.

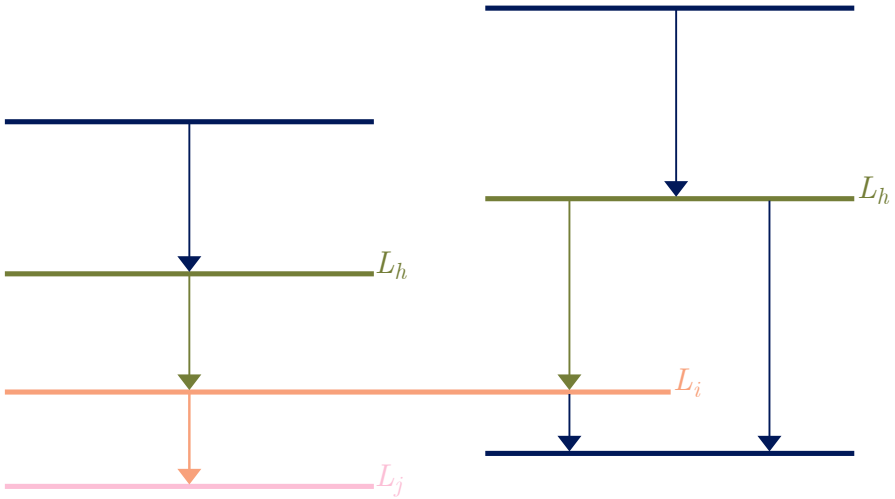

Figure 4.3: Illustrative decay scheme. The lifetime of level L_i is determined from the decay to level L_j and the feeding from levels L_h.

Consider a level L_i which is fed by the levels L_h and decays a level L_j, as illustrated in figure 4.3. The number of nuclei n_i in L_i is described by the differential equation

$$\frac{\mathrm{d}n_i(t)}{\mathrm{d}t} = -\lambda_i n_i(t) + \sum_h \lambda_h b_{hi} n_h(t), \tag{2.1}$$

where $\lambda = \tau^{-1}$ is the decay constant and b_{hi} is the branching ratio for the transition $h \rightarrow i$. We denote $R_i(t)$ the number of nuclei which have yet to decay from level L_i at time t. This function is called the decay curve. Similarly, $F_i(t)$ is called the flight curve and is the number of nuclei which have decayed. From this definition, it follows that

$$R_i(t) = \lambda_i \int_t^\infty n_i(t')\,\mathrm{d}t'\,, \tag{2.2}$$

that is the number of decays from L_i occurring after time t.

All nuclei will eventually decay to the ground state L_0. In mathematical terms, $\lim_{t\to\infty} n_i(t) = 0$. Using this, we can integrate the left hand side of equation (2.1) and get

$$\int_t^\infty \frac{\mathrm{d}n_i(t')}{\mathrm{d}t'}\,\mathrm{d}t' = \lim_{t'\to\infty} n_i(t') - n_i(t) = \sum_h b_{hi}R_h(t) - R_i(t). \tag{2.3}$$

We insert this result into the derivative of equation (2.2) to obtain,

$$\frac{\mathrm{d}R_i(t)}{\mathrm{d}t} = -\lambda_i n_i(t) = \lambda_i\left[\sum_h b_{hi}R_h(t) - R_i(t)\right], \tag{2.4}$$

which can be rearranged as such to give the lifetime of the state L_i:

$$\tau_i = \frac{1}{\lambda_i} = \frac{\mathrm{d}R_i(t)}{\mathrm{d}t}^{-1}\left[\sum_h b_{hi}R_h(t) - R_i(t)\right]. \tag{2.5}$$

Ideally, we expect this expression to be constant over all t.

Now we need to rewrite equation (2.5) in terms of measurable quantities. Namely the intensities I_{ij}^{b} and I_{ij}^{a} introduced in the previous chapter. First we calculate the time $t_D(x) = x \cdot v_b^{-1}$ when the nucleus of interest passes through the degrader foil at position x, and write $R(x) \equiv R(t_D(x))$. Then we introduce the relative quantity

$$Q_{ij}(x) = \frac{I_{ij}^{\mathrm{a}}(x)}{I_{ij}^{\mathrm{b}}(x) + I_{ij}^{\mathrm{a}}(x)} = \frac{b_{ij}R_i(x)}{b_{ij}R_i(0)}. \tag{2.6}$$

By making this substitution in equation (2.5) we get

$$\tau_i = \left[v_b R_i(0)\frac{\mathrm{d}Q_{ij}(x)}{\mathrm{d}x}\right]^{-1}\left[\sum_h b_{hi}Q_{hi}(x)R_h(0) - Q_{ij}(x)R_i(0)\right] \tag{2.7}$$

$$= \left[v_b\frac{\mathrm{d}Q_{ij}(x)}{\mathrm{d}x}\right]^{-1}\left[\sum_h b_{ij}\alpha_{hi}Q_{hi}(x) - Q_{ij}(x)\right]. \tag{2.8}$$

The feeding coefficient α_{hi} describes the relative number of decays from the levels L_h and L_i, corrected for efficiency. It is given by

$$\alpha_{hi} = \frac{b_{hi}R_h(0)}{b_{ij}R_i(0)} = \frac{\epsilon_{ij}}{\epsilon_{hi}}\left[\frac{I_{hi}^{\mathrm{b}}(x) + I_{hi}^{\mathrm{a}}(x)}{I_{ij}^{\mathrm{b}}(x) + I_{ij}^{\mathrm{a}}(x)}\right] \quad \text{for any } x \quad , \tag{2.9}$$

where ϵ_{hi} is the relative efficiency of AGATA at the energy of the transition from L_h to L_i.

An accurate lifetime estimate hinges on finding Q_{hi} for all feeding transitions. This can prove difficult if there are several weak transitions feeding into the state of interest. Such unobserved feeding can induce a systematic error and result in an overestimate of the lifetime. This can be overcome by employing $\gamma\gamma$-coincidence analysis, where gates applied to the before degrader component of a feeding transition eliminate the influence of the feeding transitions. A drawback is that this gating excludes the majority of events, increasing the statistical uncertainty. In this work we have concentrated on single-γ analysis; the $\gamma\gamma$-coincidence technique is discussed in more detail by Dewald, Harissopulos, and Brentano (1989).

2.1 Fitting the γ-spectra

The differential decay curve method requires extracting the intensities of the two peaks for each transition. In order to fit the peaks, it is necessary to make assumptions about their shape, as well as that of the background. The peaks are described reasonably well by Gaussians, and we have approximated the background as linear under each peak.

Each of the peaks was fitted to a Gaussian function of energy

$$f(E) = \frac{A}{\sigma\sqrt{2\pi}} \exp\left(-\frac{(E-\mu)^2}{2\sigma^2}\right), \tag{2.10}$$

where A, μ and σ respectively are the area, mean and standard deviation of the Gaussian. These were added to a linear background $g(E) = aE + b$.

To achieve a consistent fit, the spectra for all distances were fitted simultaneously, with common μ and σ parameters. The total fit function for a single spectrum j was constructed as

$$F_j(E) = \sum_{i=0}^{n_{\text{peaks}}} \frac{A_{ij}}{\sigma_i\sqrt{2\pi}} \exp\left(-\frac{(E-\mu_i)^2}{2\sigma_i^2}\right) + a_j E + b_j, \tag{2.11}$$

A χ_j^2 cost function for $F_j(E)$ was constructed for each spectrum j using the `cost.LeastSquares` method implemented in `iminuit` (Dembinski and al. 2020). These were then combined into a total χ^2 cost function, where the parameters

σ_i and μ_i depend only on the peak i and the parameters a_j and b_j depend only on the spectrum number j. The area A_{ij}, corresponding to the intensity of the peak, depends on both.

Finally, the combined cost function was minimised using the Migrad algorithm (James and Roos 1975).

2.2 The feeding coefficient

The peak fitting described above gives us the values for I, and hence for Q. To complete equation (2.8), we need the detector efficiency and branching ratios.

The efficiency calibration was performed by Ansari (2019) using a ^{152}Eu source. The efficiency values were read from figure 4.4 (Ansari 2019) using pixel measurements. The uncertainty on the reading was estimated as ± 0.01. The branching ratios were obtained from the literature.

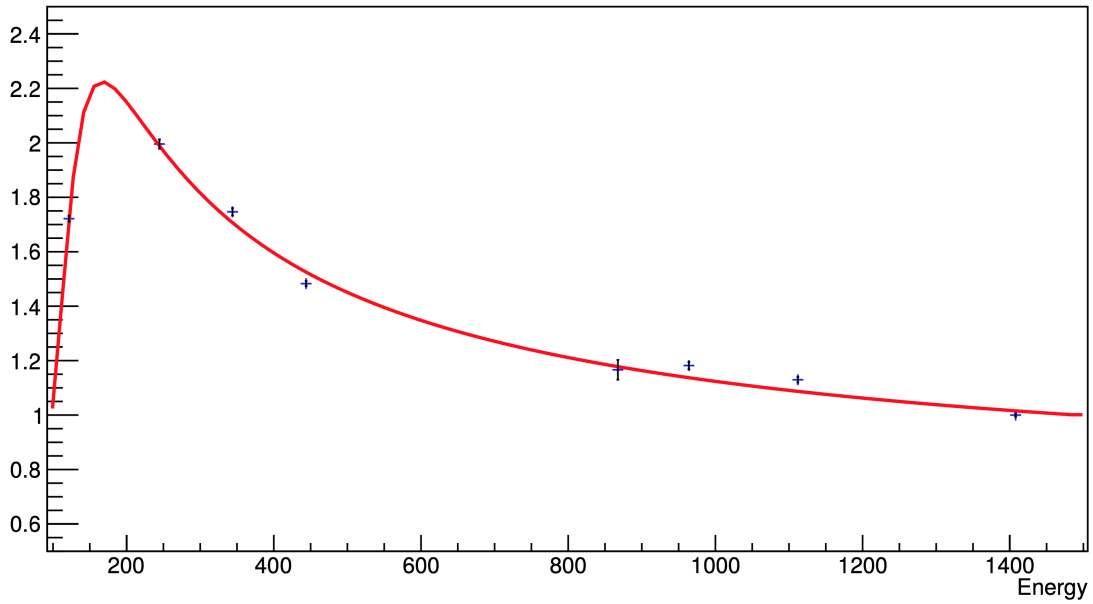

Figure 4.4: Efficiency curve normalised to 1 for 1408 keV. Figure taken from Ansari (2019).

The energy levels we study here decay primarily through γ emmission. There is however a small probability of internal conversion, given by the conversion coefficient. This coefficient tends to decrease with increasing energy, making

the feeder slightly stronger than what we measure. However, for the transitions treated here, this amounts to a correction of approximately 1%, which is well within one standard deviation of our measurements. We have therefore elected to ignore this effect.

2.3 Fitting the decay curves: the derivative constrained monotonic decay curve method

The recoil distance doppler shift method yields direct measurements of Q, but $\mathrm{d}Q/\mathrm{d}x$ must be estimated by fitting the data points. Figure 4.5 shows simulated decay curve measurements similar to those obtained with the RDDS method.

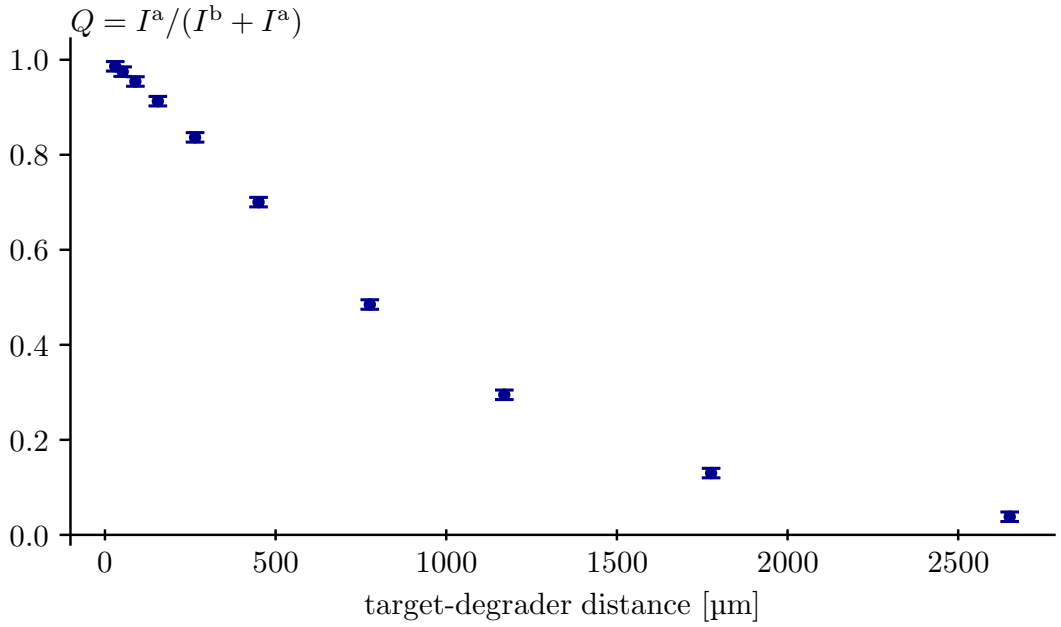

Figure 4.5: Simulated decay curve of the type one obtains with the RDDS method, corresponding to a decay with $v\tau = 700$ µm, fed by a state with $v\tau = 350$ µm and $\alpha = 0.7$.

The most widely used method is to fit a smooth continuous piecewise function comprising of quadratic polynomials to the data. The lifetime is then calculated separately for each data point. Several slightly different implementation of this

method are used. One common implementation is the Napatau software (Saha 2003). For simplicity, we will use the term "Napatau method" to refer to all implementations of this method.

The approach described above has several limitations. The low curvature sections at the start and end of the curve are not well reproduced by quadratic polynomials, which often results in the fitted curve having an unphysical shape. A sensitive region is typically defined around the steepest point of the curve, and points outside this region are discarded. The choice of this sensitive region can influence the final result. While the derivative is continuous, it is not usually constrained to be smooth. This creates an unphysical cusp at the maximum of the derivative, which is at the center of the sensitive region.

A novel method of extracting the lifetime from the measurements was developed by Modamio, Heines, and Görgen (unpublished), and was first applied in this work. This included exploration of the method's parameters and testing to identify and estimate potential sources of uncertainty. This method , which we have named the *derivative constrained monotonic decay curve method* (DCM2), is based on two primary considerations which are explained here.

The lifetime of any given state is a constant. Assuming all significant transitions are accounted for, this places an additional constraint on the fits of $Q_{hi}(x)$ and $Q_{ij}(x)$, namely that

$$\sum_h b_{ij}\alpha_{hi}Q_{hi}(x) - Q_{ij}(x) = \tau_i v_b \frac{\mathrm{d}Q_{ij}(x)}{\mathrm{d}x}. \tag{2.12}$$

In other words, we constrain the fits by the derivative, minimising not only the difference between the fitted curves and the data points, but also the difference between the two sides of equation (2.12).

With v_b known, the lifetime τ_i becomes another parameter in the fit, for which we get a single value. This eliminates the need to define a sensitive region.

The relative decay curve $Q(x)$ represents the fraction of nuclei which have yet to decay from a given level. As such, it is necessarily a monotonic, decreasing function. In some cases, especially when one of the components is close to zero, fluctuations in the measurements or in the background can results in a local increase, within the uncertainties, of the experimentally measured values. Since equation (2.8) includes a factor $\mathrm{d}Q/\mathrm{d}x$ in the denominator, such fluctuations will have a significant effect on the calculated lifetime. To mitigate this effect,

$Q(x)$ is transformed into the relative flight curve $1 - Q(x)$, which is fitted using monotonic increasing Isplines (Ramsay 1988; djmw 2012; Bloom and Crawford 2022).

The use of Isplines, while arguably better adapted to the physical situation than simple quadratic polynomials, depends on the absolute target-degrader distances. In contrast, the traditional DDCM only uses the relative distances. The use of absolute distance introduces a systematic uncertainty which could skew the result. This effect was however estimated to be negligible compared to the other sources of uncertainty in this analysis. A more detailed study of the significance of this effect will be performed in future work.

The DCM2 was tested both on simulated and measured data to characterise its statistical and systematic errors. The results of these test are presented in section 5.1.

2.4 Gating on the velocity distribution

The use of equation 2.8 requires a single velocity value. In any experiment however, the velocities will follow some distribution depending on the reaction and experimental setup. Because v appears in the denominator, the best solution – as shown by Hackstein and Dewald (2014) – is to calculate the average of the inverse velocity distribution $\langle 1/v \rangle$. In VAMOS++, the velocity distribution is particularly wide, and this can be used to our advantage.

The AGATA + VAMOS experimental setup opens up the possibility for a new method which can extract multiple data points from a single target-degrader distance. With VAMOS++, the velocity distribution can be accurately measured, and thanks to the high statistics of AGATA, it is possible to apply the DDCM to events from a subset of this distribution. By dividing the events into velocity slices, we get data corresponding to multiple different velocities, and thus to multiple different times which are closer together than the individual distances, but still far enough apart to yield different values for Q. The details of this method will be explained below using the $4_1^+ \rightarrow 2_1^+$ transition in ^{100}Zr as an example.

Figure 4.6 shows the β distribution for ^{100}Zr. The five sections, or slices, each contain between 111×10^3 and 114×10^3 events. Individual γ-spectra were extracted for each slice and fitted as described in section 2.1.

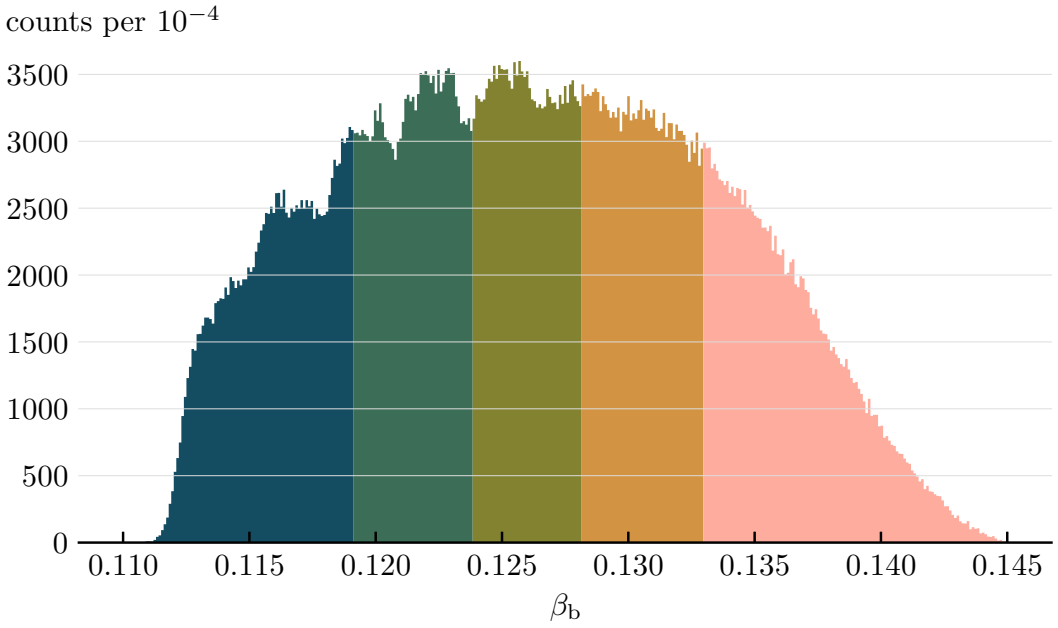

Figure 4.6: The velocity distribution of ^{100}Zr nuclei before the degrader, divided into five slices with an approximately equal number of counts.

Now, there are five sets of Q values for each distance. To separate them, the average inverse velocity $\langle\beta^{-1}\rangle$ is calculated for each slice, then multiplied by the distance to get the time $t_\mathrm{d} = x_\mathrm{d} c^{-1} \langle\beta^{-1}\rangle$ corresponding to each value of Q. The decay curve can now be plotted as a function of t_d and interpolated from fifty points, instead of ten. In this specific case however, we only performed the process for the last six distances, where Q changes quickly enough that an effect would be visible. For the 264 µm distance, we only made two velocity slices.

The resulting fit of the lifetime is displayed in figure 4.7. The top graph shows the measured relative decay values $Q_{hi}(x)$ of the feeding energy level, along with the fitted curve. The knots used in the fit are marked as dashed vertical lines. The next graph is equivalent for the energy level under study. The third graph shows the two sides of equation (2.12); the degree of overlap of these curves is an important indication of the quality of the fit. Finally, the bottom graph shows the lifetime calculated at each experimental value, as well as from the fitted curves. The fitted lifetime value is marked by a horizontal dashed line.

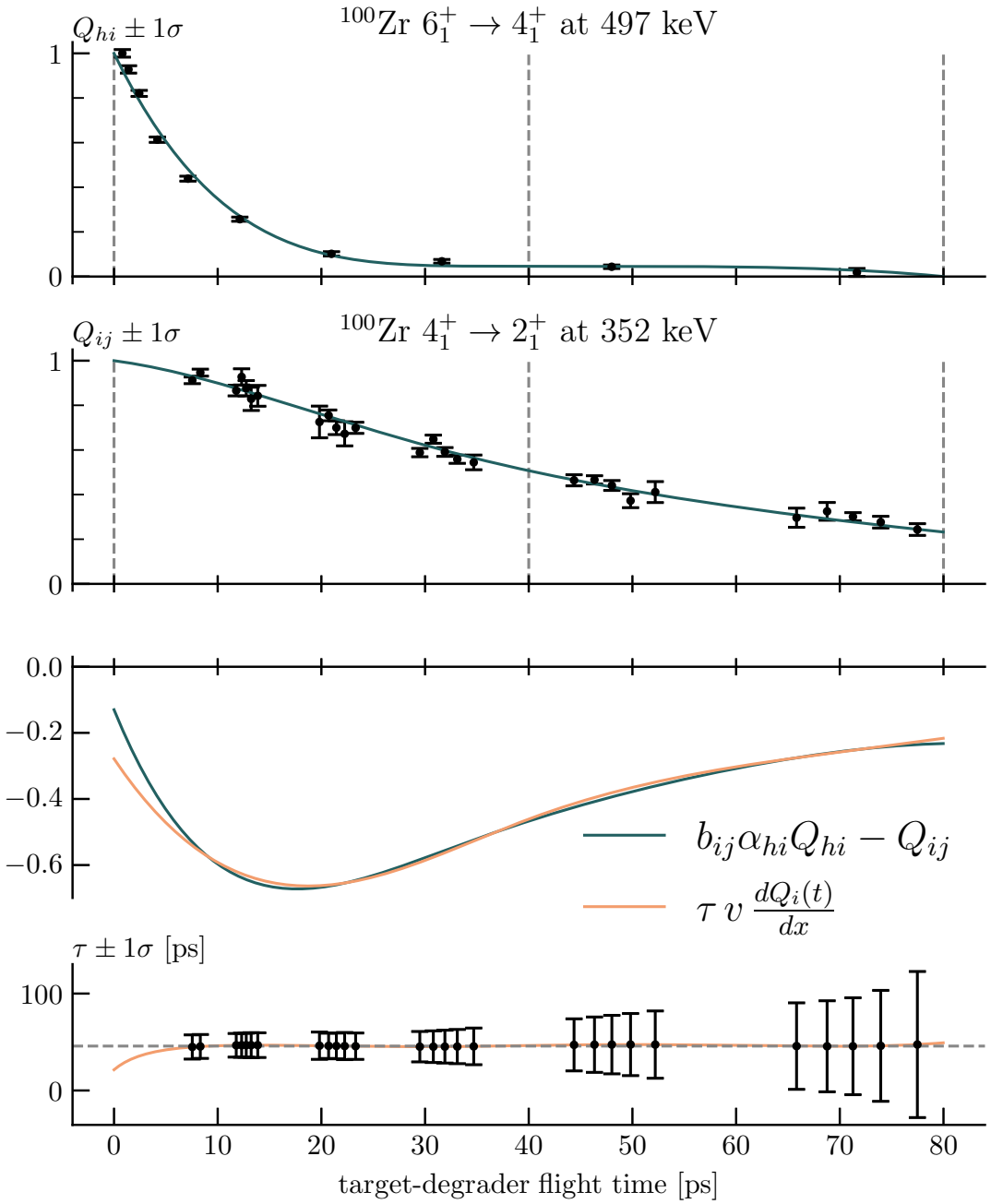

Figure 4.7: DCM2 analysis of the $4_1^+ \rightarrow 2_1^+$ decay in ^{100}Zr using sliced velocity distributions for the six longest distances. The four shortest distances have been omitted for the decaying level, see the text for details.

With this technique, we obtain lifetimes which are consistent with those obtained without velocity slicing. For the lifetime in this example however, we suspect unseen feeding might be inducing a systematic error in the estimate. Consequently, the analysis of this transition is better studied in $\gamma\gamma$ coincidences. Such an analysis is being performed by another member of the collaboration (Pasqualato et al. unpublished).

This technique achieves a similar result to the differential plunger proposed by Dewald, Harissopulos, and Brentano (1989), where multiple consecutive degrader foils are used to get multiple velocities from a single configuration.

Chapter 5

Results

This chapter presents the results of the DCM2 tests, as well as the analyses for the studied transitions, namely the first $19/2^- \rightarrow 15/2^-$ and $15/2^- \rightarrow 11/2^-$ transitions in ^{109,111}Ru, and the $6_1^+ \rightarrow 4_1^+$, $5_1^+ \rightarrow 3_1^+$ and $4_2^+ \rightarrow 2_2^+$ transitions in ^{110}Ru.

The treatment of overlapping transitions and contaminants is explained here. The fits of the individual peaks in the γ-spectra are shown in appendix A.

1 Test of the DCM2

This work was the first application of DCM2. As such it was crucial to test it in terms of accuracy and reliability.

The DCM2 includes manual selection of both the number of knots and the order of the splines used to fit the decay curves. This introduces an element of uncertainty which cannot be predicted reliably, because it depends on the person performing the analysis.

The magnitude of this effect can be estimated by performing multiple fits with different parameter combinations and comparing the results. We performed fits of a simulated decay with $\tau_i v = 700$ µm, and a single feeder with $\tau_h v = 350$ µm and $\alpha_{hi} = 0.7$. A summary of the results is shown in figure 5.1, the fits can be found in appendix B.

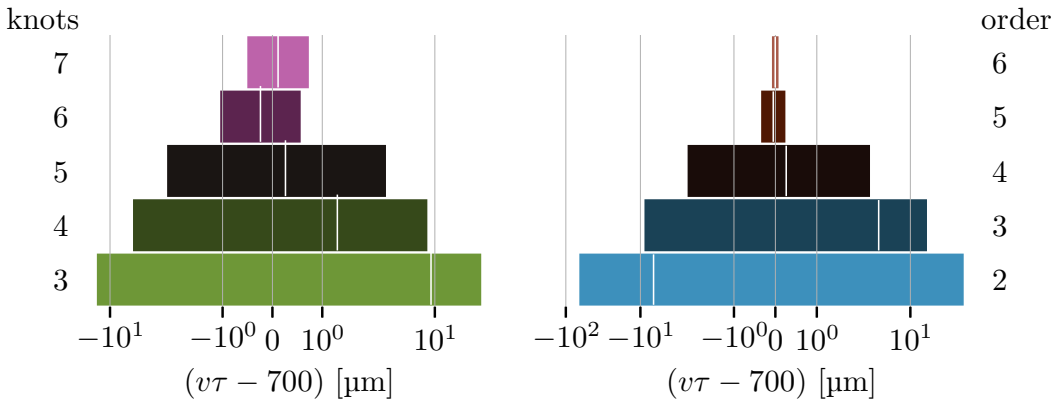

Figure 5.1: Results for fits of the simulated decay curves. Left: fourth order splines with three to seven knots. Right: five knots with splines between second and sixth order. Note the symmetrical log scale on the x-axis.

In our test cases, the DCM2 was observed to be highly robust, that is the lifetimes obtained with multiple different reasonable parameter combinations all reproduce the values used to generate the simulated data, within the uncertainties. As seen in figure 5.1, the uncertainty decreases with increasing number of free parameters. It is important to note that this was not always the case for experimental decay curves. In our analysis of the Ruthenium isotopes, the parameters were chosen on a case by case basis to yield the lowest error. A more thorough study with both simulated and experimental data, featuring various lifetimes and errors as well as multiple feeders, is needed to draw general conclusion as to the optimal parameter combinations.

To assess the accuracy of the method, we applied it to the $8_1^+, 6_1^+$ and 4_1^+ states in ^{104}Mo. The lifetimes of these states have all been measured by Smith et al. (2002) using a ^{252}Cf source in a differential plunger arrangement, as well as by Pasqualato (2022) using the DDCM with traditional fits of the decay curves on the same data used in this work, both in single-γ and $\gamma\gamma$-coincidence analysis. The values for the 4_1^+ state are compared in figure 5.2. The same pattern was observed for the other lifetimes.

We found that the lifetimes we obtain with the DCM2 in single-γ analysis are consistent with those obtained with the Napatau method. The shorter lifetimes obtained in $\gamma\gamma$-coincidence analysis can be explained by the elimination of unseen feeders, and the larger uncertainty by the lower statistics. This also illus-

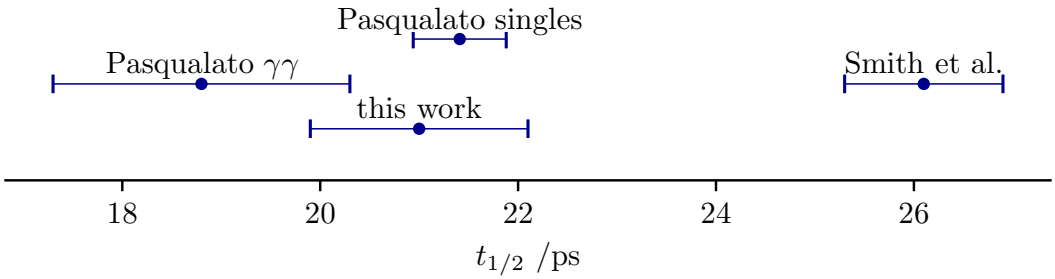

Figure 5.2: Comparison of the lifetimes of the 4_1^+ excited state of ^{104}Mo, as calculated with the DCM2 (this work) and the Napatau method (Pasqualato 2022), along with the adopted value (Smith et al. 2002).

trates the value of $\gamma\gamma$-coincidence analysis to obtain reliable results. The measurements derived from the present dataset do, however, yield significantly shorter lifetimes than the ^{252}Cf decay measurements.

2 Ruthenium isotopes.

The results of the analysis are shown in figures 5.5, 5.6, 5.10, 5.11 and 5.14 to 5.16. These all share the same setup. The top graph shows the measured relative decay values $Q_{hi}(x)$ of the feeding energy level, along with the fitted curve. The knots used in the fit are marked as dashed vertical lines. The next graph is equivalent for the energy level under study. The third graph shows the two sides of equation (2.12); the degree of overlap of these curves is an important indication of the quality of the fit. Finally, the bottom graph shows the lifetime calculated at each experimental value, as well as from the fitted curves. The fitted lifetime value is marked by a horizontal dashed line. To show the points contributing significantly to the lifetime estimate, the y-axis has been limited around these values. Note that in each case, the fitted lifetime value is within one standard deviation of the values outside the y-axis range.

In most cases, the feeding coefficient α was taken as the average value $\langle\alpha\rangle$ over all distances. Deviation from this is stated for the concerned cases.

2.1 ^{109}Ru

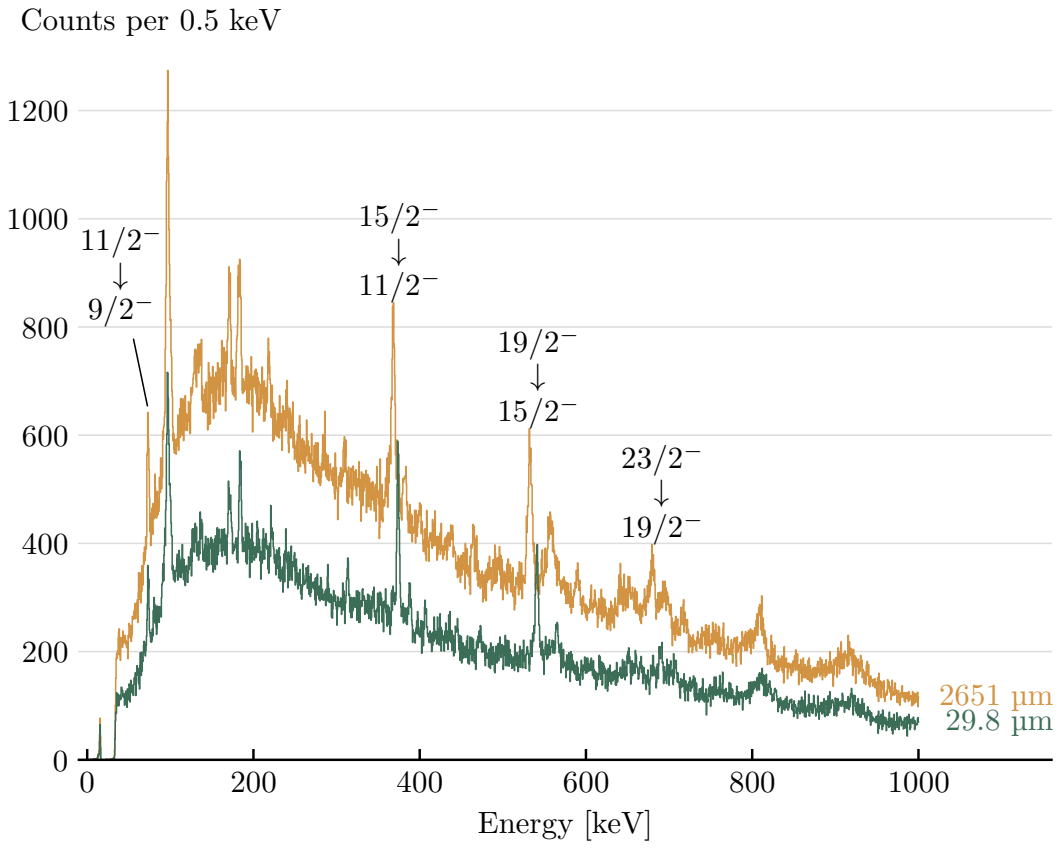

Figure 5.3: The γ-spectra for ^{109}Ru taken at the shortest and longest plunger distance. The labeled peaks correspond to the transitions highlighted in figure 5.4.

The γ-spectra for ^{109}Ru with the shortest and longest plunger distance are displayed in figure 5.3. Figure 5.4 shows a partial level scheme in which the studied transitions are highlighted. The other transitions feeding into the studied levels were not visible in the γ-spectra. Only one previous publication (Ding Huai-Bo et al. 2009) has claimed the observation of the low-energy M1 transitions from $15/2_1^-$ and $19/2_1^-$. This, however, without showing evidence or providing intensities. As we do not see any evidence for these transitions in our spectra, it can be assumed that these decay branches are negligible.

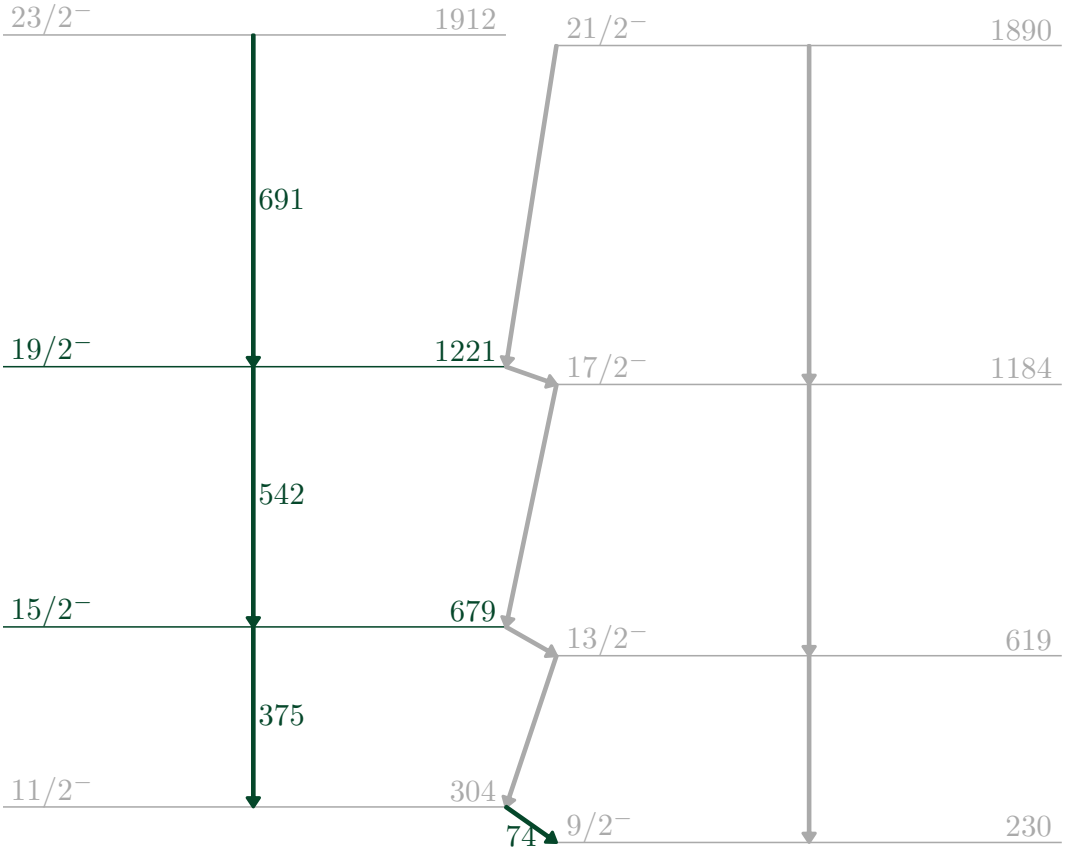

Figure 5.4: Partial level scheme around the studied levels in ^{109}Ru, coloured green. The level and transition energies are given in keV.

The fitting method described in section 2.1 was applied for each of the peaks. The peaks at 542 keV and at 691 keV were clean enough for the DDCM to be applied directly. For the peak at 375 keV, however, I^{b} was contaminated by the $9/2_2^+ \rightarrow 7/2_1^+$ decay at 368 keV.

Unable to determine Q directly in this case, we instead normalised the decay curve to the intensity I_{norm} of the $11/2_1^- \rightarrow 9/2_1^-$ transition at 74 keV. The $11/2_1^-$ state is long lived ($\tau = 1.0$ ns) and so only decays after the degrader, making a single component peak easily fitted cleanly. We then calculated Q as

$$Q = \frac{I^{\mathrm{b}}}{I_{\mathrm{norm}}} k, \tag{2.1}$$

where k is the ratio of the intensity of the normalisation peak to the total intensity of the studied peaks. This ratio is expected to be constant over the distances, and can thus be calculated for a single distance. In this case, we assumed that for the shortest distance, all decays occurred after the degrader:

$$k = \frac{I_{\text{norm}}}{I^{\text{b}} + I^{\text{a}}} = \frac{I_{\text{norm}}}{I^{\text{a}}(30\ \mu\text{m})} \tag{2.2}$$

For both the studied levels, the relative decay curves were fitted to fifth order Isplines, with knots at $x_{\text{d}} = \{0, 83, 235, 500, 1000, 2680\}$ µm. For the $19/2_1^-$ state, we obtained a better fit by adding an additional knot at 39 µm.

The results are displayed in figures 5.5 and 5.6. The velocity v_{b} was obtained from $\langle \beta^{-1} \rangle = 8.16$ reconstructed from VAMOS++, and the branching ratios were taken from Kumar, Chen, and Kondev (2016). The resulting lifetime values are

$$\tau(19/2_1^-) = 5.00 \pm 0.45 \text{ ps} \quad \text{and} \quad \tau(15/2_1^-) = 32.3 \pm 8.2 \text{ ps}.$$

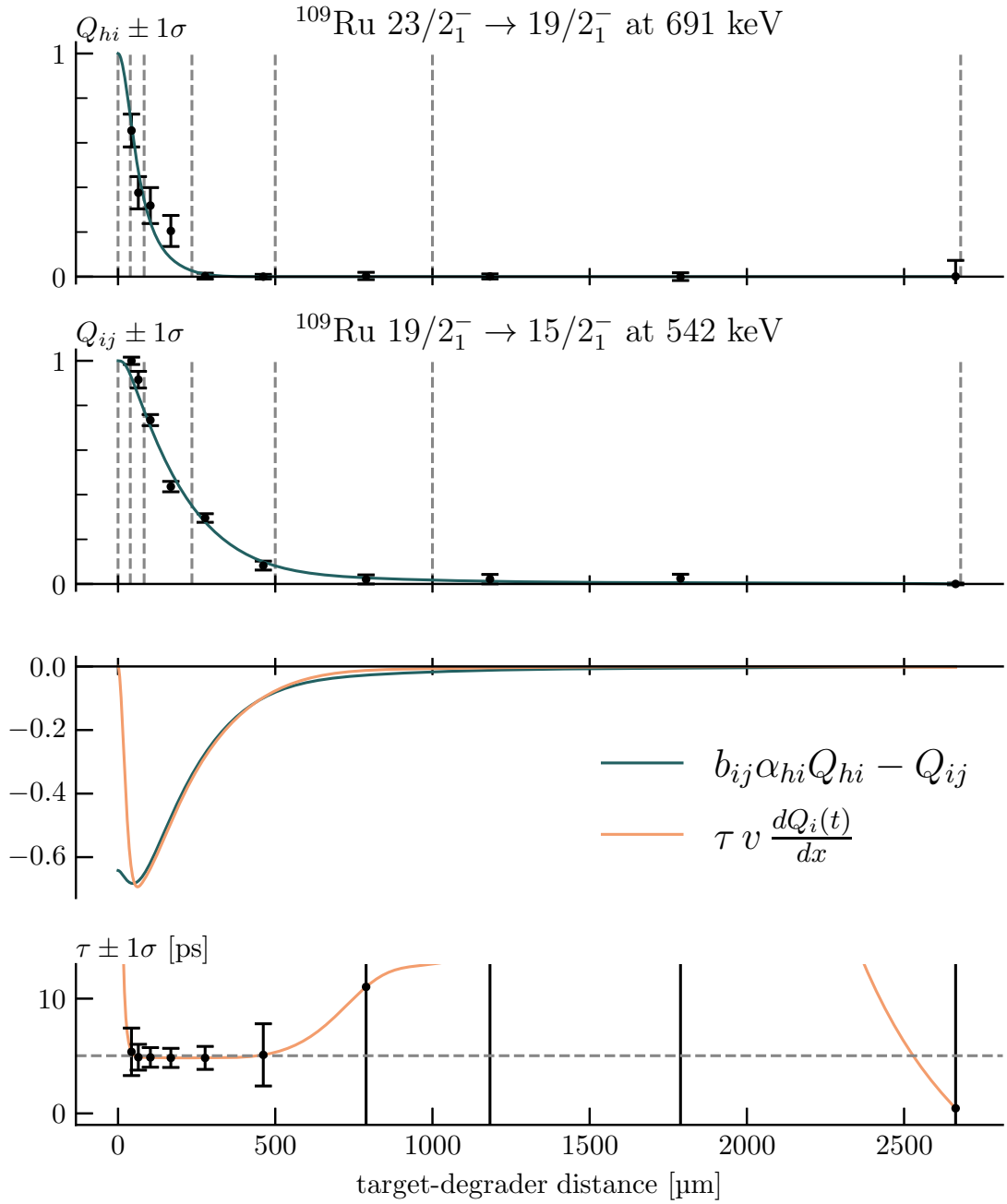

Figure 5.5: Fitted decay curves Q and lifetime τ of the $19/2_1^-$ state in ^{109}Ru. The fitted functions are fifth order Isplines, with knots marked by the vertical dashed lines. The horizontal dashed line in the bottom graph indicates the fitted lifetime value $\tau = 5.00 \pm 0.45$ ps.

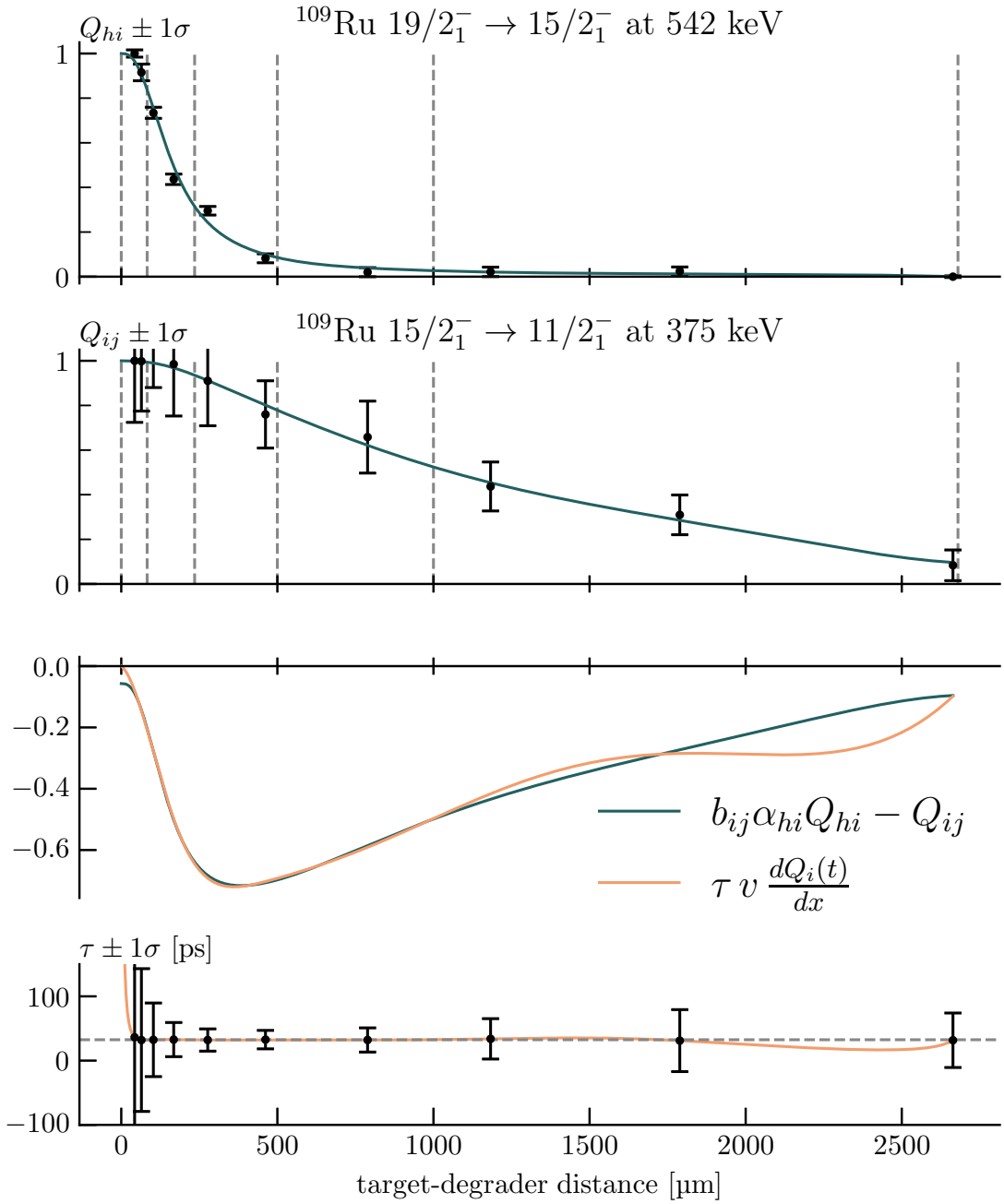

Figure 5.6: Fitted decay curves Q and lifetime τ of the $15/2_1^-$ state in ^{109}Ru. The fitted functions are fifth order Isplines with knots marked by the vertical dashed lines. The horizontal dashed line in the bottom graph indicated the fitted lifetime value $\tau = 32.3 \pm 8.2$ ps.

2.2 ^{111}Ru

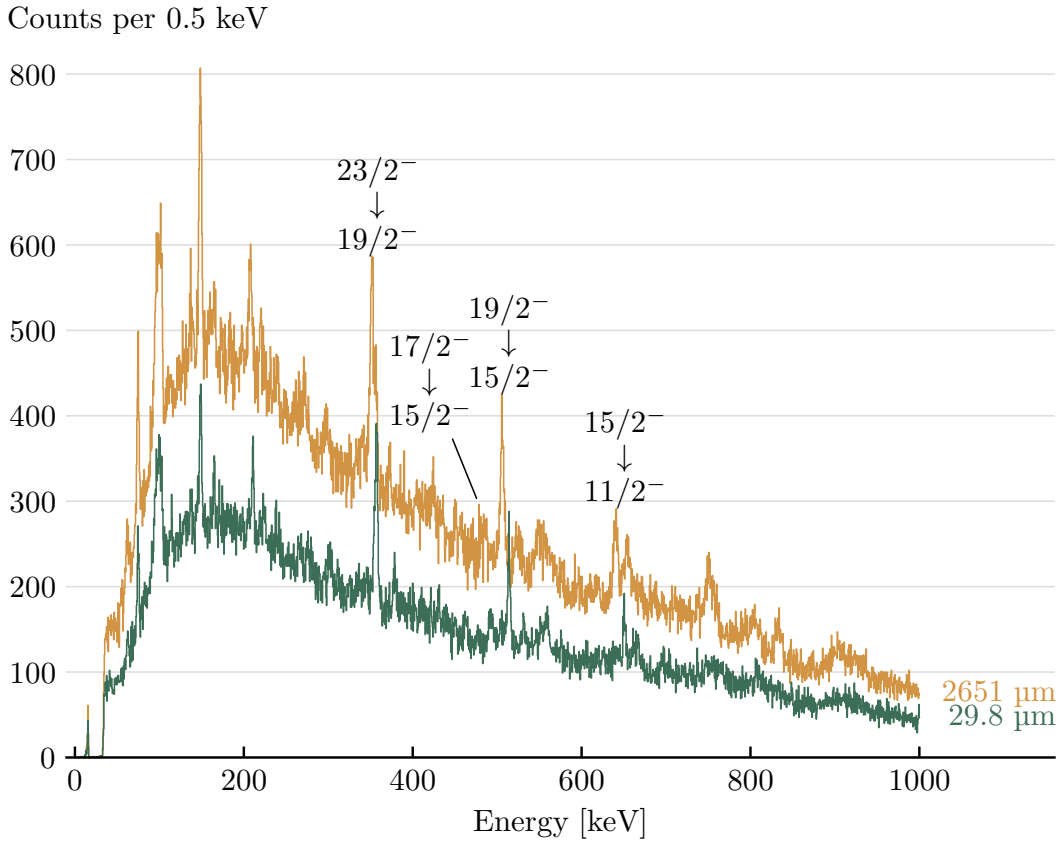

Figure 5.7: The γ-spectra for ^{111}Ru taken at the shortest and longest plunger distance.

Figure 5.7 shows the γ-spectra for ^{111}Ru, with the associated level scheme in figure 5.8. The $17/2^-_1 \rightarrow 15/2^-_1$ transition at 477 keV is present in the spectra, but too weak to fit. Its contribution to the lifetime of the $15/2^-_1$ state is assumed negligible. Feeding transitions from other bands (such as the $15/2^-_2 \rightarrow 15/2^-_1$ or $19/2^-_2 \rightarrow 19/2^-_1$transitions) were not observed in the γ-spectra.

The after degrader component of the $23/2^-_1 \rightarrow 19/2^-_1$ transition at 651 keV is superposed on the before degrader components of the $21/2^-_1 \rightarrow 17/2^-_1$ transition at 661 keV and the $19/2^+_1 \rightarrow 15/2^+_1$ transition at 666 keV. Due to the broadening of the peaks after the degrader, these two components had to be fitted as

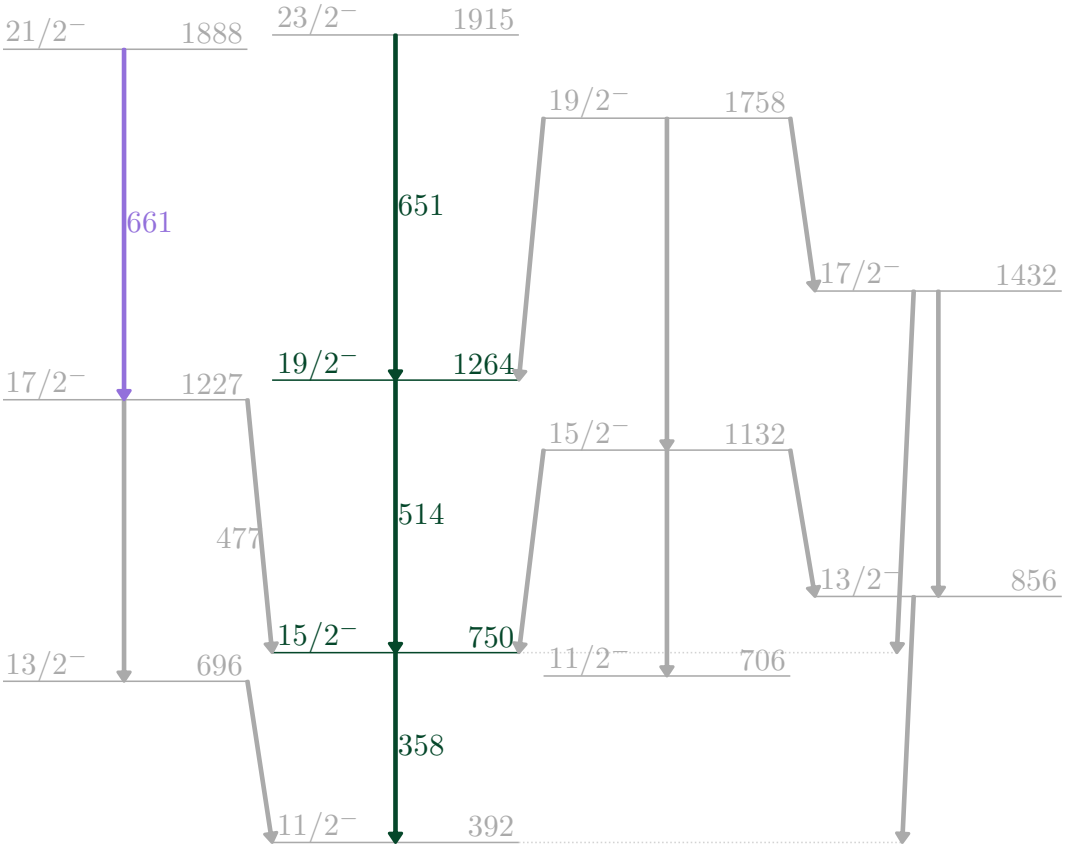

Figure 5.8: Partial level scheme around the studied transitions of ^{111}Ru, coloured green. The transitions referenced in the text are labeled, the contaminant transition is drawn in purple. The level and transition energies are given in keV.

a single peak. The before degrader components were still fitted individually. An example of this fit is shown in figure 5.9. Note that the spectra were fitted simultaneously with the same peak positions and widths.

Because of the aforementioned contamination, the uncertainty is significantly larger in I^{a} than in I^{b}. Therefore, the feeding coefficient α was calculated as the average of only the two longest distances, where it is safe to assume $I^{\mathrm{a}} = 0$.

No significant contaminants were observed for the $19/2^-_1 \rightarrow 15/2^-_1$ transition.

The decay curves were fitted using fifth order Isplines, with knots placed at $x_{\mathrm{d}} = \{0, 83, 235, 500, 1000, 2680\}$ µm.

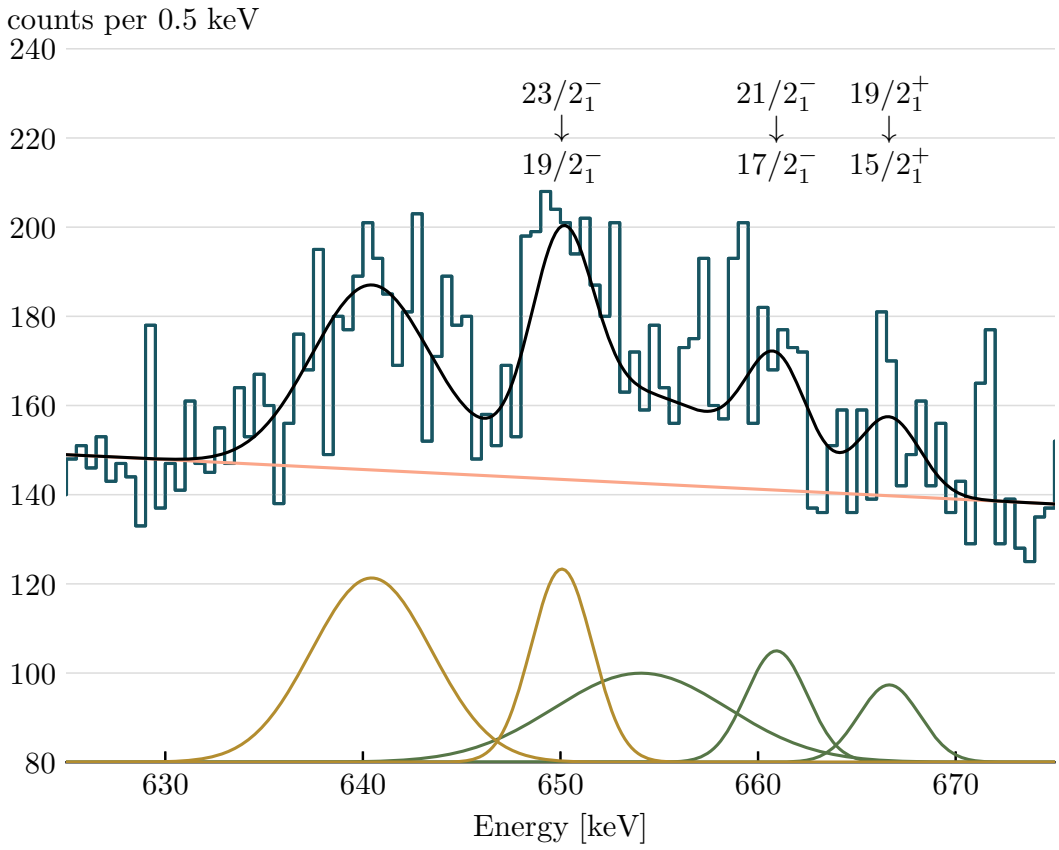

Figure 5.9: Fit of the $23/2_1^- \rightarrow 19/2_1^-$ transition along with the two contaminating transitions on a linear background for $x_d = 89.9$ µm. The labels correspond to the after degrader components. The before degrader components of the contaminating transitions are fitted as a single peak.

For the $15/2_1^- \rightarrow 11/2_1^-$ transition, the lifetime was long enough that the change in Q_{ij} took place primarily in the last four distances. We used the technique described in section 2.4, slicing the velocity distribution into two regions to give the decay curve 20 data points instead of the usual 10. The relative decay curves were fitted to fourth order Isplines whith knots at $t_\mathrm{d} = \{0, 4, 18, 40, 77\}$ ps.

The results are displayed in figures 5.10 and 5.11. The velocity v was obtained from $\langle\beta^{-1}\rangle = 8.27$ measured in VAMOS++, and the branching ratios were taken from Blachot (2009). We obtained the lifetimes

$$\tau(19/2_1^-) = 4.8 \pm 1.1 \text{ ps} \quad \text{and} \quad \tau(15/2_1^-) = 47.6 \pm 2.8 \text{ ps}.$$

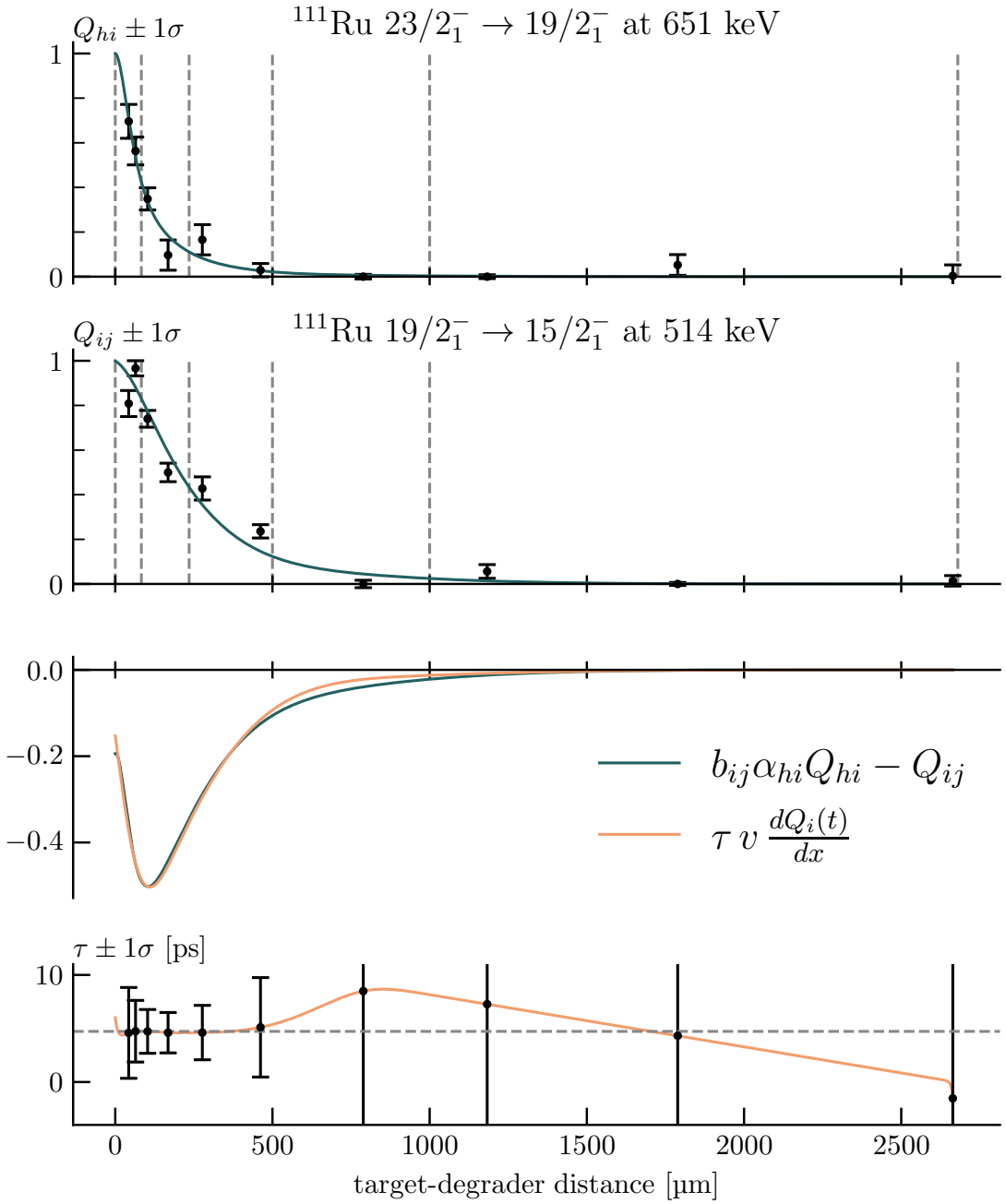

Figure 5.10: Fitted decay curves Q and lifetime τ of the $19/2_1^-$ state in ^{111}Ru. The fitted functions are fifth order Isplines with knots marked by the vertical dashed lines. The horizontal dashed line in the bottom graph indicates the fitted lifetime value $\tau = 4.8 \pm 1.1$ ps.

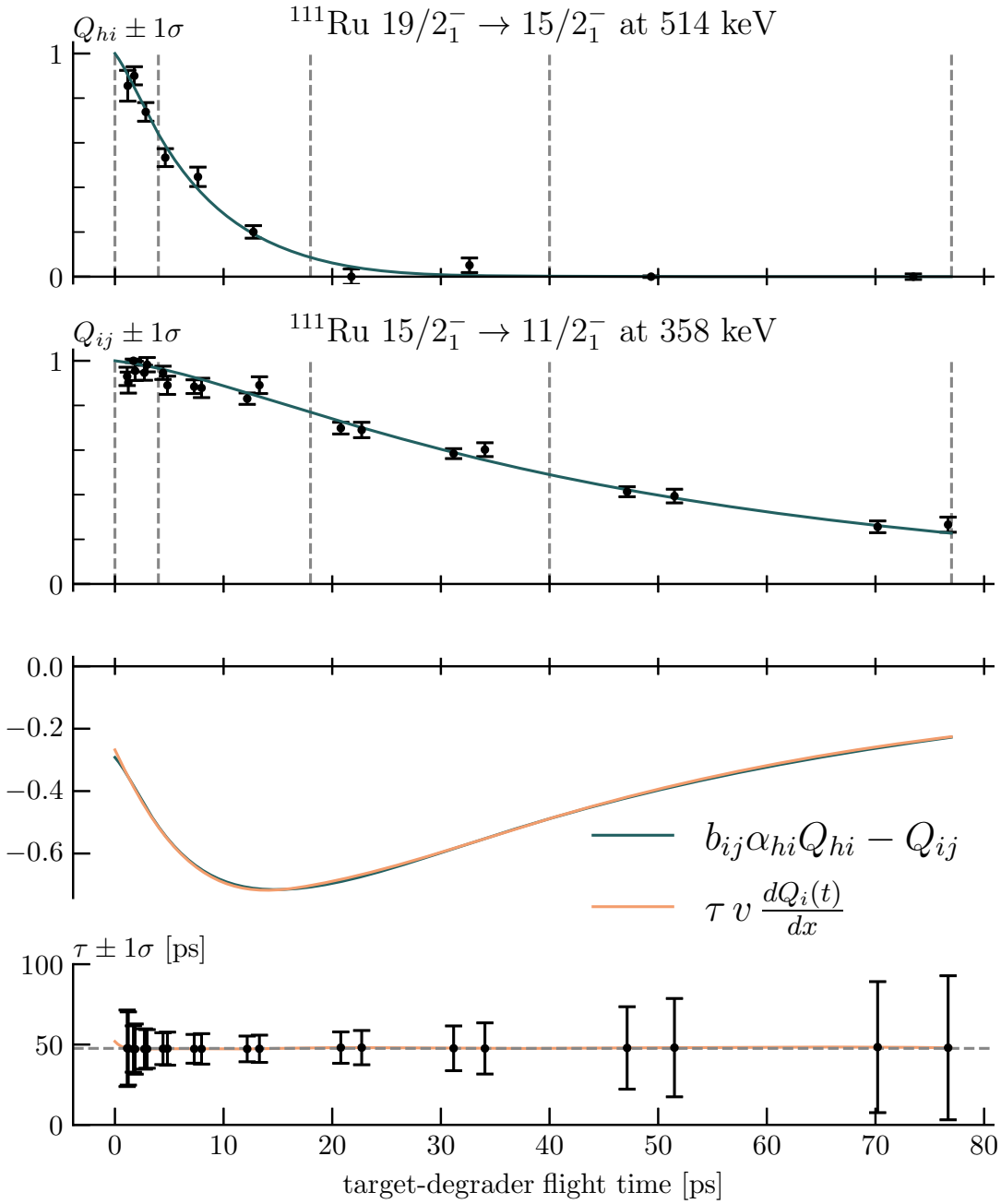

Figure 5.11: Fitted decay curves Q and lifetime τ of the $15/2_1^-$ state in ^{111}Ru, plotted against the target-degrader flight time. The fitted functions are fourth order Isplines with knots marked by the vertical dashed lines. The horizontal dashed line in the bottom graph indicates the fitted lifetime value $\tau = 47.6 \pm 2.8$ ps.

2.3 ^{110}Ru

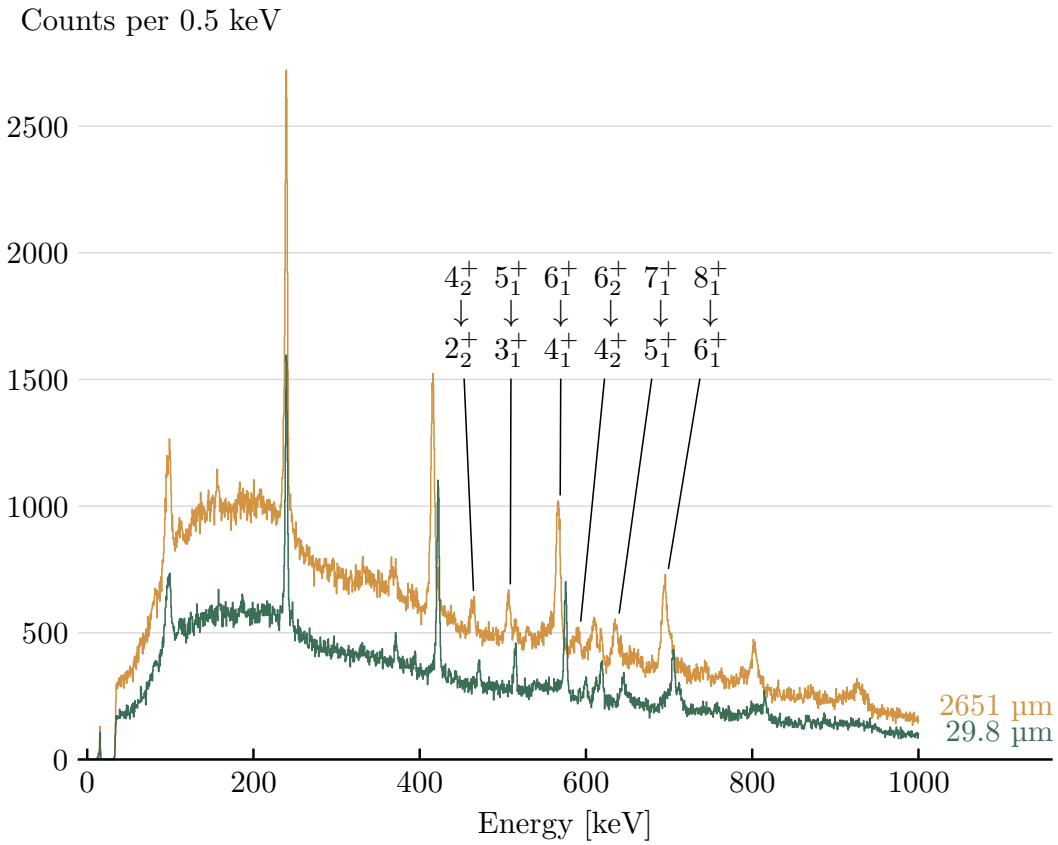

Figure 5.12: The γ-spectra for ^{110}Ru taken at the shortest and longest plunger distance.

The γ-spectra for this nucleus are displayed in figure 5.12. While they are dominated by transitions in the ground state band, transitions from the one phonon γ-band are distinguishable as well. These bands are shown in figure 5.13.

For the 6_1^+ level, only the transition from 8_1^+ feeder showed enough counts to be fitted. The transition from 6_2^+ may be present, but was not strong enough to include in the analysis. The other feeding transitions were not seen at all in the γ-spectra.

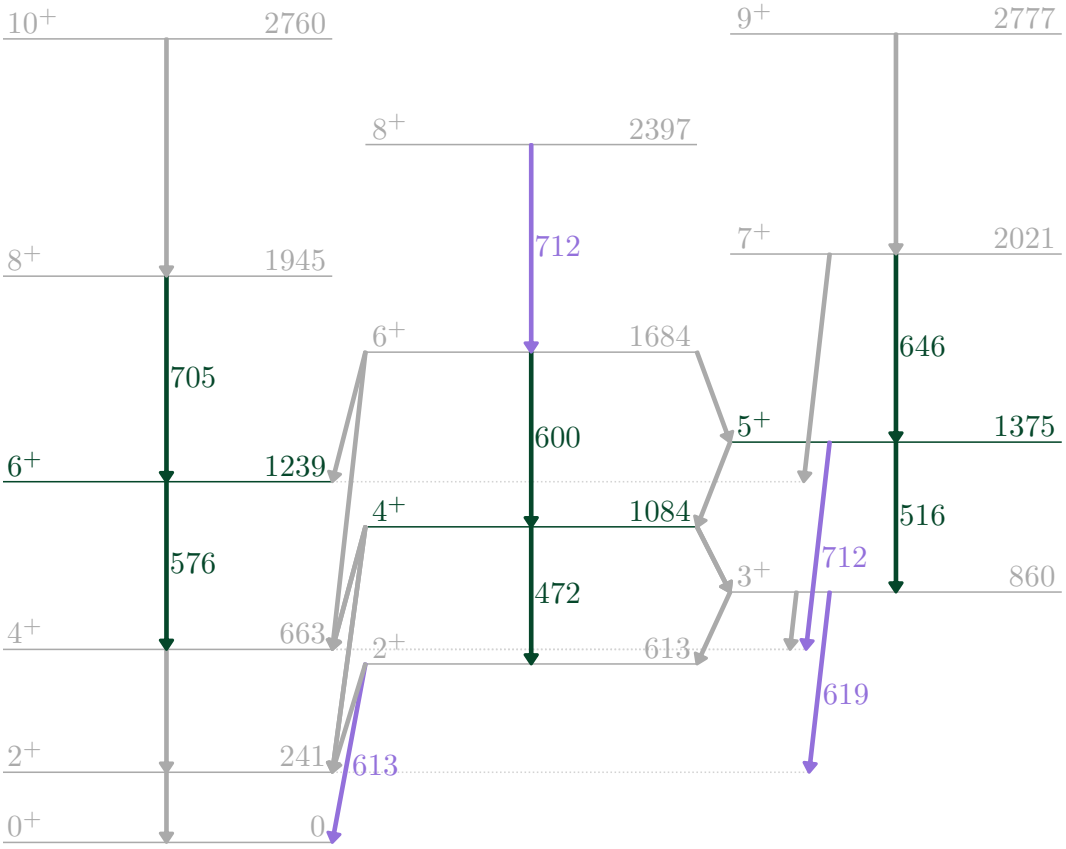

Figure 5.13: Partial decay scheme showing the ground-state band and one-phonon γ-band in ^{110}Ru. The studied transitions are drawn in green and contaminants in purple.

Several other transitions overlap with the $8_1^+ \rightarrow 6_1^+$ transition. The $12_2^- \rightarrow 10_2^-$ and $14_1^+ \rightarrow 12_1^+$ were both determined to be negligible. The $5_1^+ \rightarrow 4_1^+$ and $8_2^+ \rightarrow 6_2^+$ were indistinguishable from each other, but large enough to fit them as one peak, thus separating them from the transition of interest.

No significant contaminants were identified for the $6_1^+ \rightarrow 4_1^+$ transition.

The decay curves were fitted with fourth order Isplines, with knots placed at $x_\mathrm{d} = \{0, 83, 235, 500, 1500, 2680\}$ µm.

The $4_2^+ \rightarrow 2_2^+$ and $5_1^+ \rightarrow 3_2^+$ transitions peaks were both clean and were fitted without difficulty.

The feeding transition $6_2^+ \rightarrow 4_2^+$ was too close to the $3_1^+ \rightarrow 2_1^+$ and $2_2^+ \rightarrow 0_1^+$ transitions to be fitted alone. The peak itself was clean, but the fit also requires some background on both sides. Therefore, the three transitions were fitted together, but since only the first peak was used in the analysis, we did not strive for a high level of accuracy on the latter two.

Several transitions overlap with the $7_1^+ \rightarrow 5_1^+$ feeding transition. We have not been able to conclusively confirm their negligibility, nevertheless they all come from high energy states which we expect to be at most very weakly populated. We have therefore assumed they are negligible.

The decay curves were fitted using fifth order Isplines with knots placed at $x_\mathrm{d} = \{0, 235, 500, 1500, 2680\}$ µm.

The results are displayed in figures 5.14 to 5.16. The velocity v was obtained from $\langle \beta^{-1} \rangle = 8.21$ measured in VAMOS++, and the branching ratios were taken from Gürdal and Kondev (2012). Our analysis yielded the lifetimes

$$\tau(6_1^+) = 3.56 \pm 0.36 \text{ ps}, \quad \tau(5_1^+) = 14.0 \pm 2.6 \text{ ps} \quad \text{and} \quad \tau(4_2^+) = 27.5 \pm 2.1 \text{ ps}.$$

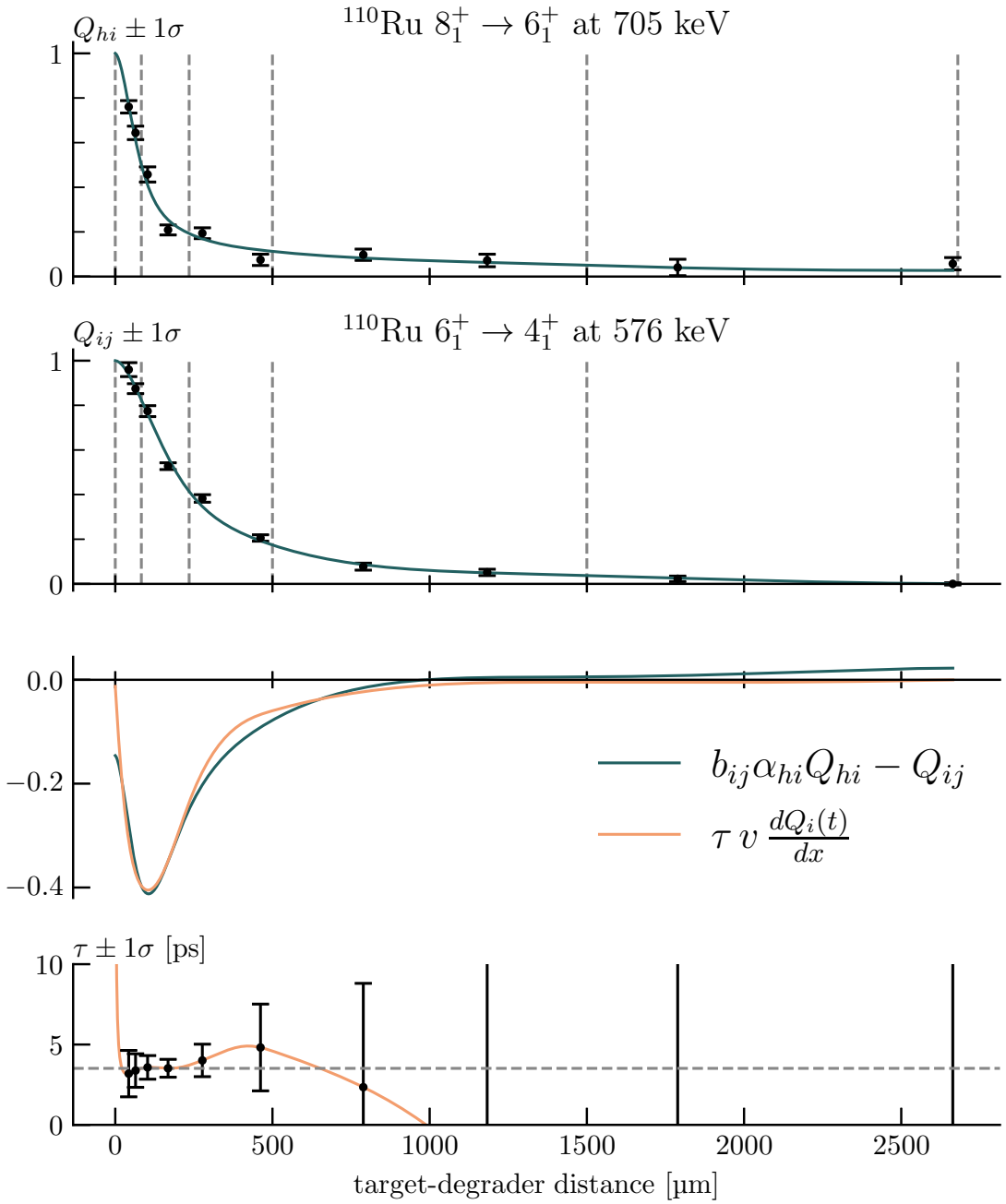

Figure 5.14: Fitted decay curves Q and lifetime τ of the 6_1^+ state in ^{110}Ru. The fitted functions are fourth order Isplines with knots marked by the vertical dashed lines. The horizontal dashed line in the bottom graph indicates the fitted lifetime value $\tau = 3.56 \pm 0.36$ ps.

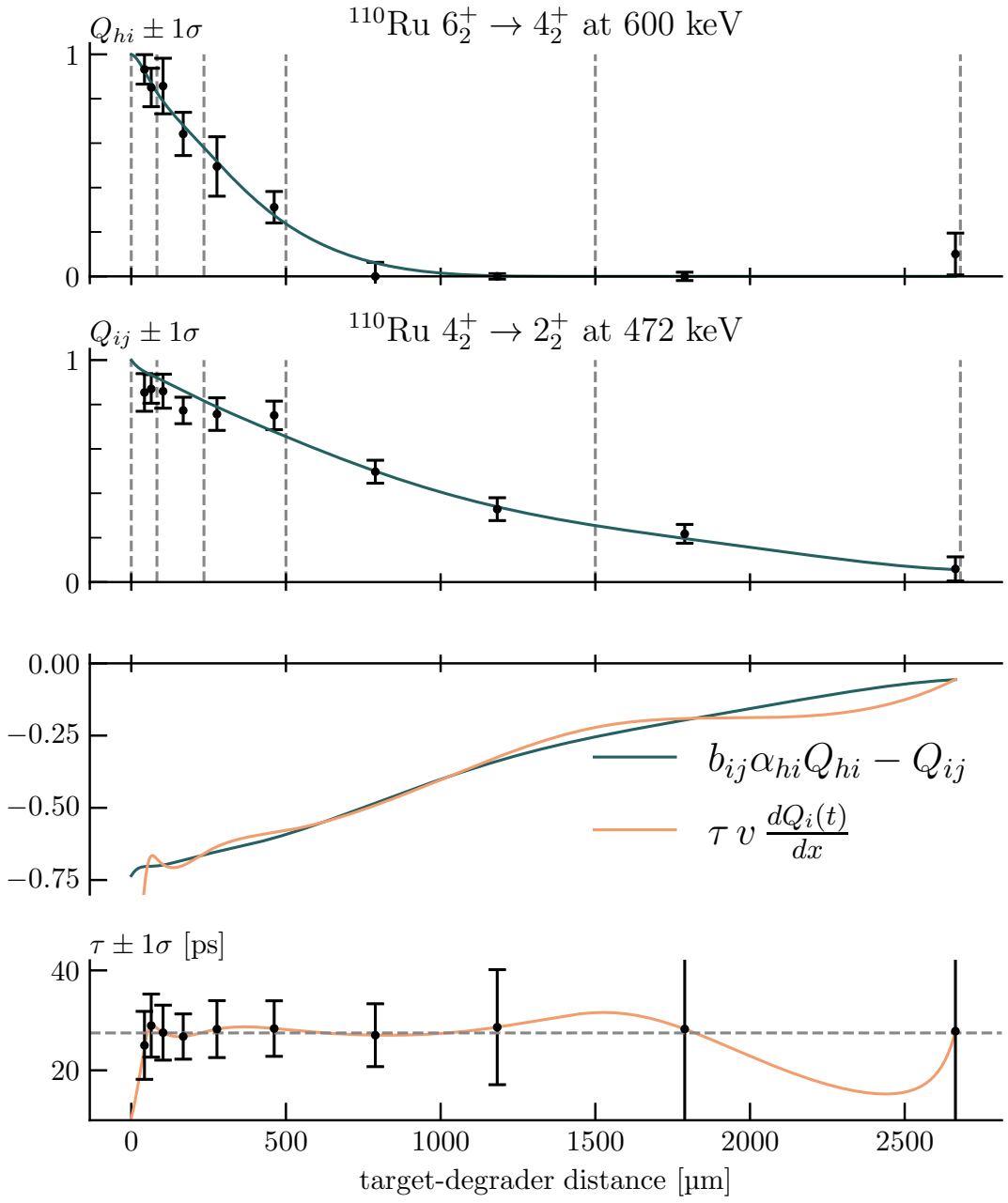

Figure 5.15: Fitted decay curves Q and lifetime τ of the 4_2^+ state in ^{110}Ru. The fitted functions are fifth order Isplines with knots marked by the vertical dashed lines. The horizontal dashed line in the bottom graph indicates the fitted lifetime value $\tau = 27.5 \pm 2.1$ ps.

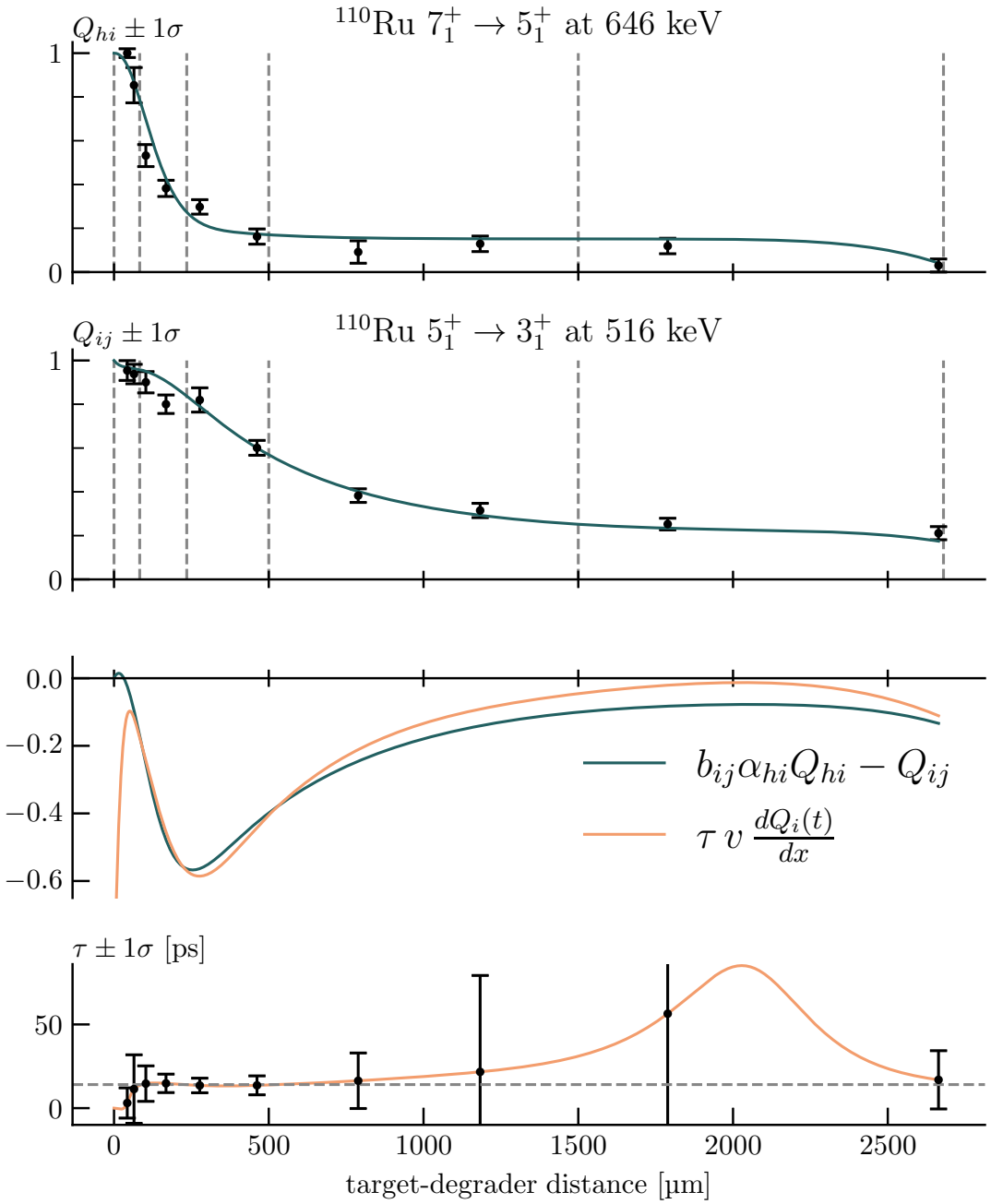

Figure 5.16: Fitted decay curves Q and lifetime τ of the 5_1^+ state in ^{110}Ru. The fitted functions are fifth order Isplines with knots marked by the vertical dashed lines. The horizontal dashed line in the bottom graph indicates the fitted lifetime value $\tau = 14.0 \pm 2.6$ ps.

Table 5.1: Measured lifetimes of excited states in ^{109,110,111}Ru, along with branching ratios from the literature and calculated $B(E2)$ values. The standard deviations are shown in brackets for each value.

Nucleus	**Transition**	$\boldsymbol{E_\gamma}$ keV	$\boldsymbol{\tau}$ ps	$\boldsymbol{b}$ %	$\boldsymbol{B(E2)}$ $10^2\ e^2\text{fm}^4$
^{109}Ru*	$19/2_1^- \rightarrow 15/2_1^-$	541.6	5.00 (45)	100	35.0 (32)
	$15/2_1^- \rightarrow 11/2_1^-$	374.7	32.3 (82)	100	34.2 (87)
^{111}Ru†	$19/2_1^- \rightarrow 15/2_1^-$	514.1	4.8 (11)	100	47. (11)
	$15/2_1^- \rightarrow 11/2_1^-$	357.8	47.6 (28)	100	29.3 (17)
^{110}Ru‡	$6_1^+ \rightarrow 4_1^+$	575.7	3.56 (36)	100	36.3 (37)
	$5_1^+ \rightarrow 3_1^+$	515.5	14.0 (26)	80.7	12.9 (24)
	$5_1^+ \rightarrow 4_2^+$	291.0		2.9	8.1 (15)
	$5_1^+ \rightarrow 4_1^+$	711.9		16.4	0.52 (10)
	$4_2^+ \rightarrow 2_2^+$	471.5	27.5 (21)	46.4	5.91 (45)
	$4_2^+ \rightarrow 3_1^+$	224.5		1.3	6.77 (52)
	$4_2^+ \rightarrow 4_1^+$	421.0		23.5	5.27 (40)
	$4_2^+ \rightarrow 2_1^+$	843.6		28.8	0.200 (15)

*Kumar, Chen, and Kondev (2016)
†Blachot (2009)
‡Gürdal and Kondev (2012)

Chapter 6

Discussion

1 Evaluation of the analysis methods

There are several sources of uncertainty in our analysis, some arising from the experimental measurements and some from our methods. We attempt here to give a full overview of the known sources of uncertainty, and how these affect the results presented in the previous chapter.

1.1 Uncertainties arising from the experiment

Errors in the VAMOS++ measurements used for particle identification will not affect the lifetime measurements. An event is assigned to a single fission fragment, and incorrectly identified events will only contribute to the noise in the γ-spectra. That is, of course, unless the contamination is significant and overlaps with a fitted peak. In such cases, as for ^{111}Ru, the contamination must be be identified and removed before fitting.

Two experimental uncertainties contribute to the lifetime. The statistical uncertainty in AGATA directly affects the fitted peak intensities I^{b} and I^{a}. The uncertainty in these fits are propagated through to the final lifetime. There is also an uncertainty in the reconstructed velocity v_{b} before the degrader, both from the VAMOS++ measurement and from the reconstruction. Statistical uncertainties have been studied by Hackstein and Dewald (2014), who found that effects from a wide velocity distribution are generally negligible at high veloci-

ties. Furthermore, our very good mass resolution testifies the high precision of the velocity measurement in VAMOS++. A detailed study of systematic errors related to the reconstruction of the velocity before the degrader has not yet been performed, though preliminary analysis based on the Doppler corrected energies indicates they are small.

1.2 Uncertainties arising from our analysis

In this work, each peak was fitted simultaneously for all distances, with a single mean and standard deviation. This has the distinct advantage of not placing constraints on any individual fit, only a global consistency requirement. A heavily constrained parameter can result in an artificial lowering of the final error estimates, which in turn causes incorrect weighting of the data points when fitting the decay curves.

This combined fitting does, however, suppose that the peak mean and width actually are equal in all spectra. This requires similar velocity distributions, and equivalent calibration of all γ-spectra. In practice, this method obtains more consistent fits of the peaks at the cost of a higher sensitivity to deviations in the spectra. In the present case, such inconsistencies were small and the combined fits were observed to achieve better results than early attempts at single peak fitting.

The spectra where one component is close to zero pose a particular challenge. When the fitting algorithm attempts to fit a peak at a given position, with a given width, it will find such a peak in the background noise, regardless of whether any real peak exists. In the DCM2, the relative decay curve was constrained to 0 at $x_\mathrm{d} = 0$, and thus accords less importance to these measurements.

Accurate determination of the lifetime of an energy level requires us to take into account all feeding into that level. This is a potential source of systematic error.

The studied states are fed through multiple transitions which appear very weakly or not above the background in the γ-spectra. While such transitions may not make, independently, significant contributions to the decay* , this may not be true of them combined. Such a systematic error would result in a slight overestimate of the lifetime. This is a possible explanation for the difference observed in

*Even a week feeder can contribute significantly if it is very long lived. This is not the case for the levels studied in this work.

figure 5.2 between the lifetimes measured in $\gamma\gamma$-coincidence and those measured in single-γ decay. Where possible, $\gamma\gamma$-coincidence analysis should be performed to quantify this systematic error. Single-γ analysis can then be used to obtain a lower statistical uncertainty.

The DCM2 developed for and used in this work differs significantly from the Napatau method of fitting decay curves. Where the latter aims to minimise the number of constraints, and thereby treat each data point as an independent lifetime measurement, the DCM2 aims to view the data as a single system by imposing constraints of physicality.

As we showed in section 5.1, the lifetime obtained by the DCM2 has a low sensitivity to the user-defined parameters, an important criteria for any method. It also avoids some unphysical features, namely the decay curve increasing, becoming negative, or not going to one at $t = 0$, making the fit more reliable.

We observed a discrepancy with the measurements by Smith et al. (2002) for ^{104}Ru. The results obtained with the DCM2 for this nucleus are consistent with results obtained by Pasqualato (2022) using Napatau on the same dataset, showing that it is not due to the DCM2. Our results for the 6_1^+ state in ^{110}Ru are also consistent with measurements by Krücken et al. (2001), using the RDDS method with a ^{252}Cf source, and by Doherty et al. (2017), using Coulomb excitation. This agreement gives additional confidence in our measurements, indicating that there is no general systematic discrepancy between the experimental methods. The specific case of the discrepancy with Smith et al. (2002), observed for all measurements based on VAMOS++ data with a fusion-fission reaction, is not yet understood.

2 Interpretation and comparison with previous work

2.1 Generalised Triaxial Rotor Model Calculations for ^{110}Ru

As outlined in section 2.2, theoretical calculations of the $B(E2)$ values for ^{110}Ru have been performed by Delaroche et al. (2010) and by Shi and Li (2018). Doherty et al. (2017) have performed Coulomb excitation measurements of the

transitions up to the 6_1^+ and 3_1^+ levels in ^{110}Ru, along with GTRM calculations based on those values. The GTRM calculations presented here are based on the combined set of our $B(E2)$ values and those measured by Doherty et al. (2017).

We fitted the parameters $Q_t, \gamma, \Gamma_2, \Gamma_4, \Gamma_6$ of the GTRM to the $B(E2)$ values in an iterative process. In each iteration, the quadrupole moment Q_t was fitted only to the $3^+ \rightarrow 2^+$ and $2^+ \rightarrow 0^+$ transitions, as these have the smallest dependence on the other parameters. The asymmetry angle γ and the mixing angles Γ_I were then fitted to all transitions keeping Q_t constant. The best fit was obtained after four iterations, and is shown in figure 6.1.

The mixing angles are expected from theory to follow the relation in equation (1.17). The values resulting from our fit are compared to the theoretical values in table 6.1. It should be noted that Γ_6 is only fitted from a single $B(E2)$ measurement, and as such has a very low accuracy. Indeed, we observed that with only small changes in the other parameters, Γ_6 could be made to take multiple widely different values. The good agreement between the individually fitted mixing angles and the values obtained from Γ_2 and equation (1.17) suggests that the GTRM describes the rotational bands in ^{110}Ru very well.

Table 6.1: The fitted and calculated mixing angles in the GTRM. The calculated values were obtained by inserting the fitted Γ_2 into equation 1.17.

	Γ_2 /°	Γ_4 /°	Γ_6 /°	Γ_8 /°
fitted GTRM	-15.6	-35.3	-41	
calculated from Γ_2	-15.6	-33.4	-39.4	-41.7

The $B(E2)$ values resulting from the fit are are displayed in figure 6.1 along with calculations by Delaroche (2010) and by Shi and Li (2018), as well as experimental values from this work, Doherty et al. (2017), and Snyder et al. (2013). The values are given in table C.1.

Up to the $7_1^+ \rightarrow 5_1^+$ transition, there is good agreement between the experimental values and the fitted GTRM. This indicates that, at low spins, ^{110}Ru is a well-deformed triaxial nucleus.

There is an exception, however, for the $5_1^+ \rightarrow 4_2^+$ transition, where the model prediction is close to thrice the experimental value. The experimental value is derived from the same lifetime measurement as the $5_1^+ \rightarrow 3_1^+$ and $5_1^+ \rightarrow 4_1^+$ transitions, which the GTRM predicts well. Hence it appears more likely that this discrepancy originates from an error in the adopted branching ratio, than from the GRTM calculations.

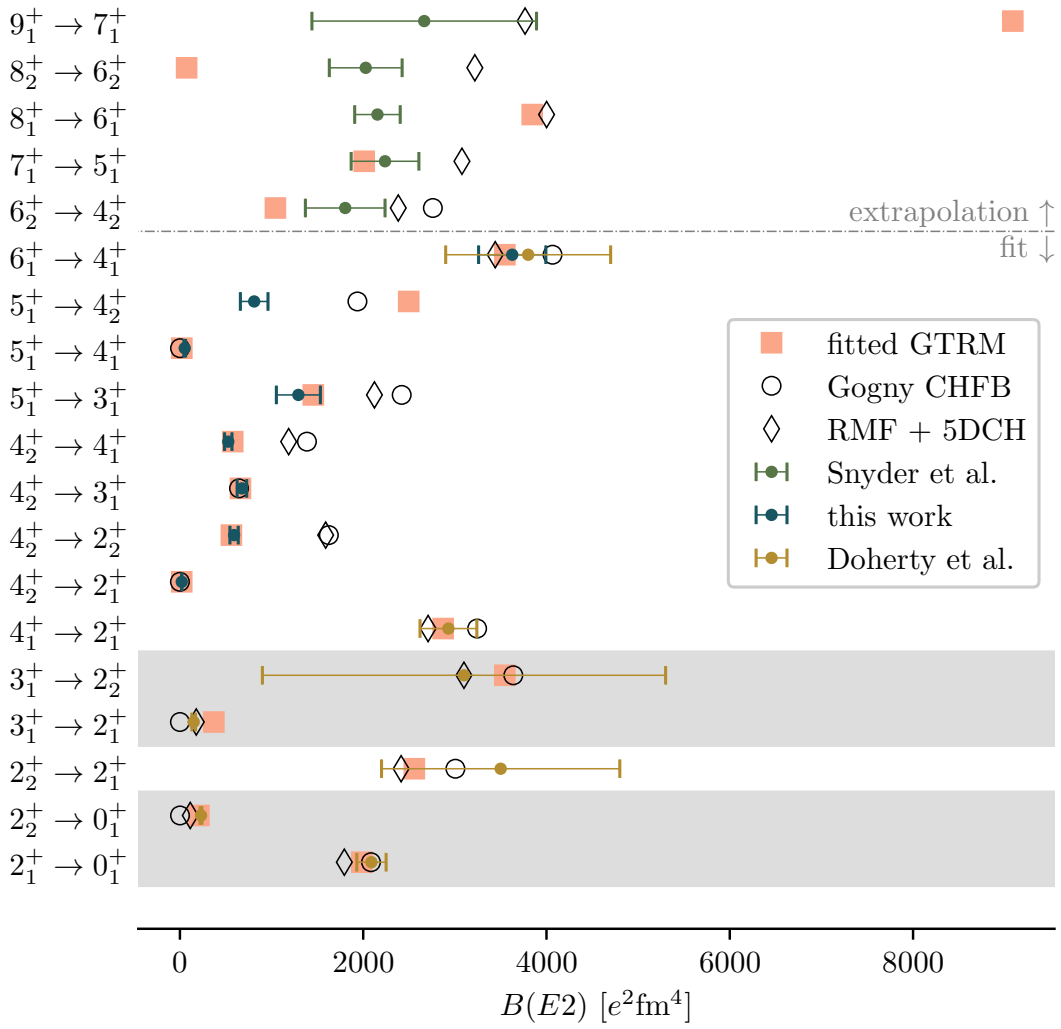

Figure 6.1: GTRM calculations fitted to $B(E2)$ values from this work and from Doherty et al. (2017), extrapolated to compare with the values obtained by Snyder et al. (2013). The gray bands mark the transitions used to fit Q_t. Predictions by CHFB + 5DCH Gogny D1S calculations by Delaroche (2010) and RMF + 5DCH calculations by Shi and Li (2018) are also shown.

The two microscopic models models displayed in figure 6.1 both follow the general trend of the experimental data. Contrarily to the GTRM, the predictions of these are not fitted to the particular data, modelling instead the entirety of the nucleic chart. As such they are typically less accurate for individual nuclei. The level of agreement observed in this case is as good as can be expected.

The deviation from experimental observations at high spin is an indication of other effects than simple triaxial rotation. At such high angular momenta we expect to see cranking effects, so this is not surprising. Indeed, the RMF + 5DCH calculations – which take cranking into account – remain close to the experimental values. Sugawara (2019) found that the asymmetry of ^{110}Ru deviated from a stable value at spins above 7_1^+. Changes in the deformation parameters would explain the breakdown of the GTRM used in this work. Changes in the transitional quadrupole moment at angular momentum $I \geq 8$ was also found in the triaxial projected shell model calculations by Zhang et al. (2015).

We obtain a quadrupole moment of $Q_t = 332 \pm 6\ e\,\mathrm{fm}^2$ and an asymmetry angle $\gamma = 33.5 \pm 0.7°$, slightly on the side of oblate deformation. From equation (1.16), we calculate a deformation magnitude $\beta = 0.30$, which is on the high end of the range of previously calculated values.

Our result is closest to the $(\beta, \gamma) = (0.31, 29°)$ obtained by Doherty et al. (2017), also using the GTRM. Their calculations already capture the main features of the nucleus. The additional $B(E2)$ values measured in this work strengthen the interpretation within the GTRM, and thus yield more reliable deformation parameters.

This contrasts with predictions of both microscopic-macroscopic and CHFB Gogny D1S calculations, which predict $\gamma < 30°$: slightly on the prolate side. The RMF + 5DCH calculations by Shi and Li (2018) are the only ones to predict $\gamma > 30°$, albeit with a slightly smaller deformation $\beta = 0.26$ than what we obtain.

Our γ value differs significantly from that found by Sugawara (2019), which predicts the lowest γ at approximately 20°.

In figure 6.2 we show contour plots of the calculated potential energy surfaces by the Gogny CHFB, RMF + 5DCH, and microscopic-macroscopic models, along with the (β, γ) values obtained in this work and by Doherty et al. (2017), and the minimum of the Skyrme CHFB calculations. It is clear that the latter deviates significantly from the other models, and our result reinforces this.

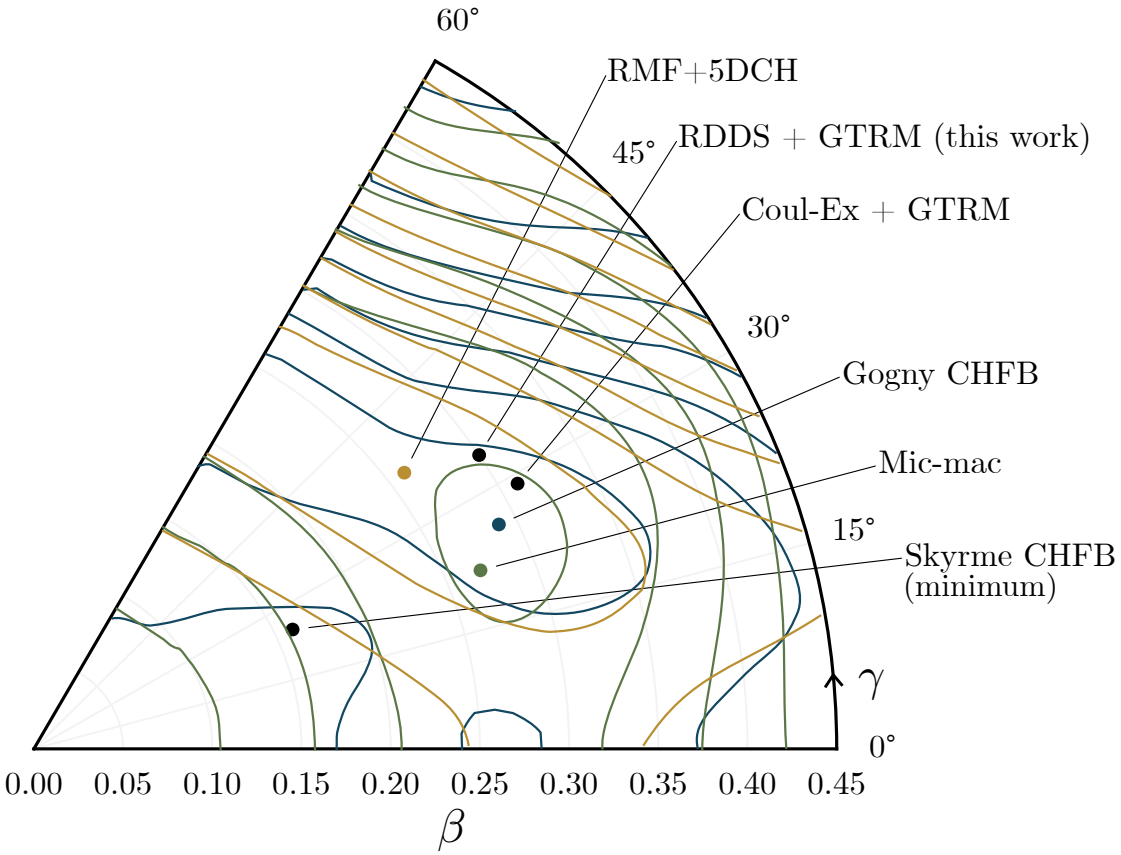

Figure 6.2: Deformation plot showing calculated and measured deformation parameters (β, γ) for ^{110}Ru. For the microscopic-macroscopic, Gogny CHFB and RMF + 5DCH calculations, contour lines of the potential energy surface are also drawn, with a separation of 1 MeV.

2.2 Odd-neutron Ruthenium isotopes.

An adequate interpretation of the $B(E2)$ values measured for ^{109,111}Ru requires triaxial particle rotor calculations. Such calculations are beyond the scope of this thesis, but will be performed in future work. Nevertheless, as a first approximation, we can compare the two nuclei by calculating their transitional quadrupole moments according to the formula

$$B(E2; I_i \to I_j) = \frac{5}{16\pi}(Q_t)^2 \langle I_i K 20 | I_j K \rangle^2 . \tag{2.1}$$

Since K is not a well-defined quantum number in triaxial nuclei, we use the strongest contributor, namely 5/2 for ^{109}Ru and 7/2 for ^{111}Ru. The value we obtain in this way has little physical significance, but can help identify possible changes in the deformation between ^{109}Ru and ^{111}Ru.

The $B(E2)$ values we have measured and the corresponding quadrupole moments from equation 2.1 are given in table 6.2.

Table 6.2: Measured $B(E2)$ values and calculated quadrupole moments for ^{109,111}Ru, assuming no higher order multipole deformations and ignoring triaxial mixing. Due to these approximation, the error in Q_t is larger than the quoted statistical uncertainties.

Nucleus	**transition**	E_γ keV	$B(E2)$ $10^2\ e^2\mathrm{fm}^4$	Q_t $10^2\ e\,\mathrm{fm}^2$
^{109}Ru	$19/2_1^- \to 15/2_1^-$	542	35.0 ± 3.2	351 ± 16
	$15/2_1^- \to 11/2_1^-$	375	34.2 ± 8.7	373 ± 47
^{111}Ru	$19/2_1^- \to 15/2_1^-$	514	47 ± 11	444 ± 51
	$15/2_1^- \to 11/2_1^-$	358	29.3 ± 1.7	403 ± 12

From the proximity of the calculated transitional quadrupole moments, there is little indication that the two additional neutrons contribute significantly to the deformation. Furthermore, compared to the quadrupole moment of $332 \pm 6\ e\mathrm{fm}^2$ obtained for ^{110}Ru, we cannot conclude on any effect of the odd neutron on the deformation in either case.

Chapter 7

Conclusions and outlook

In this thesis, we have presented several hitherto unmeasured lifetimes of excited states in ^{109,110,111}Ru. We have used them to obtain a total of twelve $B(E2)$ values – two for each odd isotope and eight for ^{110}Ru.

In the latter case, our measurements bridge the gap between previous low angular momentum Coulomb excitation measurements by Doherty et al. (2017) and high angular momentum Doppler shift attenuation measurements by Snyder et al. (2013). We combined our measurements with the former to fit the generalised triaxial rotor model. The model describes the nucleus well up to the 7_1^+ state, allowing us to extract reliable deformation parameters ($\beta = 0.30 \pm 0.01, \gamma = 33.5 \pm 0.7$) under the triaxial rotor assumption. These describe a well deformed, slightly oblate triaxial nucleus.

Microscopic nuclear structure models predict the $B(E2)$ values directly, making these a key way of testing models against experimental data. We compared the experimental $B(E2)$ values in ^{110}Ru with predictions from CHFB+5DCH Gogny D1S calculations by Delaroche et al. (2010) and RMF+5DCH calculations by Shi and Li (2018). Both models successfully predict the general trends observed in the experimental results.

The potential energy surfaces extracted from the above microscopic models are similar, and their minima differ only slightly from the deformation parameters of the fitted GTRM. They both predict a wide minimum on the oblate side, indicative of γ-softness. The precise location of the minimum is on the oblate side for the RMF+5DCH model, and slightly prolate for the Gogny CHBF model.

Contrariwise, cranked Skyrme HFB calculations by Zhang et al. (2015) predict a much lower deformation of the nucleus of approximately half the value of the GTRM fit.

Microscopic-macroscopic calculations by Möller et al. (2008) predict a well deformed nucleus, as opposed to the microscopic models which predict γ-softness. The calculated potential energy minimum is less deformed and more prolate than the deformation of the fitted GTRM.

For ^{109}Ru and ^{111}Ru, we used a simple first approximation of the transitional quadrupole moment Q_t to identify possible changes in the deformation between these two isotopes. No conclusive evidence of change was observed, either between the odd isotopes or with ^{110}Ru. These nuclei will be studied further using triaxial particle rotor calculations, which will produce more accurate results.

The evolution of the deformation in the Ruthenium chain can be studied by performing similar analyses on ^{112}Ru, and possibly ^{108}Ru. Applying the same analysis methods on data from the same experiment will drastically reduce the effect of systematic uncertainties when comparing the different isotopes.

As part of the work, we have written a program to fit the same peaks in multiple γ-spectra simultaneously, producing consistent fits while avoiding the errors that come from manually constraining fit parameters. This program is available at `https://github.com/johashei/multifit` and as a python package. It will be expanded in terms of both documentation and functionality, making it more easily applicable to other cases.

We have also developed a novel method of fitting the decay curves obtained in recoil distance Doppler shift experiments. This method, called the *derivative constrained monotonic decay curve method* (DCM2) was first tested and applied in this thesis. By imposing constraints of physicality on the fitted curves, taking all data points into account when determining the lifetime, and being only weakly dependant on user-defined parameters, it is expected to provide more reliable results than currently used methods. Future work (Modamio, Heines, and Görgen unpublished) will provide a detailed characterisation of the method, particularly with regards to uncertainty determination and expansion to multiple feeders. In this context, the code will be published and developed into a python package.

Some deviation of the lifetimes measured with the RDDS method using the ^{238}U(^{9}Be, f) reaction from the adopted values has been observed both in this work, and by Grente (2014), Ansari (2019) and Pasqualato (2022). Most of these

are likely to be caused by weak long-lived feeders which are unaccounted for in the single-γ analyses. These systematic errors will be removed by $\gamma\gamma$-coincidence analysis in future work. Nevertheless, some cases, notably in ^{100}Zr and ^{104}Mo, produce consistent shorter lifetimes in both approaches. It is therefore of interest to conduct a study of the implementations and assumptions of both the fusion-fission RDDS technique and the ^{252}Cf-decay differential plunger technique with which the adopted values were measured (Smith et al. 2002).

The experimental setup has achieved much better RDDS results than have previously been available. The fission fragment identification in VAMOS++ has made clean γ-spectra for a large number of nuclei. The replacement of EXOGAM by AGATA has increased the statistics by an order of magnitude, pushing the limits of nuclei available for single-γ and $\gamma\gamma$-coincidence analysis. In particular it allows for the analysis of odd-neutron nuclei to a much larger extent.

Only a small fraction of the dataset has yet been analysed.

Bibliography

Akkoyun, S. et al. (2012). "AGATA-Advanced GAmma Tracking Array". In: *Nuclear Instruments & Methods in Physics Research Section a-Accelerators Spectrometers Detectors and Associated Equipment* 668, pages 26–58. DOI: 10.1016/j.nima.2011.11.081.
(Cited on page 19.)

Allmond, James Mitchell (2007). "Studies of Triaxial Rotors and Band Mixing in Nuclei". Thesis. Georgia Institute of Technology.
(Cited on pages 14, 15.)

Ansari, Saba (2019). "Shape evolution in neutron-rich Zr, Mo and Ru isotopes around mass A=100". Thesis. Université Paris-Saclay.
(Cited on pages 32, 68.)

Azaiez, F. (1999). "EXOGAM: a γ-ray spectrometer for radioactive beams". In: *Nuclear Physics A* 654.1, Supplement 1, pages 1003c–1008c. DOI: 10.1016/S0375-9474(00)88588-7.
(Cited on page 21.)

Blachot, Jean (2009). "Nuclear Data Sheets for A = 111". In: *Nuclear Data Sheets* 110.6, pages 1239–1407. DOI: 10.1016/j.nds.2009.04.002.
(Cited on pages 49, 58.)

Bloom, Jesse and Kate H. D. Crawford (Mar. 4, 2022). *dms_variants. islpine.* Bloom Laboratory. URL: https://jbloomlab.github.io/dms_variants/dms_variants.ispline.html#module-dms_variants.ispline.
(Cited on page 35.)

Bohr, Aage and Ben R. Mottelson (1969-1975). *Nuclear structure.* Edited by Benjamin. 2 volumes. New York.

(Cited on page 10.)

Clément, E. et al. (2017). "Conceptual design of the AGATA 1π array at GANIL". In: *Nuclear Instruments and Methods in Physics Research Section A: Accelerators, Spectrometers, Detectors and Associated Equipment* 855, pages 1–12. DOI: 10.1016/j.nima.2017.02.063.
(Cited on page 20.)

Crameri, Fabio (Sept. 2021). *Scientific colour maps*. Version 7.0.1. DOI: 10.5281/zenodo.5501399.
(Cited on page ii.)

Crameri, Fabio, Grace E. Shephard, and Philip J. Heron (2020). "The misuse of colour in science communication". In: *Nature Communications* 11.1, page 5444. DOI: 10.1038/s41467-020-19160-7.
(Cited on page ii.)

Davydov, A. S. and G. F. Filippov (1958). "Rotational states in even atomic nuclei". In: *Nuclear Physics* 8, pages 237–249. DOI: 10.1016/0029-5582(58)90153-6.
(Cited on page 14.)

Delaroche, J. P. et al. (2010). "Structure of even-even nuclei using a mapped collective Hamiltonian and the D1S Gogny interaction". In: *Physical Review C* 81.1. DOI: 10.1103/PhysRevC.81.014303.
(Cited on pages 16, 61, 67.)

Delaroche, Jean-Paul (2010). *HFB+GCM(GOA) calculations with Gogny D1S interaction*. private communication. Bruyères-le-Châtel: CEA/DAM/DIF.
(Cited on pages 62, 63, 91.)

Dembinski, Hans and Piti Ongmongkolkul et al. (Dec. 2020). "scikit-hep/iminuit". In: DOI: 10.5281/zenodo.3949207.
(Cited on page 31.)

Dewald, A., S. Harissopulos, and P. von Brentano (1989). "The differential plunger and the differential decay curve method for the analysis of recoil distance Doppler-shift data". In: *Zeitschrift für Physik A Atomic Nuclei* 334.2, pages 163–175. DOI: 10.1007/BF01294217.
(Cited on pages 29, 31, 38.)

Dewald, A., O. Möller, and P. Petkov (2012). "Developing the Recoil Distance Doppler-Shift technique towards a versatile tool for lifetime measurements of excited nuclear states". In: *Progress in Particle and Nuclear Physics* 67.3, pages 786–839. DOI: 10.1016/j.ppnp.2012.03.003.
(Cited on page 29.)

Ding Huai-Bo et al. (2009). "Extended collective bands in neutron-rich ^{109}Ru". In: *Chinese Physics C* 33.S1, pages 154–157. DOI: 10.1088/1674-1137/33/s1/049.
(Cited on page 42.)

djmw (Nov. 1, 2012). *Praat manual. spline.* URL: https://www.fon.hum.uva.nl/praat/manual/spline.html.
(Cited on page 35.)

Doherty, D. T. et al. (2017). "Triaxiality near the 110Ru ground state from Coulomb excitation". In: *Physics Letters B* 766, pages 334–338. DOI: 10.1016/j.physletb.2017.01.031.
(Cited on pages 16, 17, 61–64, 67, 91.)

Droste, Ch et al. (2004). "Description of 111Ru within the Core-Quasiparticle Coupling model". In: *The European Physical Journal A - Hadrons and Nuclei* 22.2, pages 179–188. DOI: 10.1140/epja/i2004-10041-9.
(Cited on page 15.)

Girod, Michel (2007). private communication. Bruyères-le-Châtel: CEA/DAM/DIF.
(Cited on page 2.)

Grente, Lucie (2014). "Structure des fragments de fission de masse A = 100 - 110 : mesures de temps de vie et analyses en champ moyen et au-delà". Thesis. Université Paris-Sud.
(Cited on pages 21, 23, 68.)

Gürdal, G. and F. G. Kondev (2012). "Nuclear Data Sheets for A = 110". In: *Nuclear Data Sheets* 113.5, pages 1315–1561. DOI: 10.1016/j.nds.2012.05.002.
(Cited on pages 54, 58.)

Hackstein, M. and A. Dewald (2014). "Velocity distribution in Recoil-Distance Doppler-Shift experiments". In: *Nuclear Instruments & Methods in Physics Research Section a-Accelerators Spectrometers Detectors and Associated Equipment* 738, pages 93–98. DOI: 10.1016/j.nima.2013.11.047.
(Cited on pages 35, 59.)

Hilaire, S. and M. Girod (2007). "The AMEDEE nuclear structure database". In: *International Conference on Nuclear Data for Science and Technology* (ND 2007). DOI: 10.1051/ndata:07709.
(Cited on page 2.)

James, F. and M. Roos (1975). "Minuit: A System for Function Minimization and Analysis of the Parameter Errors and Correlations". In: *Comput. Phys. Commun.* 10, pages 343–367. DOI: 10.1016/0010-4655(75)90039-9.
(Cited on page 32.)

Krücken, R. et al. (2001). "Lifetimes in neutron-rich fission fragments using the differential recoil distance method". In: *Physical Review C* 64.1. DOI: 10.1103/PhysRevC.64.017305.
(Cited on page 61.)

Kumar, S., J. Chen, and F. G. Kondev (2016). "Nuclear Data Sheets for A = 109". In: *Nuclear Data Sheets* 137, pages 1–286. DOI: 10.1016/j.nds.2016.09.001.
(Cited on pages 15, 44, 58.)

Ljungvall, J. et al. (2012). "The Orsay Universal Plunger System". In: *Nuclear Instruments and Methods in Physics Research Section A: Accelerators, Spectrometers, Detectors and Associated Equipment* 679, pages 61–66. DOI: 10.1016/j.nima.2012.03.041.
(Cited on pages 18, 20.)

Modamio, Victor, Johannes S. Heines, and Andreas Görgen (unpublished). "The Derivative Constrained Monotonic Decay Curve Method". in preparation.
(Cited on pages 34, 68.)

Möller, P. et al. (2008). "Axial and reflection asymmetry of the nuclear ground state". In: *Atomic Data and Nuclear Data Tables* 94.5, pages 758–780. ISSN: 0092-640X. DOI: 10.1016/j.adt.2008.05.002.
(Cited on pages 16, 68.)

Nilsson, S. G. (1955). "Binding states of individual nucleons in strongly deformed nuclei". In: *Kong. Dan. Vid. Sel. Mat. Fys. Med.* 29N16, pages 1–69.
(Cited on page 7.)

Nilsson, Sven Gösta and Ingemar Ragnarsson (1995). *Shapes and Shells in Nuclear Structure*. Cambridge: Cambridge University Press. DOI: 10.1017/CBO9780511563973.
(Cited on page 4.)

Pasqualato, Giorgia (May 6, 2022). *Mo-104. results may 2022*. Personal communication. IJCLab, CNRS/IN2P3, Université Paris-Saclay.
(Cited on pages 40, 41, 61, 68.)

Pasqualato, Giorgia et al. (unpublished). in preparation.
(Cited on page 38.)

Ramsay, J. O. (1988). "Monotone Regression Splines in Action". In: *Statistical Science* 3.4, pages 425–441. URL: http://www.jstor.org/stable/2245395.
(Cited on page 35.)

Rejmund, M. et al. (2011). "Performance of the improved larger acceptance spectrometer: VAMOS++". In: *Nuclear Instruments and Methods in Physics Research Section A: Accelerators, Spectrometers, Detectors and Associated Equipment* 646.1, pages 184–191. DOI: 10.1016/j.nima.2011.05.007.
(Cited on page 19.)

Saha, Bejoy (2003). *Napatau or Tk-Lifetime-Analysis*. unpublished. Institut für Kernphysik, Universität Köln.
(Cited on page 34.)

Shi, Z. and Z. P. Li (2018). "Microscopic description of triaxiality in Ru isotopes with covariant energy density functional theory". In: *Physical Review C* 97.3. DOI: 10.1103/PhysRevC.97.034329.
(Cited on pages 16, 61–64, 67, 91.)

Smith, A. G. et al. (2002). "Lifetimes of yrast rotational states of the fission fragments 100Zr and 104Mo measured using a differential plunger". In: *Journal of Physics G: Nuclear and Particle Physics* 28.8, pages 2307–2316. DOI: 10.1088/0954-3899/28/8/316.
(Cited on pages 40, 41, 61, 69.)

Snyder, J. B. et al. (2013). "High-spin transition quadrupole moments in neutron-rich Mo and Ru nuclei: Testing γ softness?" In: *Physics Letters B* 723.1, pages 61–65. DOI: 10.1016/j.physletb.2013.04.046.
(Cited on pages 17, 62, 63, 67, 91.)

Sugawara, M. (2019). "Attempt at describing triaxiality of ^{108,110,112}Ru by the generalized triaxial rotor model with independent, variable moments of inertia". In: *Physical Review C* 99.5. DOI: 10.1103/PhysRevC.99.054323.
(Cited on pages 16, 64.)

Urban, W. et al. (2004). "New bands and spin-parity assignments in 111Ru". In: *The European Physical Journal A - Hadrons and Nuclei* 22.2, pages 231–239. DOI: 10.1140/epja/i2003-10234-8.
(Cited on page 15.)

Wood, J. L. et al. (2004). "Triaxial rotor model for nuclei with independent inertia and electric quadrupole tensors". In: *Physical Review C* 70.2. DOI: 10.1103/PhysRevC.70.024308.
(Cited on page 14.)

Wu, C. Y. et al. (2006). "Evidence for possible shape transitions in neutron-rich Ru isotopes: Spectroscopy of ^{109,110,111,112}Ru". In: *Physical Review C* 73.3. DOI: 10.1103/PhysRevC.73.034312.
(Cited on page 16.)

Xu, F. R., P. M. Walker, and R. Wyss (2002). "Oblate stability of $A \approx 110$ nuclei near the r-process path". In: *Physical Review C* 65.2. DOI: 10.1103/PhysRevC.65.021303.
(Cited on page 9.)

Zhang, C. L. et al. (2015). "Theoretical study of triaxial shapes of neutron-rich Mo and Ru nuclei". In: *Physical Review C* 92.3. DOI: 10.1103/PhysRevC.92.034307.
(Cited on pages 16, 64, 68.)

Appendix A

Fitted γ-spectra

This appendix contains figures of all the fitted γ-spectra. Unless stated otherwise, the spectra are fitted using two Gaussian peaks on a linear background, following the method described in section 2.1. Particularities of the fits are noted in the figure texts.

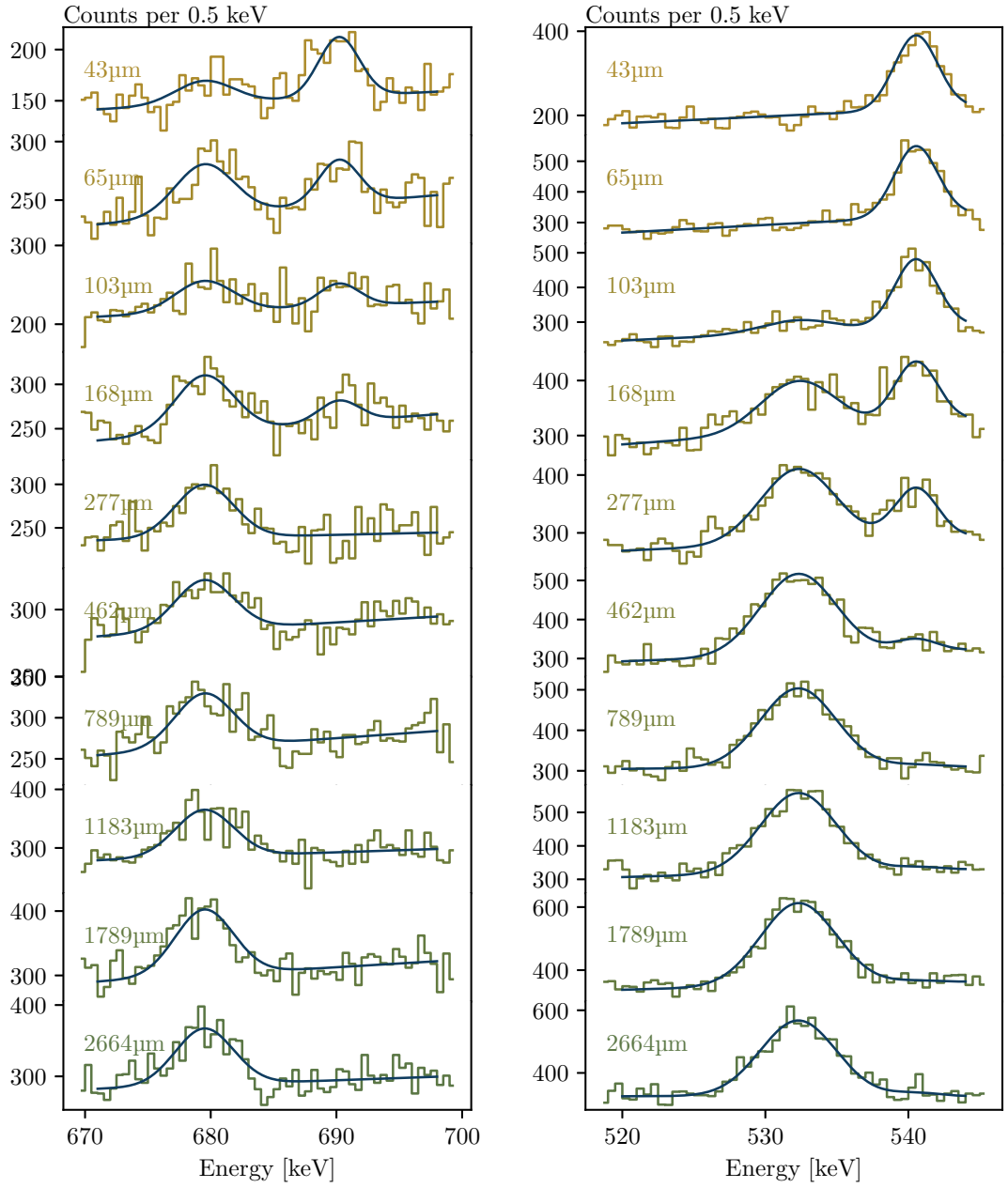

Figure A.1: Transitions $23/2_1^- \rightarrow 19/2_1^-$ @ 691 keV (left) and $19/2_1^- \rightarrow 15/2_1^-$ @ 542 keV (right) in ^{109}Ru.

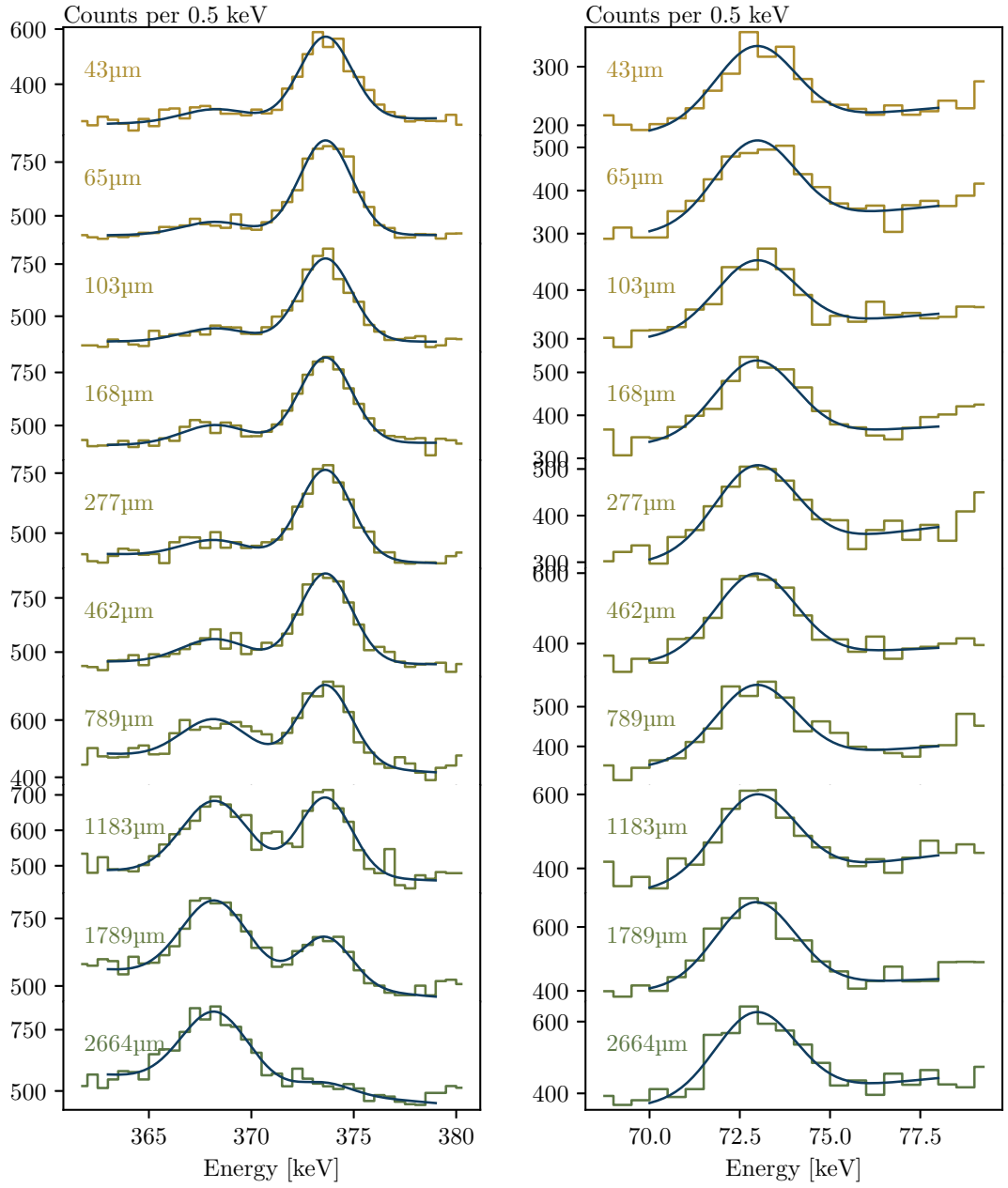

Figure A.2: Transitions $15/2_1^- \rightarrow 11/2_1^-$ @ 375 keV (left) and $11/2_1^- \rightarrow 9/2_1^-$ @ 74 keV (right) in ^{109}Ru. The latter is fitted with a single peak.

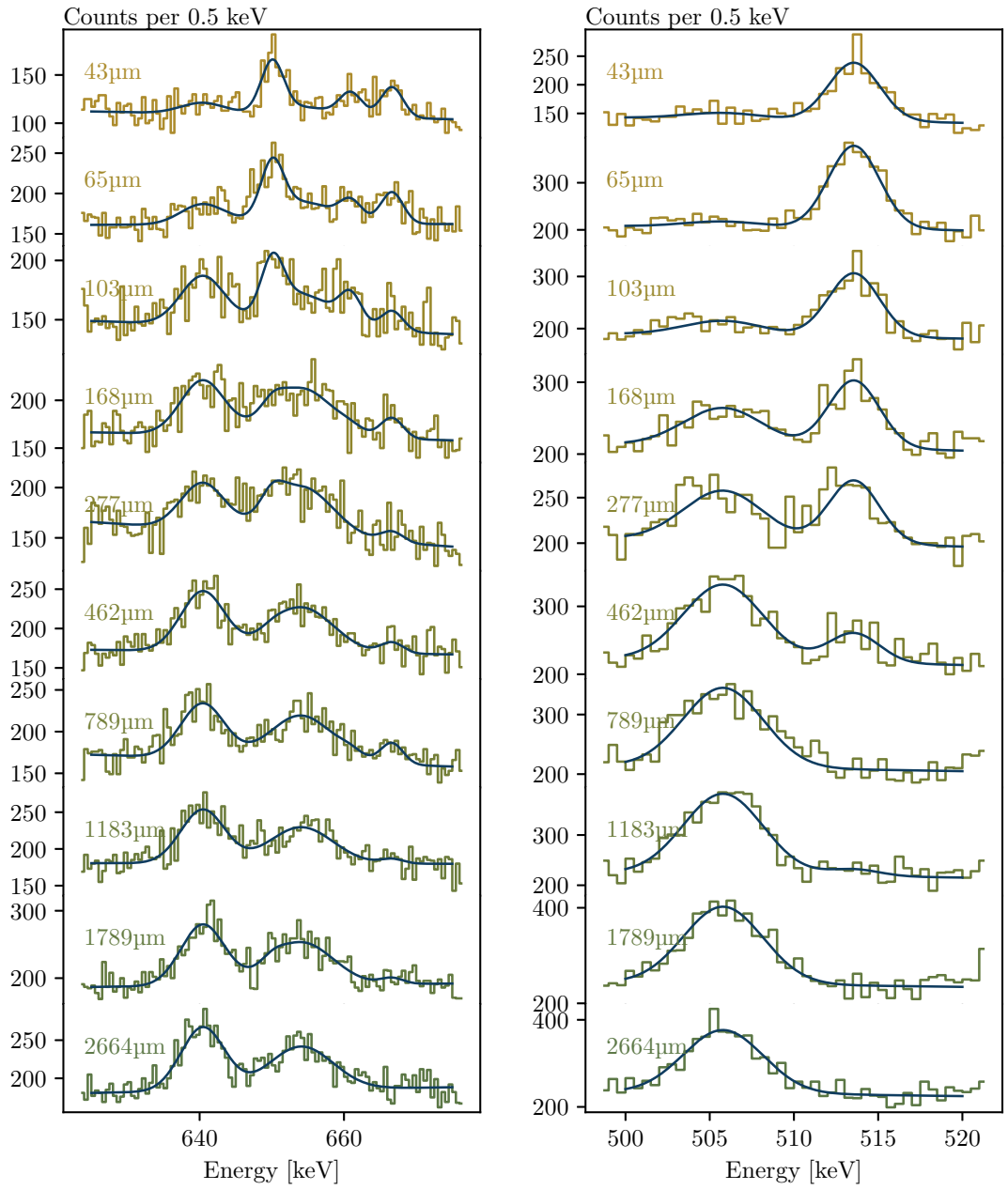

Figure A.3: Transitions $23/2_1^- \rightarrow 19/2_1^-$ @ 651 keV (left) and $19/2_1^- \rightarrow 15/2_1^-$ @ 514 keV (right) in ^{111}Ru. The former includes the transitions $21/2_1^- \rightarrow 17/2_1^-$ @ 661 keV and $19/2_1^+ \rightarrow 15/2_1^+$ @ 666 keV. The before degrader components of these two peaks are fitted as a single peak.

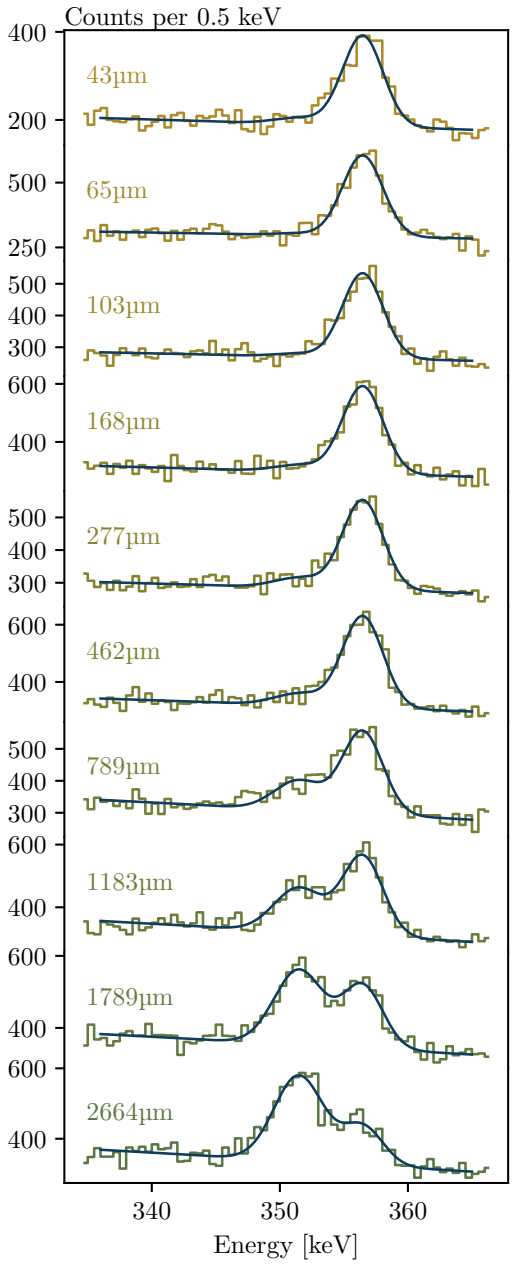

Figure A.4: Transition $15/2_1^- \rightarrow 11/2_1^-$ @ 358 keV in ^{111}Ru.

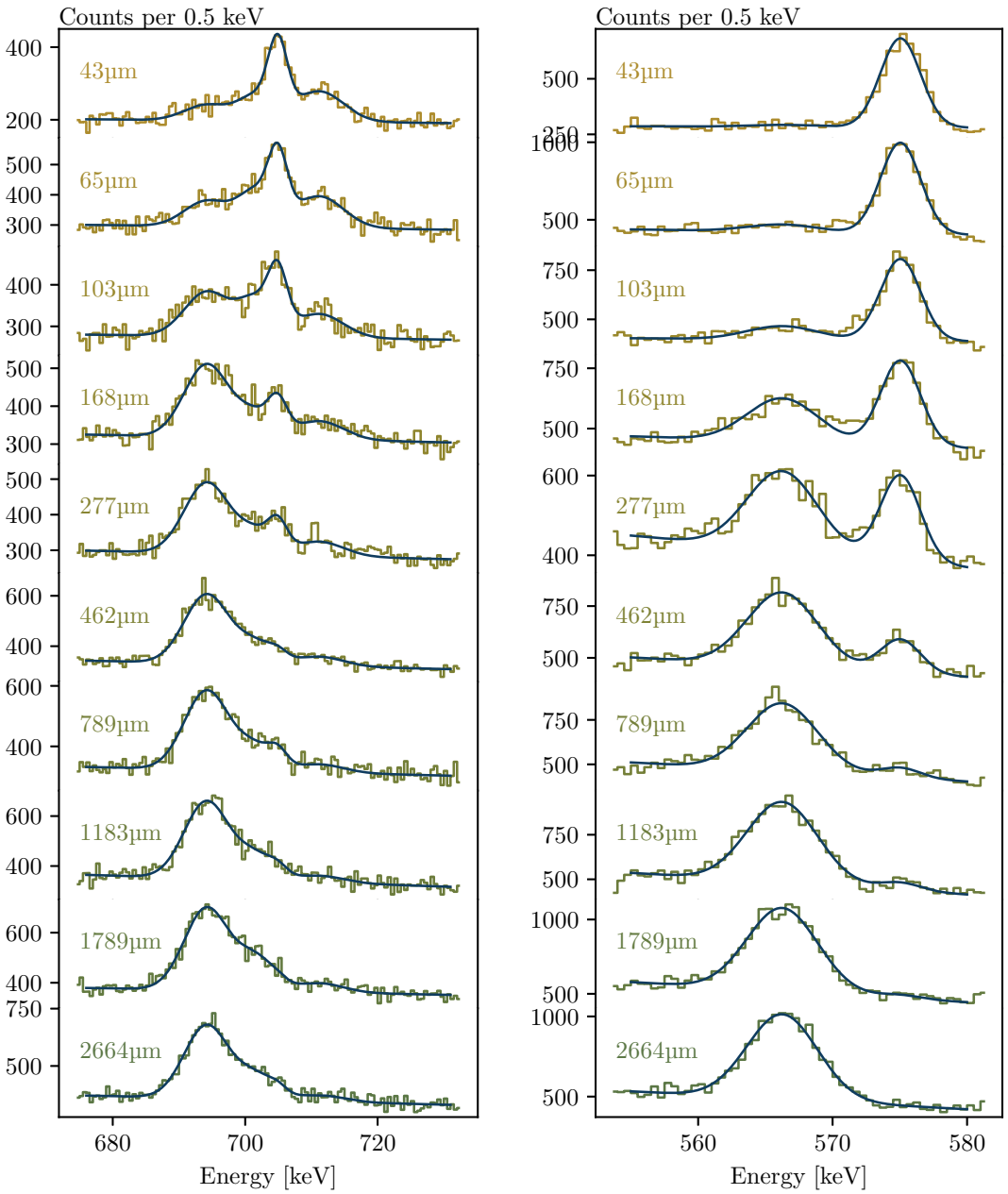

Figure A.5: Transitions $8_1^+ \rightarrow 6_1^+$ @ 705 keV (left) and $6_1^+ \rightarrow 4_1^+$ @ 576 keV (right) in ^{110}Ru. The former also includes $5_1^+ \rightarrow 4_1^+$ and $8_2^+ \rightarrow 6_1^+$ @712 keV, fitted together as a single pair of peaks.

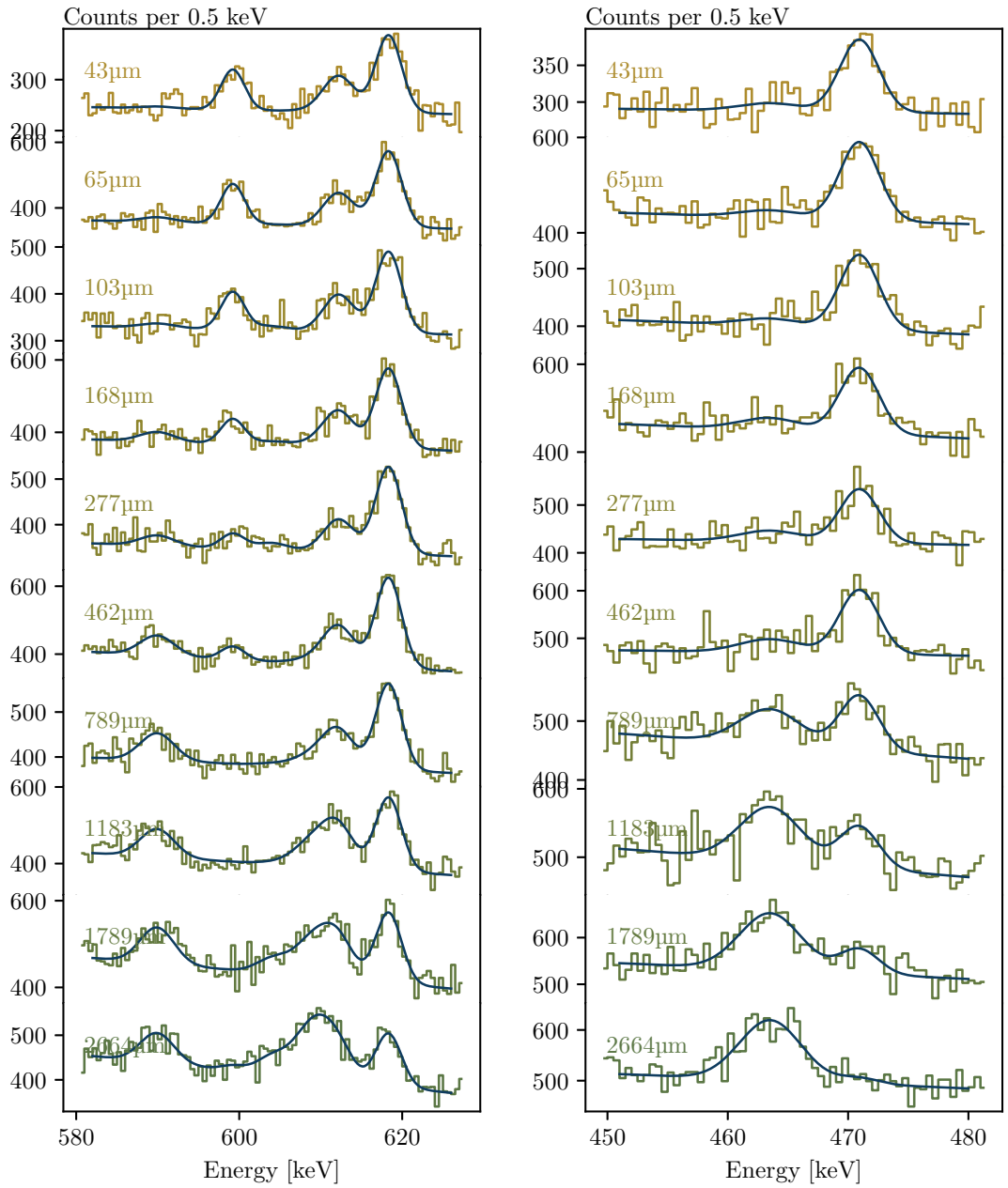

Figure A.6: Transitions $6_2^+ \rightarrow 4_2^+$ @ 600 keV (left) and $4_2^+ \rightarrow 2_2^+$ @ 472 keV (right) in ^{110}Ru. The former also includes fits of $2_2^+ \rightarrow 0^+$ @ 613 keV and $3_1^+ \rightarrow 2_1^+$ @ 619 keV.

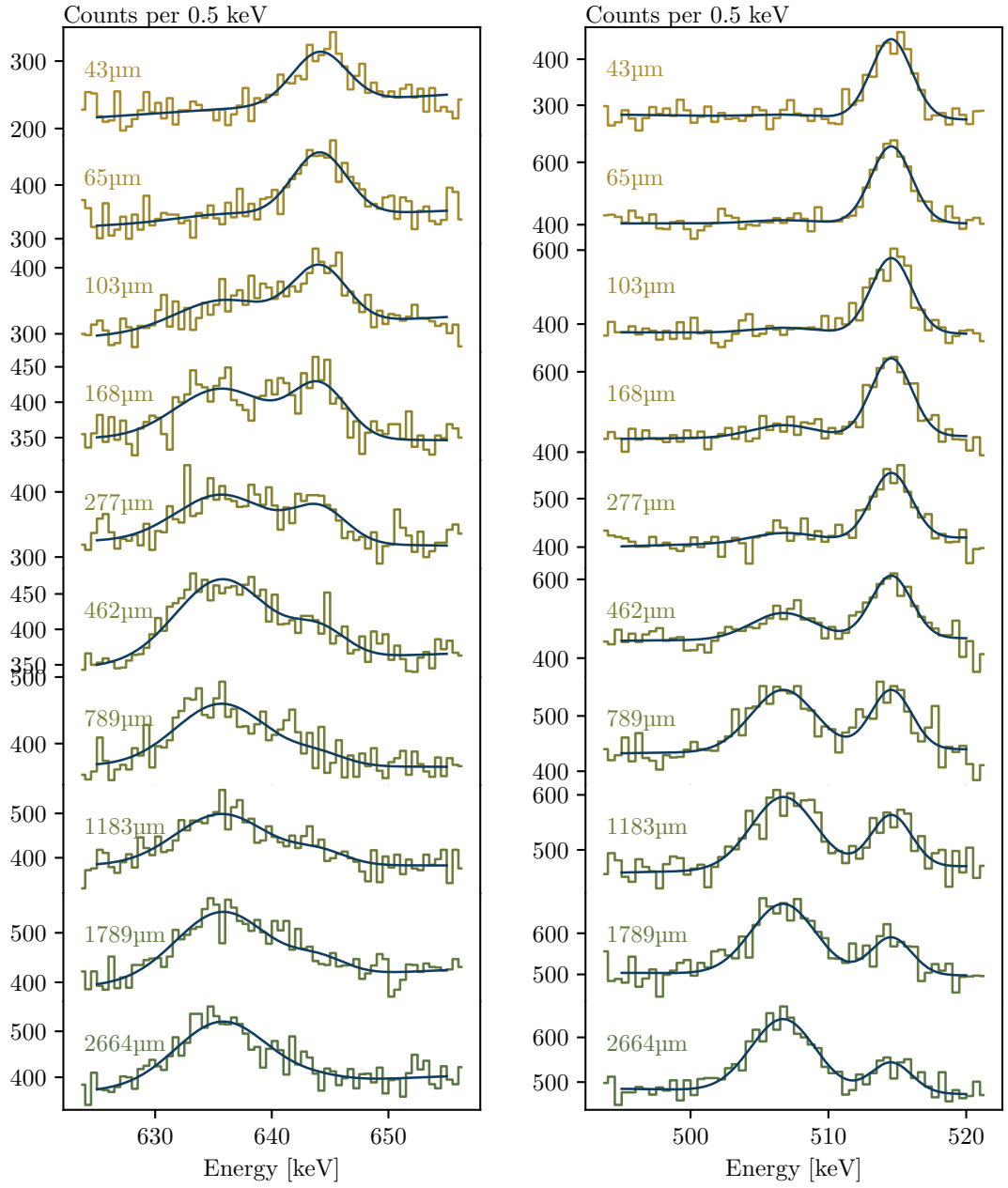

Figure A.7: Transitions $7_1^+ \rightarrow 5_1^+$ @ 646 keV (left) and $5_1^+ \rightarrow 3_1^+$ @ 516 keV (right) in ^{110}Ru.

Appendix B

Fits of simulated decay curves

This appendix contains DCM2 fits of the simulated decay curves used for testing the effects of varying the user-defined parameters. These are the order of the Isplines and number of knots used to fit the decay curves. Their values are given in the figure captions.

The top graph shows the simulated relative decay values $Q_{hi}(x)$ of the feeding energy level, along with the fitted curve. The knots used in the fit are marked as dashed vertical lines. The next graph is equivalent for the simulated decay whose lifetime is measured. The third graph shows the two sides of equation (2.12); the degree of overlap of these curves is an important indication of the quality of the fit. Finally, the bottom graph shows the value $v\tau$ calculated at each experimental value, as well as from the fitted curves. The fitted value is marked by a horizontal dashed line.

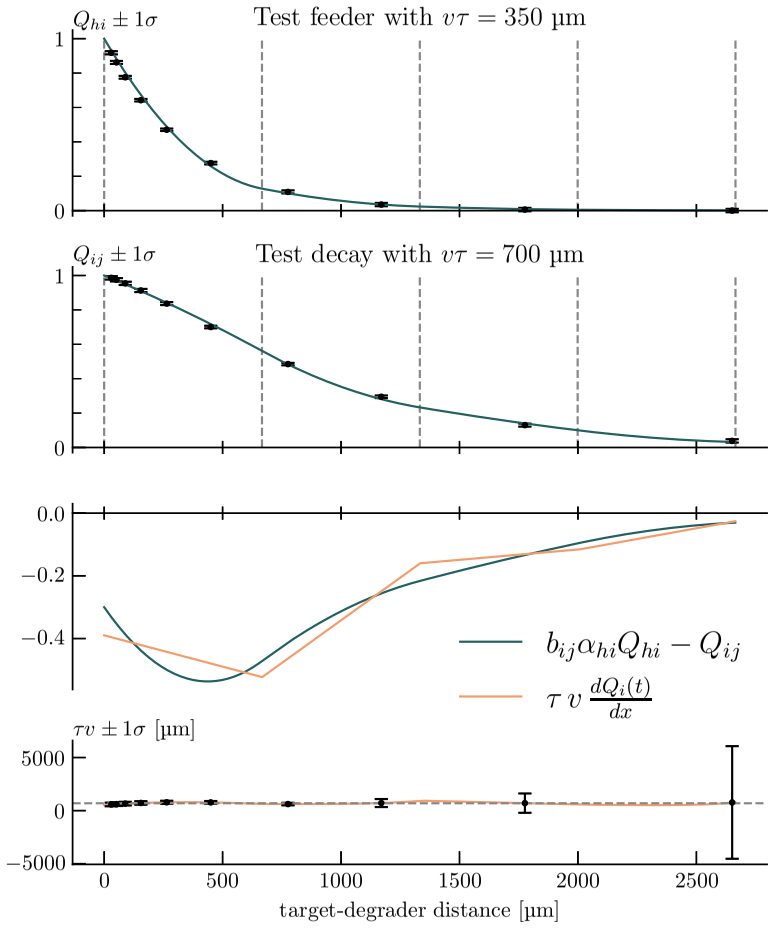

Figure B.1: Simulated decay curves fitted with quadratic splines with five knots. $v\tau = 693 \pm 56$ µm.

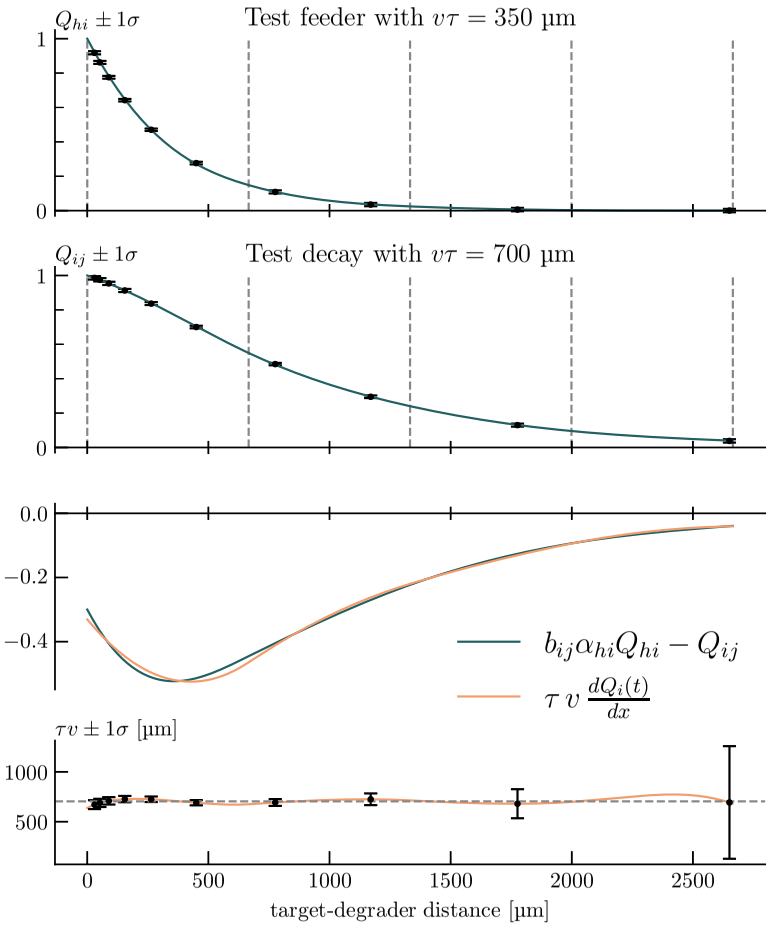

Figure B.2: Simulated decay curves fitted with cubic Isplines with five knots. $v\tau = 704 \pm 12$ µm.

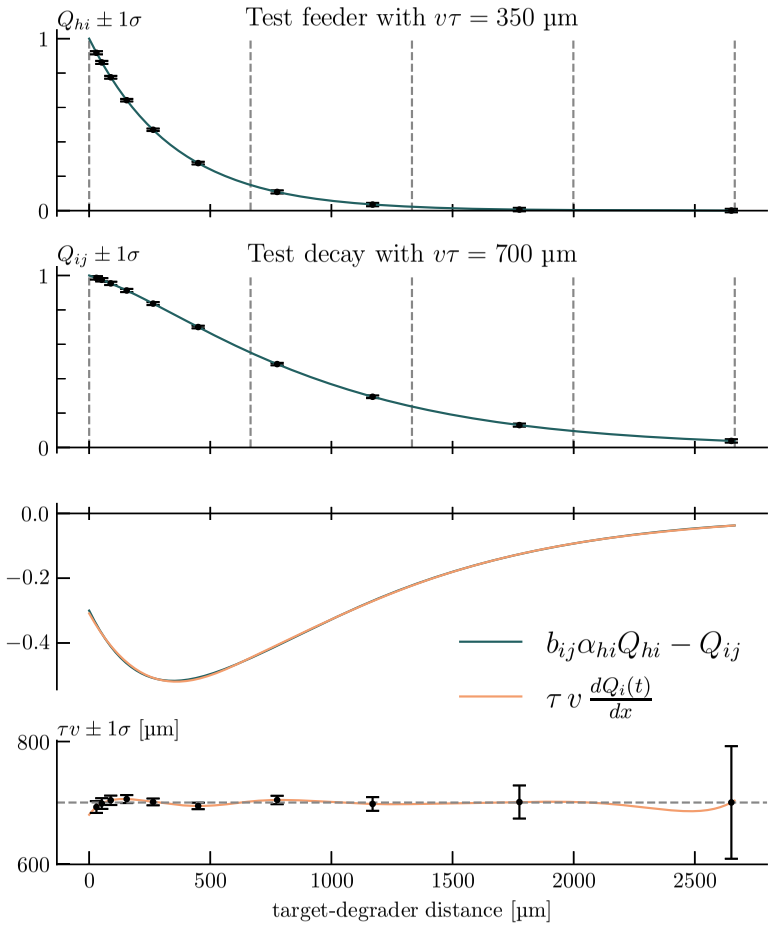

Figure B.3: Simulated decay curve fitted with quartic Isplines with five knots. $v\tau = 700.3 \pm 2.5$ µm.

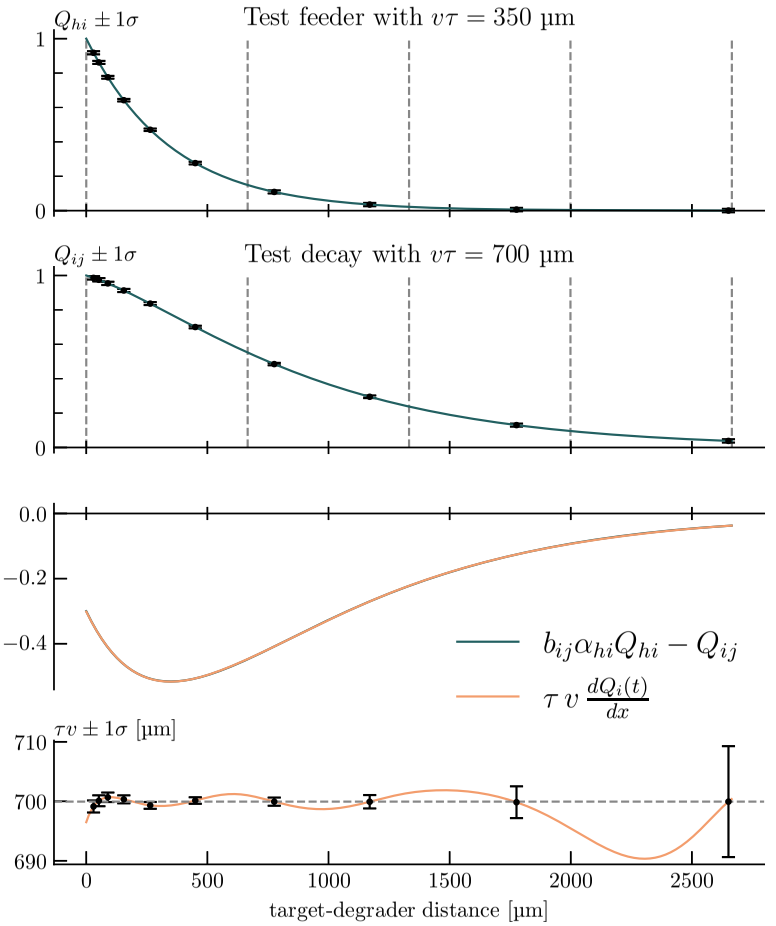

Figure B.4: Simulated decay curve fitted with quintic Isplines with five knots. $v\tau = 699.95 \pm 0.26$ µm.

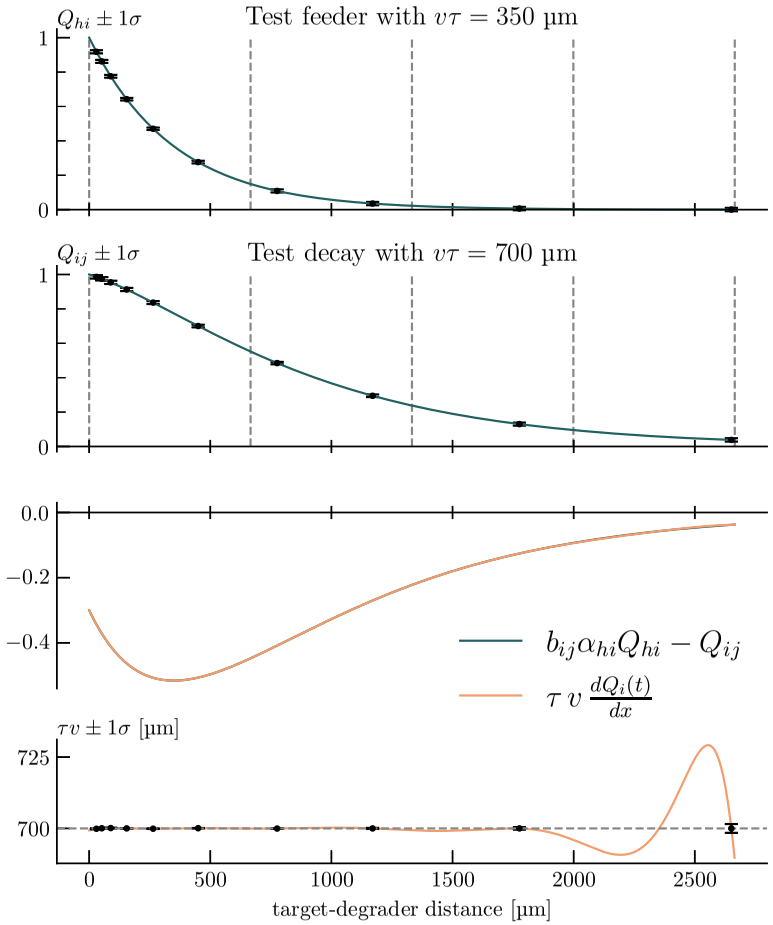

Figure B.5: Simulated decay curve fitted with sixth order Isplines with five knots. $v\tau = 699.997 \pm 0.042$ µm.

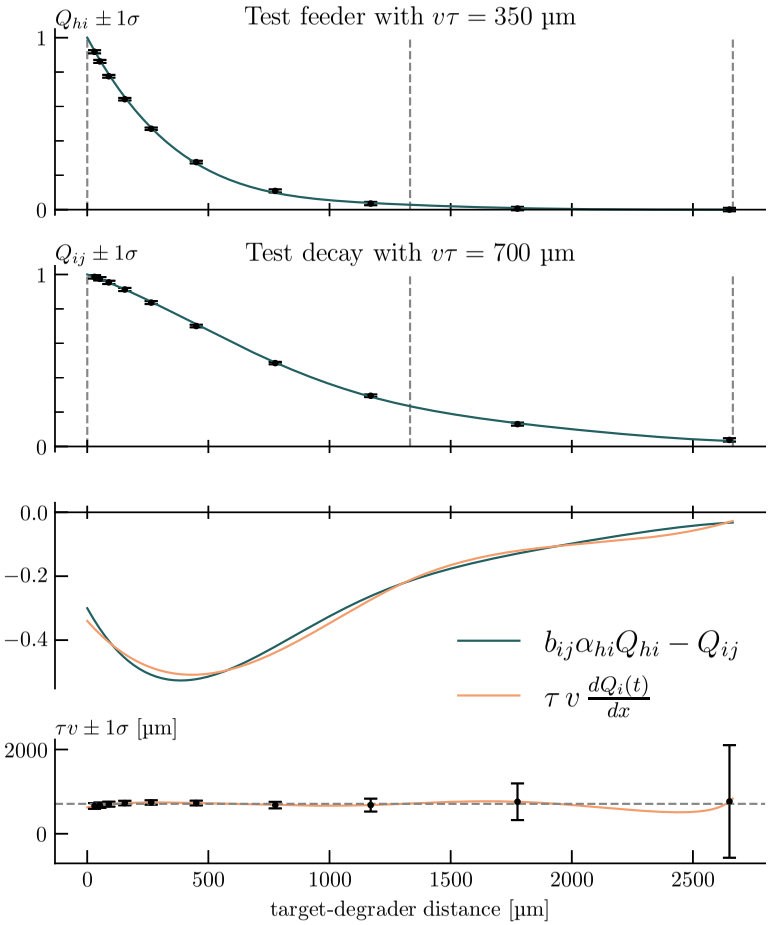

Figure B.6: Simulated decay curve fitted with quartic Isplines with three knots. $v\tau = 709 \pm 23$ µm.

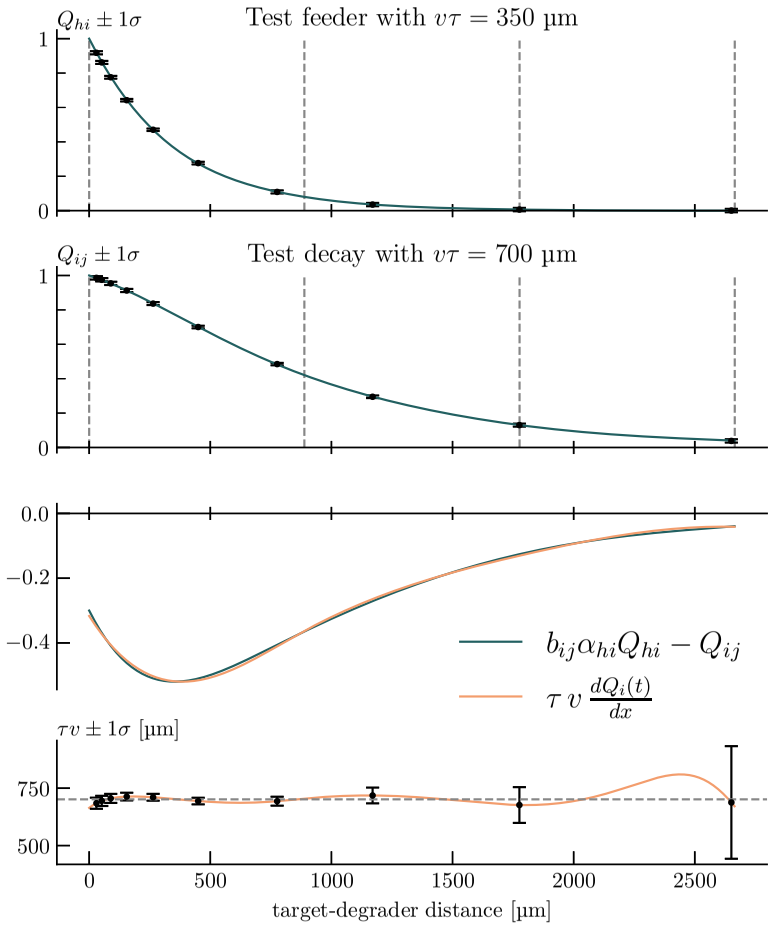

Figure B.7: Simulated decay curves fitted with quartic splines with four knots. $v\tau = 701.3 \pm 6.6$ µm.

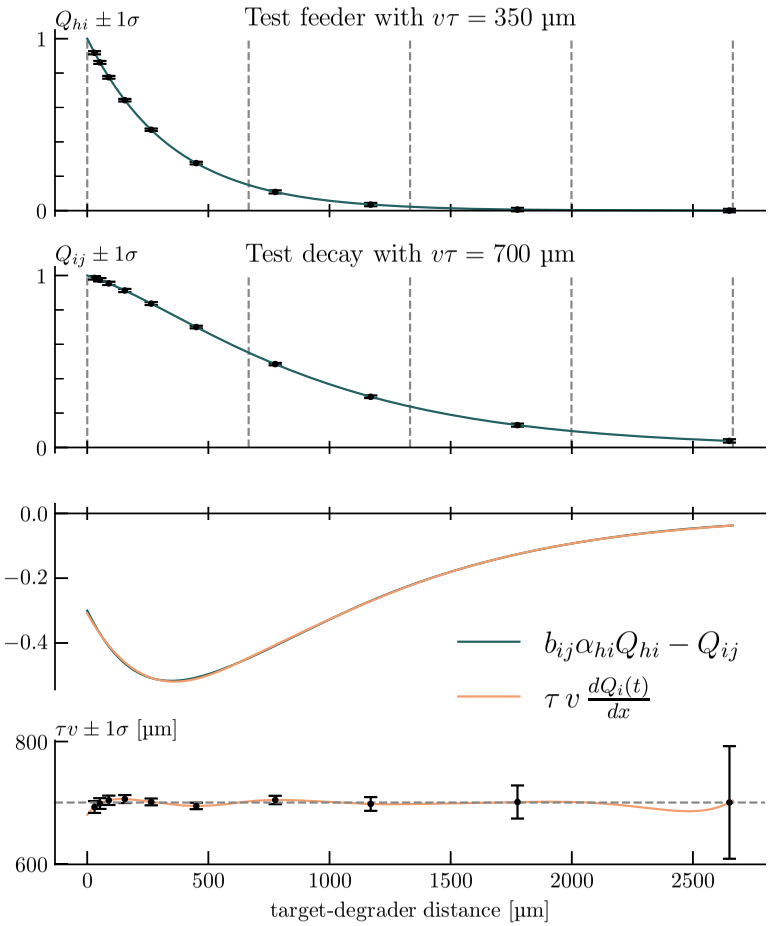

Figure B.8: Simulated decay curves fitted with quartic Isplines with five knots. $v\tau = 700.3 \pm 2.5$ µm.

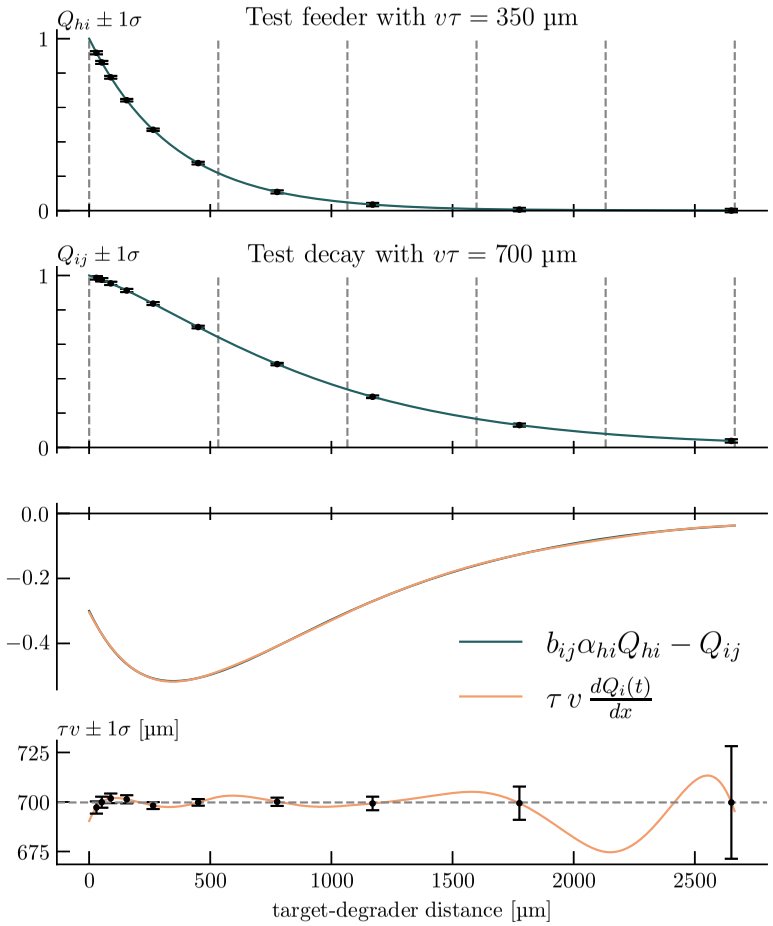

Figure B.9: Simulated decay curves fitted with quartic splines with six knots. $v\tau = 699.76 \pm 0.78$ µm.

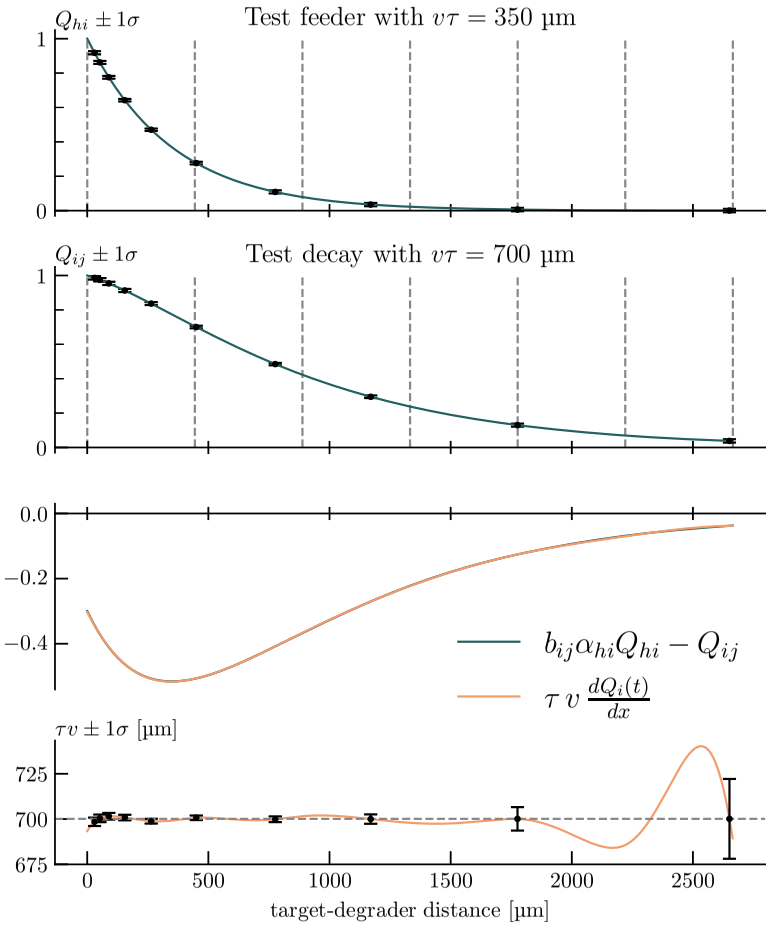

Figure B.10: Simulated decay curves fitted with quartic Isplines with seven knots. $v\tau = 700.11 \pm 0.59$ µm.

Appendix C

Comparison of $B(E2)$ values

Table C.1 gives the numerical values of the points plotted in figure 6.1.

Table C.1: Comparison between the measured and predicted $B(E2)$ values shown in figure 6.1. The uncertainties on the last two digits are shown in brackets for the experimental values.

transition	**experimental** $10^2\ e^2\mathrm{fm}^4$	**GTRM**	**Gogny CHFB***	**RMF + 5DCH†**
Doherty et al. (2017)				
$2_1^+ \to 0_1^+$	20.9 $(^{+16}_{-15})$	19.85	20.85	17.94
$2_2^+ \to 0_1^+$	2.30 (10)	2.07	0.01	1.13
$2_2^+ \to 2_1^+$	35. (13)	25.58	30.06	24.14
$3_1^+ \to 2_1^+$	1.50 (20)	3.70	0.00	1.78
$3_1^+ \to 2_2^+$	31. $(^{+21}_{-22})$	35.45	36.38	30.99
$4_1^+ \to 2_1^+$	29.3 $(^{+31}_{-21})$	28.72	32.43	27.08
$6_1^+ \to 4_1^+$	38. $(^{+9}_{-4})$	35.46	40.66	34.41
This work				
$4_2^+ \to 2_1^+$	0.200 (15)	0.199	0.00	
$4_2^+ \to 2_2^+$	5.91 (45)	5.62	16.25	15.90
$4_2^+ \to 3_1^+$	6.76 (52)	6.61	6.45	
$4_2^+ \to 4_1^+$	5.27 (40)	5.76	13.86	11.87
$5_1^+ \to 3_1^+$	12.9 (24)	14.56	24.20	21.23
$5_1^+ \to 4_1^+$	0.52 (10)	0.21	0.01	
$5_1^+ \to 4_2^+$	8.1 (15)	24.96	19.37	
$6_1^+ \to 4_1^+$	36.3 (37)	35.46	40.66	34.41
Snyder et al. (2013)				
$6_2^+ \to 4_2^+$	18.0 (43)	10.42	27.60	23.82
$7_1^+ \to 5_1^+$	22.4 (37)	20.11		30.77
$8_1^+ \to 6_1^+$	21.6 (25)	38.44		40.01
$8_2^+ \to 6_2^+$	20.3 (40)	0.73		32.18
$9_1^+ \to 7_1^+$	27. (12)	90.89		37.66

*Delaroche (2010)

†Shi and Li (2018)